Master thesis

Synthesis of Silicon Carbide Thin Films by Pyrolysis of a Polycarbosilane Precursor

carried out for the purpose of obtaining the 2nd degree of Dipl.-Ing. or DI, submitted at TU Wien, Faculty of Sensor- und Aktuatorsysteme, by

DI Günter Wedl, Bsc

Mat.Nr.: 09926574

under the supervision of

Univ.Prof. Dipl.-Phys. Dr.rer.nat. Schmid Ulrich

and

Dr. Markus Leitgeb

Institut für Sensor- und Aktuatorsysteme, E366-02

Wien, 18.06.2024

Affidavit

I declare in lieu of oath, that I wrote this thesis and performed the associated research myself, using only literature cited in this volume. If text passages from sources are used literally, they are marked as such.

I confirm that this work is original and has not been submitted elsewhere for any examination, nor is it currently under consideration for a thesis elsewhere.

I acknowledge that the submitted work will be checked electronically-technically using suitable and state-of-the-art means (plagiarism detection software). On the one hand, this ensures that the submitted work was prepared according to the high-quality standards within the applicable rules to ensure good scientific practice "Code of Conduct" at the TU Wien. On the other hand, a comparison with other student theses avoids violations of my personal copyright.

City and Date	*Signature*

Acknowledgements

I would like to thank my thesis adviser Ulrich Schmid and Markus Leitgeb for their guidance, help and constant support during the whole research work.

Appreciation is also extended to the members of the Institute of Faculty of Sensor- and Actuator Systems, who gave me the support all the time.

I also want to say thank you Krisztina Wedl and Sophie Wedl, who always remind me what is important in life and thank all my friends and study colleagues for the great time.

"If you want to find the secrets of the universe, think in terms of energy, frequency, and vibration." – Nikola Tesla

Table of Contents

Abstract

In this work a silicon carbide (SiC) thin film on silicon (Si) bulk material, using SMP10, a liquid precursor to SiC ceramics was developed. A monocrystalline SiC foil was developed at ISAS (Technische Universität Wien) which could help to reduce cutting and polishing losses when originating from monocrystalline SiC wafers and when subsequently bonded on a Si or polycrystalline SiC wafer. For this purpose, the SiC thin film should be used as sticky layer for bonding these monocrystalline silicon carbide (SiC) foils on Si in a first attempt. The SMP10 should coat the Si surface evenly and, after pyrolysis, form a dense, coherent SiC thin film. To achieve this thin film, spin coating and dip coating were investigated. With spin coating a dense and coherent thin film, still with few defects but with controllable thickness from 50 nm to 500 nm was generated. The spin coating process was successfully used to create thin films with and without nitrogen as dopant, which can be used for electrically conductive bonding for future works. The high cost reduction would be achieved if foils are bonded to polycrystalline SiC substrates. Bonding to a Si substrate would be a predominantly of a technological advancement, rather than targeting specific applications.

Kurzfassung

In dieser Arbeit wurde ein Siliziumkarbid (SiC) Dünnfilm auf Silizium Wafern, mittels SMP10, einem flüssigen, keramischen Polymer aufgebracht. Am ISAS der Technische Universität Wien wurde eine monokristalline SiC Folie entwickelt, welche helfen soll, die auftretenden Säge- und Polierverluste bei der Herstellung von Leistungsbauelementen auf monokristallinen SiC Wafern zu minimieren, indem die Folie auf polykristalline SiC Wafer gebondet wird. Zu Beginn dieser Untersuchungen dienen Si Wafer aus Kostengründen für Versuchszwecke. Für diesen Bond-Vorgang soll der Dünnfilm als eine Art Klebeschicht dienen. Um diesem Zweck zu genügen, muss der SiC Dünnfilm eine dichte und zusammenhängende Schicht bilden. Für die Herstellung des Dünnfilms wurde das Spin Coating Verfahren und das Tauchzieh Verfahren untersucht. Mit dem Spin Coating Prozess konnten dichte, zusammenhängende Schichten mit wenigen Defekten und einer kontrollierbaren Schichtdicke von 50 nm bis 500 nm hergestellt werden. Das Spin Coating Verfahren wurde erfolgreich verwendet, um SiC Dünnfilme mit und ohne Stickstoff als Dotierelement zu erzeugen, welche als Grundlage für weitere Arbeiten dienen. Bonden der Folie auf polykristallinen SiC Wafer würde die Kosten bei der Herstellung von SiC leistungselektronischen Bauelementen reduzieren, wobei zudem das erstmalige Bonden der Folie auf Si Substrat demonstriert werden konnte.

List of Abbreviations and Symbols

SMP10	Polycarbonsilane from Starfire Systems
AIBN	Azobisisobutyronitrile
TEVS	Triethoxyvinylsilane
SEM	Scanning electron microscope
XRD	X-ray diffractometer
FTIR	Fourier transform infrared
Si	Silicon
n-Si	Negative doped silicon
p-Si	Positive doped silicon
SiC	Silicon carbide
SiO	Silicon monoxide
SiN	Silicon nitride
N	Nitrogen
rpm	Rotation per minute
sccm	Standard cubic centimeter
CVD	Chemical vapor deposition
LPCVD	Low pressure chemical vapor deposition
RCA	Radio Corporation of America
SC1/2	Standard cleaning 1/2
UV	Ultraviolet
UV-C	Ultraviolet-C
US	Ultrasound
IR	Infrared
DoE	Design of experiment
ρ	Specific resistance
R	Ohmic resistance

1. Introduction

The unique combination of properties of silicon carbide (SiC), which cannot be found at other more common semiconductor materials such as its high thermal conductivity and melting point, extreme hardness and excellent resistance to chemical attack and mechanical damage makes it a very interesting material for electrical engineering. Furthermore, it is characterized by a range of large energy bandgaps of 2.29 eV - 3.3 eV depending on the polytope, and a high saturated drift velocity of $2 \cdot 10^7$ cm/s - $2.7 \cdot 10^7$ cm/s [1], [2], [3], which are particularly important for electronic applications. Therefore, SiC is most promising as electronic and as structural material for advanced microelectronic and microelectromechanical systems (MEMS) since 30 years [3].

For SiC wafer production, SiC boules grown using the modified Lely method are most commonly used [4]. The boules are grinded to the desired diameter and then sliced into wafers. The slicing induces saw marks, surface damage, and subsurface damage which are treated through surface grinding and lapping processes with the goal to parallelize each face of the substrate and achieve global flatness and reduce the damages of the slicing process [4], [5]. To meet the target surface roughness and wafer quality, chemical mechanical polishing is used to obtain an atomically smooth surface [4]. This complex manufacturing process requires different machines and tools, making it not only costly but also time consuming.

Monocrystalline SiC foils have been developed, using metal assisted etching and photoelectrochemical etching [6], [7]. To reduce the losses of slicing and polishing, these foils can be bonded to a cheaper bulk material such as polycrystalline SiC or silicon (Si).

The aim of this work is to develop an adhesive (sticky layer) for bonding monocrystalline SiC foils on Si bulk material using SMP10, a polycarbonsilane in form of a one-component liquid precursor to SiC ceramics from the company Starfire systems. The to be developed thin film layer should therefore be a dense layer with as few defects as possible, controllable thickness and if possible, electrically conductive (through nitrogen (N) doping).

2. State of the Art

To deposit a thin film on a foreign substrate, different methods have been described in literature, such as molecular beam epitaxial growth [8], magneton and RF sputtering [9], [10], chemical vapor deposition (CVD) [8], or bonding two different substrates together [11]. Since the aim of this work is to fabricate a SiC thin film with a SiC pre-ceramic polymer on a Si substrate, the above-mentioned methods will be only discussed for SiC on Si.

One method to achieve a SiC thin film on Si is the low-pressure chemical vapour deposition (LPCVD) process, where gaseous precursors undergo a chemical reaction on the selectively heated silicon substrate to grow the SiC layer. A schematic of a LPCVD reactor is shown in Figure 1.

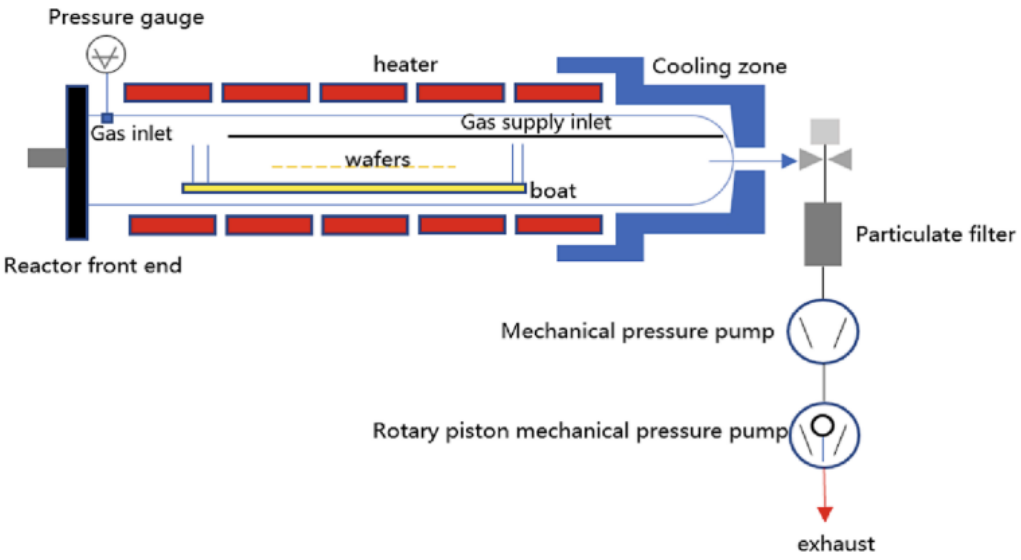

Figure 1: Simplified structure of a LPCVD reactor [12].

Figure 1 shows a simplified structural schematic of a tube LPCVD reactor. The wafers are vertically lined up in the entire reactor and small gas inlet holes in a ring shape are scattered on the side of the reactor. Two gas filler pipes run from the end into the front of the equipment, and spray ports are arranged in a uniform linear pattern on the supply gas pipes [12]. The gas reacts on the wafer, forming a thin film. This can be done in one step, using *e.g.* hexamethyldisilane ($Si_{12}C_6H_{18}$) and a carrier gas to deposit monocrystalline SiC [8], or through alternating supply deposition for polycrystalline SiC [3], where monosilane (SiH_4) and propane (C_3H_8) are used as process gasses in an alternating mode after each other. The process is shown in Figure 2.

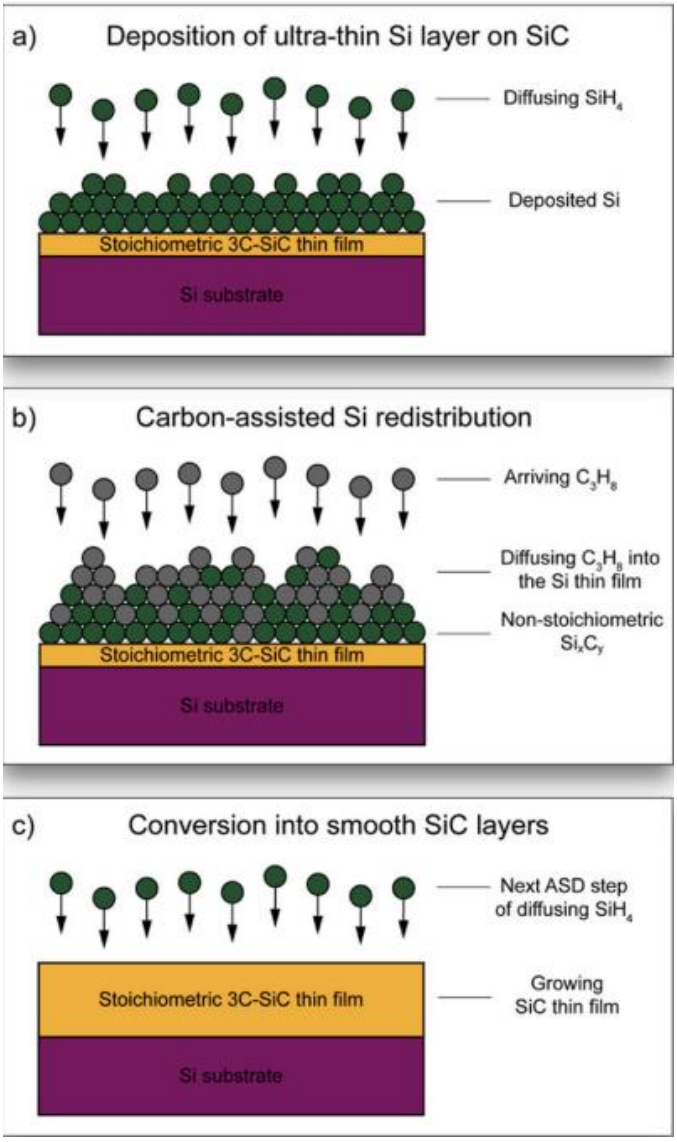

Figure 2: Schematic of the altering supply deposition [3].

In Figure 2 a SiC thin film is grown on a Si substrate by deposition of Si in a first step (a), followed by carbon diffusion in Si (b) and lastly redistribution of the Si and C atoms (c).

Another method to gain SiC layers on Si is wafer bonding as described by M. R. Jennings [13]. Figure 3 shows one possible process of wafer bonding, with the advantage, that also hexagonal, single-crystalline thin films can be attached to a cubic silicon substrate.

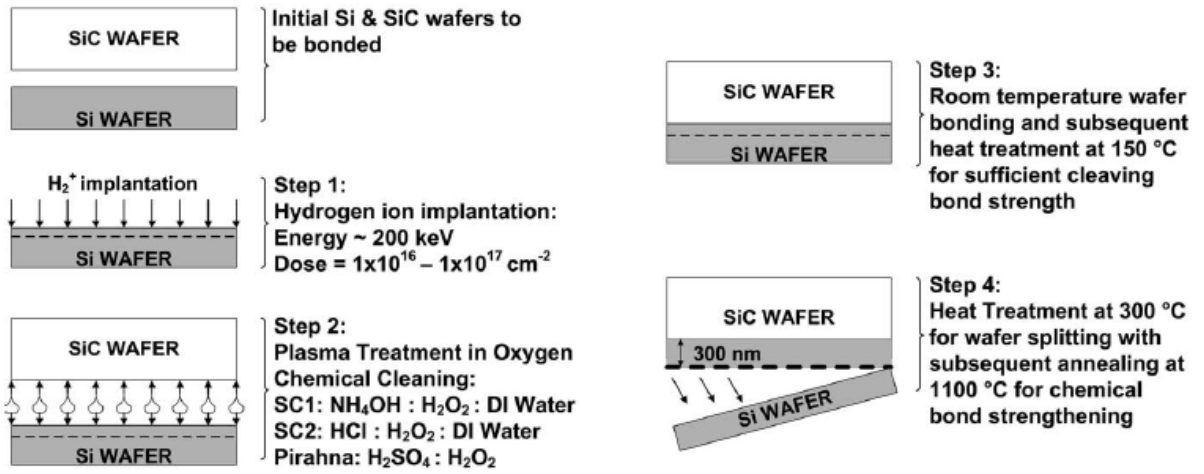

Figure 3: Process of wafer bonding [13].

In Figure 3, the wafers were bonded at room temperature, which is possible due to the surface activation. Before the bonding, hydrogen ions (H^+) were implanted into the Si wafer. Thereafter, the wafers were cleaned using oxygen (O_2) plasma, standard cleaning (SC) 1 and 2 processes as well as piranha acid treatment for 20 minutes. The wafers were then bonded in vacuum at room temperature, where the two activated surfaces of the SiC and Si wafer are pressed together [14], followed by a heat treatment to achieve sufficient bond strength for cleaving [13]. In the last step, the Si layer was cleaved, followed by annealing at 1100 °C to strengthen the bond between Si and SiC further.

Figure 4 (a) and (b) show the principles of magneton and RF sputtering to fabricate SiC thin films on Si, respectively.

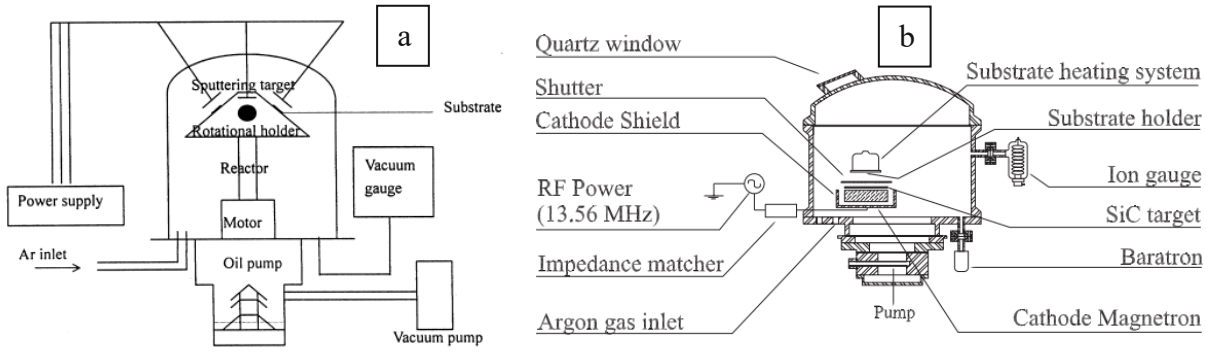

Figure 4: Principle of magneton sputtering [9] *(a) and RF sputtering* [10] *(b) of SiC.*

Sputtering is the deposition of a target material on a substrate using plasma for particle generation which bombard the target for material removal. Therefore, sintered SiC targets with high purity are used [10], [15]. In the sputtering process, ions and energetic neutrals are crossing the target dark space (space between plasma and target), which leads to emission of the target

material because positively charged ions hit the target and their momentum is transferred. The sputtered target material is transported from the target to the substrate, were it deposits in a re-emission of material from the substrate [16]. Figure 4 (a) and (b) show this process. In Figure 4 (a) the substrate where the SiC should be deposited is fixed on a rotating sample holder. The SiC targets are above the rotating holder in a fixed position. As soon as the power supply is switched on and the samples are beneath the targets, SiC will be deposited on the substrate. In Figure 4 (b) the SiC target is beneath the substrate and a shutter can block the way of the plasma beam. If the power supply is switched on and the shutter is open, SiC will be deposited on the substrate.

Molecular beam epitaxy (MBE) is a process for growing thin, epitaxial films. Figure 5 shows a schematic an MBE growth vacuum chamber [17].

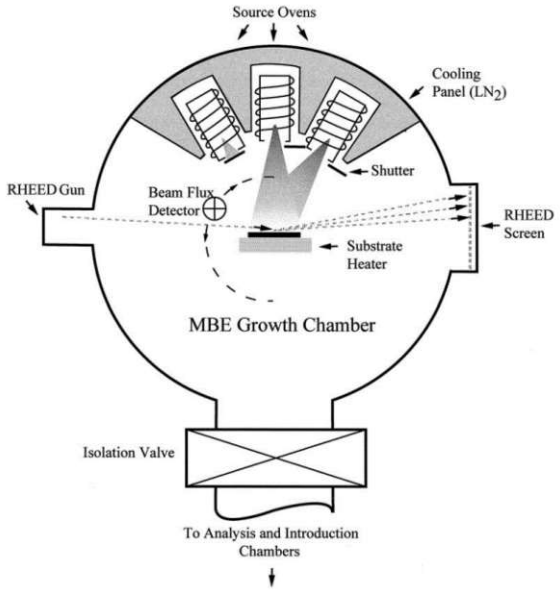

Figure 5: Schematic of an MBE growth chamber [17].

In Figure 5, the substrate is mounted on a heater block facing the source ovens, which are used to evaporate the target material. Mechanical shutters can switch the beams from the source oven on and off, which transport the target material to the substrate [17].

3. Methods and Experiments

The goal is to develop a process that allows the synthesis of dense crystalline SiC thin films on Si substrates with different thicknesses. If the SiC thin film can be fabricated successfully, the film should also be doped. In this chapter, the used methods and the conducted experiments will be explained, starting with the polymerization reactions, and ending with the analysis of the produced sample. Figure 6 shows the general process of synthesizing the SiC thin film.

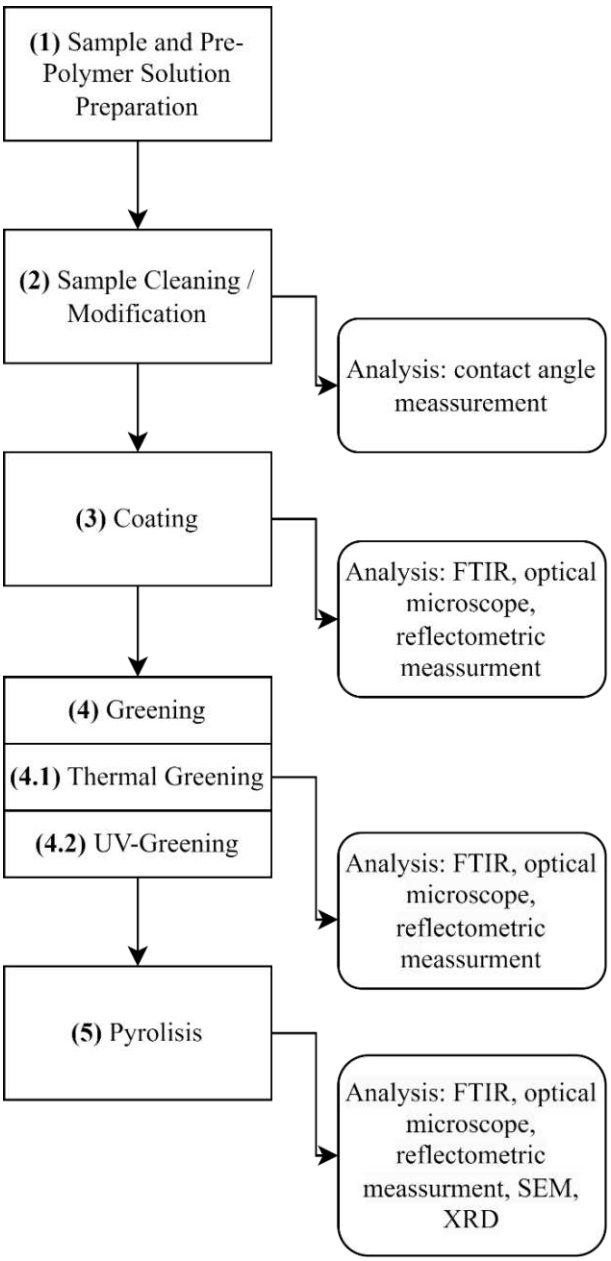

Figure 6: Process overview of the SiC thin film synthesis.

The first step in Figure 6 of the synthesis process is the sample preparation (1), followed by sample cleaning (2), coating (3), greening (4) and finally pyrolysis (5). The greening can be

divided into thermal greening (4.1) in the furnace and UV-greening (4.2) which is only possible if a radical starter is admixed to coating solution. From step 2 to 5 the effectiveness of each used technique was observed with different measurement and analysis methods. The methods which were mostly used are shown in Figure 6.

3.1. Sample Preparation

Sample Preparation generally consists of cutting a Si wafer into 1 cm x 1 cm squares and cleaning them, using different methods such as Radio Corporation of America (RCA) clean, ultrasonic or ozone, followed by a surface chemistry modification. Also, the preparation of the pre-polymer liquid in different dilutions and doping agents is considered as sample preparation.

3.1.1. Polymerization reaction of polycarbonsilan (SMP10) pre-polymer solution

Starfire Sytems StarPCSTM SMP-10 (SMP10) is a one-component liquid precursor to SiC ceramics with high purity ceramic yields of near stoichiometric SiC of 72 % to 78 % [18]. Figure 7 (a) shows the structure of SPM10 with its vinyl group (1) and Figure 7 (b) a bottle with liquid SMP10 solution, which is a yellow, translucent viscous liquid.

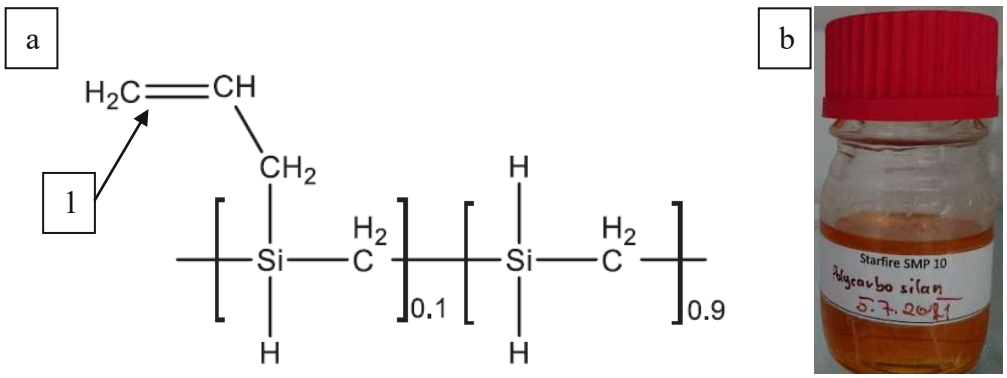

Figure 7: Structure of SMP10 [19] *(a) and SMP10 (b).*

The green cure (hydrosilylation), where the liquid solution forms a hard film, can be done from 180 °C to 400ºC, depending on the degree of desired hardness, while amorphous SiC is formed between 850°C and 1200ºC, while nano-crystalline β-SiC is formed between 1250 °C and 1700 ºC [18]. The mechanism of the polymerisation is shown in Figure 7 [19].

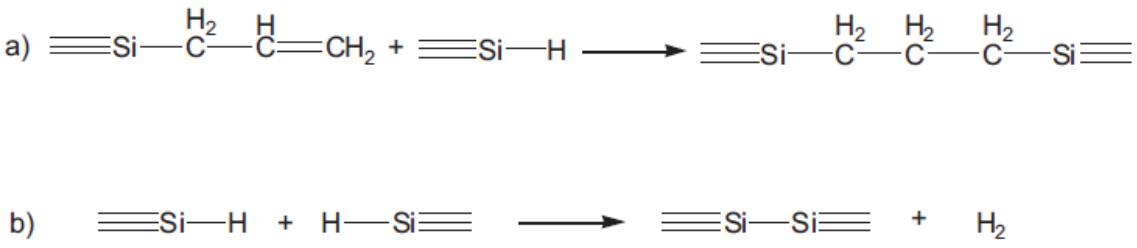

Figure 8: Hydrosilylation (a) and dehydrocoupling (b) reactions occurring up on thermal cross-linking of SMP10 [19].

In Figure 8 the two, from the structure of SMP10 indicated main mechanisms which contribute to its thermal cross-linking process, hydrosilylation and dehydrocoupling reactions are shown. The first reaction, Figure 8 (a), of hydrosilylation, takes place in the range of 180 °C to 400 °C [18] and causes curing or crosslinking of the liquid preceramic polymer. The second reaction, Figure 8 (b), the dehydrocoupling, takes place in the ceramization process [19], the pyrolysis, from 850 °C to 1700 °C [18].

3.1.2. Doping of SMP10

For doping the SiC film with nitrogen, the nitrogen can be admixed into SMP10 using the carriers liquid methylvinylhydrogen polycarbosilazane (Durazane) or azobisisobutyronitrile (AIBN), respectively. While Durazane was a ready-to-use liquid which was not mixing well with SMP10 and led to dewetting, AIBN was a powder which first had to be dissolved. For AIBN, m-xylene was used as solvent, which also could be used for diluting SMP10. The cross-linking mechanism of AIBN is shown in Figure 9.

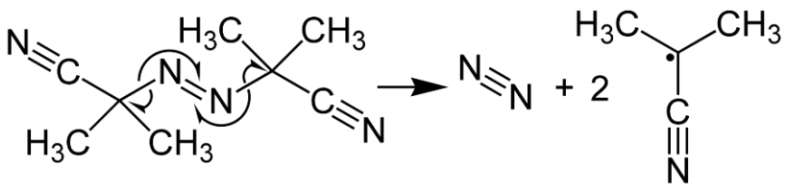

Figure 9: Photodissociation of AIBN. Nitrogen containing radical becomes part of Si-C-H polymer [20].

The nitrogen finally incorporated into the polycrystalline SiC serves as dopant. AIBN not only serves as nitrogen source, but also as radical starter for the first polymerization reaction of SMP10, when exposed to UV-C light or moderate heat [21].

3.2. Sample Cleaning

To remove impurities like residues from wafer sawing or organic or inorganic pollution through e.g. dust or wrong handling, the silicon wafer samples had to be cleaned. Therefore, cleaning with O_2-plasma, with piranha acid or the RCA process, with and without ultra sonic (US) pre-cleaning were performed. Before cleaning, the protective foil of the wafer was removed in an iso-propanol bath in a petri dish.

US-bath: For precleaning, the samples, a US-bath from Bandelin Sonorex as used. The silicon samples were immersed in a small beaker with iso-propanol, which was placed in a, to 45 °C heated US-bath for 10 minutes with an effective ultrasonic power of 160W.

O_2-plasma: The cleaning with O_2-plasma was done in the reactive ion etcher STS 320 with a plasma generator power of 100 W for 2 min and an oxygen flow of 40 sccm.

Piranha acid: The piranha acid was freshly mixed for each cleaning procedure, using 30 ml of concentrated sulfuric acid and 10 ml of hydrogen peroxide (30 %), according to equation (1) [22].

$$H_2SO_4 + H_2O_2 \rightarrow H_2SO_5 + H_2O \qquad (1)$$

Piranha acid cleans organic and metallic residues from the surface [22]. Therefore, the sample was immersed for 20 minutes in piranha acid at 80 °C. After the cleaning process, the samples were rinsed with deionised (DI) water and dried with nitrogen.

RCA cleaning: The RCA clean consists of two processes, standard cleaning SC 1 and SC 2, respectively [23]. The SC 1 process is effective against organic impurities, while the SC 2 process is effective against metallic pollutions. For SC 1, ammonium hydroxide (29 %), hydrogen peroxide (30 %) and DI water were mixed in a volume ratio of 1:1:5 [24], while for SC 2 hydrochloric acid (37 %), hydrogen peroxide (30 %) and DI water were mixed in a volume ratio of 1:1:6 [24]. For both processes, the samples were immersed in the respective solution for 15 minutes at 80 °C. After each bath, the samples were rinsed with DI water and tried with nitrogen.

3.3. Surface Modification

For a better adherence of SMP10 on the substrate, surface vinyl bonds for better adhesion were created, which also leads to a hydrophobic surface of the silicon. Therefore,

triethoxyvinylsilane (TEVS) was used, which lowers the surface energy. The structure and bondage of TEVS on silicon is shown in Figure 10.

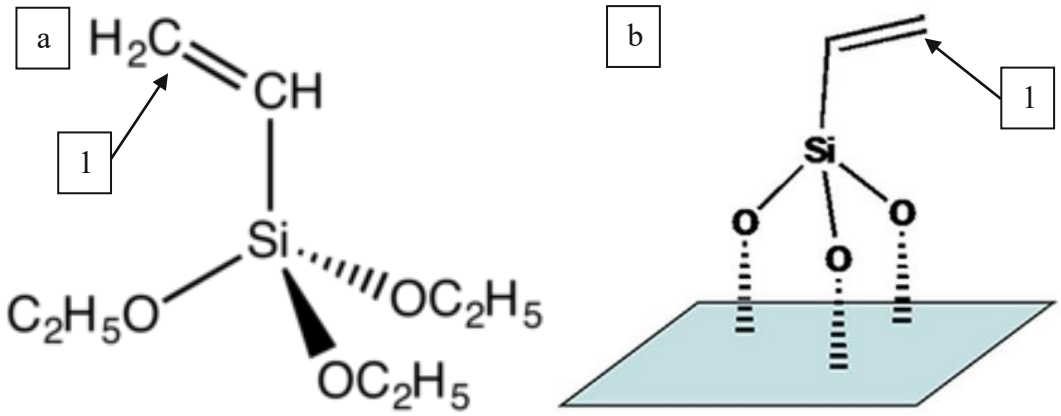

Figure 10: structure of TEVS [25] *(a) and bonding of TEVS on silicon surface* [26] *(b).*

The chemical bonds between the substrate treated with TEVS and SMP10 are created through radical polymerization with the double bonding of the vinyl group of SMP10 and TEVS, respectively. The vinyl group (1) of TEVS is shown in Figure 10 (a, b).

The silicon substrate was immersed into in water free ethanol or n-hexane containing dissolved TEVS, then rinsed with water free ethanol or n-Hexane, respectively and dried with nitrogen. Different immersion times and TEVS solution temperatures were tested and analysed with a KRÜSS drop shape analyser (see also 3.7.3).

3.4. Sample coating

For sample coating, two different approaches were tested, dip coating and spin coating. In dip coating, the silicon sample is immersed in the prepared coating solution and then withdrawn, as shown in Figure 11 where the film thickness is adjusted by the withdrawal velocity, as well as by the viscosity of the coating solution [27].

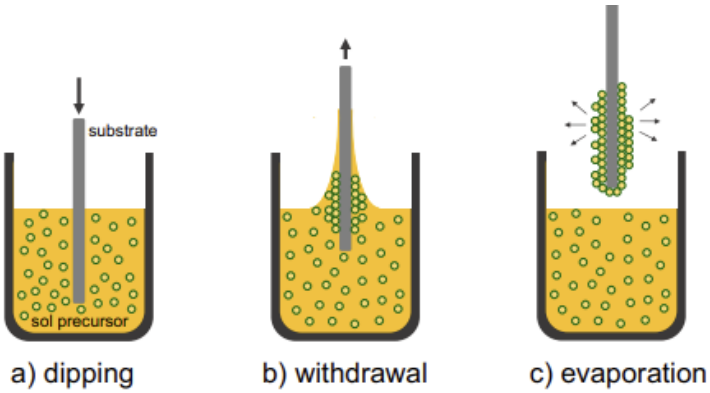

Figure 11: Process of dip coating [28].

Dip coating was done in a beaker, filled with the diluted SMP10, where the sample was withdrawn slowly by hand.

In spin coating, the coating solution is deposited on the sample, which is then rotated, producing a uniform liquid film [27]. The coating liquid adheres on the substrate through adhesive forces, while centrifugal forces acting on the rotating solution result in shearing. This causes a radial flow, leading to most of the coating solution being ejected from the sample [27]. Figure 12 (a) shows this process, combined with evaporation of the solvent, leading to a reduced film thickness.

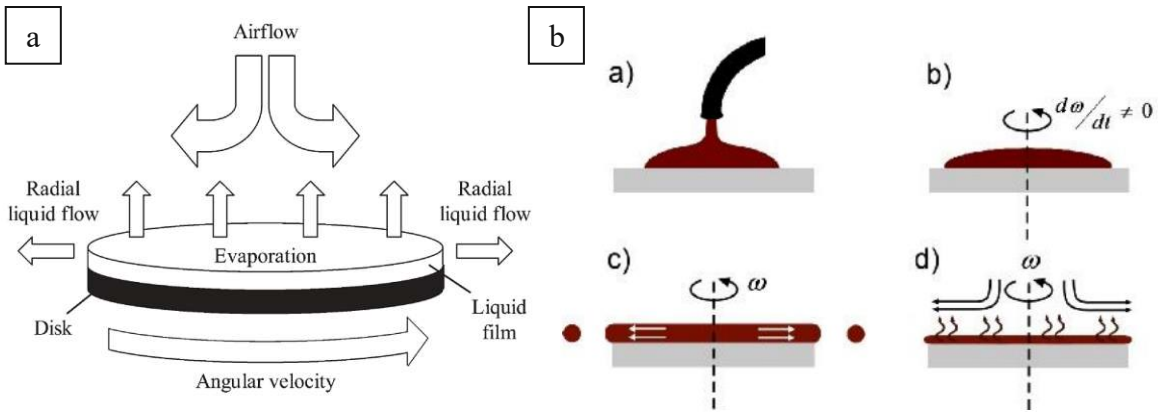

Figure 12: Principle of spin coating [27] *and four stages of spin coating* [29].

Figure 12 (b) shows the four stages of spin coating, according to M. D. Tyona [29]. From a) to d) they are the dispense stage, the substrate acceleration stage, the stage of substrate spinning at a constant rate with fluid viscous forces dominating fluid thinning behavior and the stage of substrate spinning at a constant rate with solvent evaporation dominating the coating thinning behavior. In the disperse stage, the coating fluid is deposited on the sample. This can either be a static process, where the sample stands still, or a dynamic process, where the sample is in low

rotation. In the substrate acceleration stage, the substrate is brought into higher rotations per minute (rpm) of typically between 1500 rpm and 6000 rpm [29], where the substrate rotates faster than the coating fluid, causing an aggressive expulsion of the surplus liquid until the film is thin enough so that the liquid rotates with the same speed as the substrate. This step takes from 10 seconds to several minutes [29]. The third step, the stage of substrate spinning at a constant rate where fluid viscous forces dominate fluid thinning behavior, is characterized by gradual fluid thinning. In this step, edge effects often occur, because the fluid flows uniformly outward, but need to form droplets at the edge to flung of. In the last stage of substrate spinning at a constant rate with solvent evaporation dominating the coating thinning behavior, the evaporation of volatile solvent species become dominant, as the name implies.

For spin coating two different spin coaters were used. The spin coating machine Convac ST146, located in a clean room, where no UV light was allowed, as shown in Figure 13 (a) and a custom-built one, which was used for pre-experiments and spin coating under UV light on the chemical bench, as shown in Figure 13 (b).

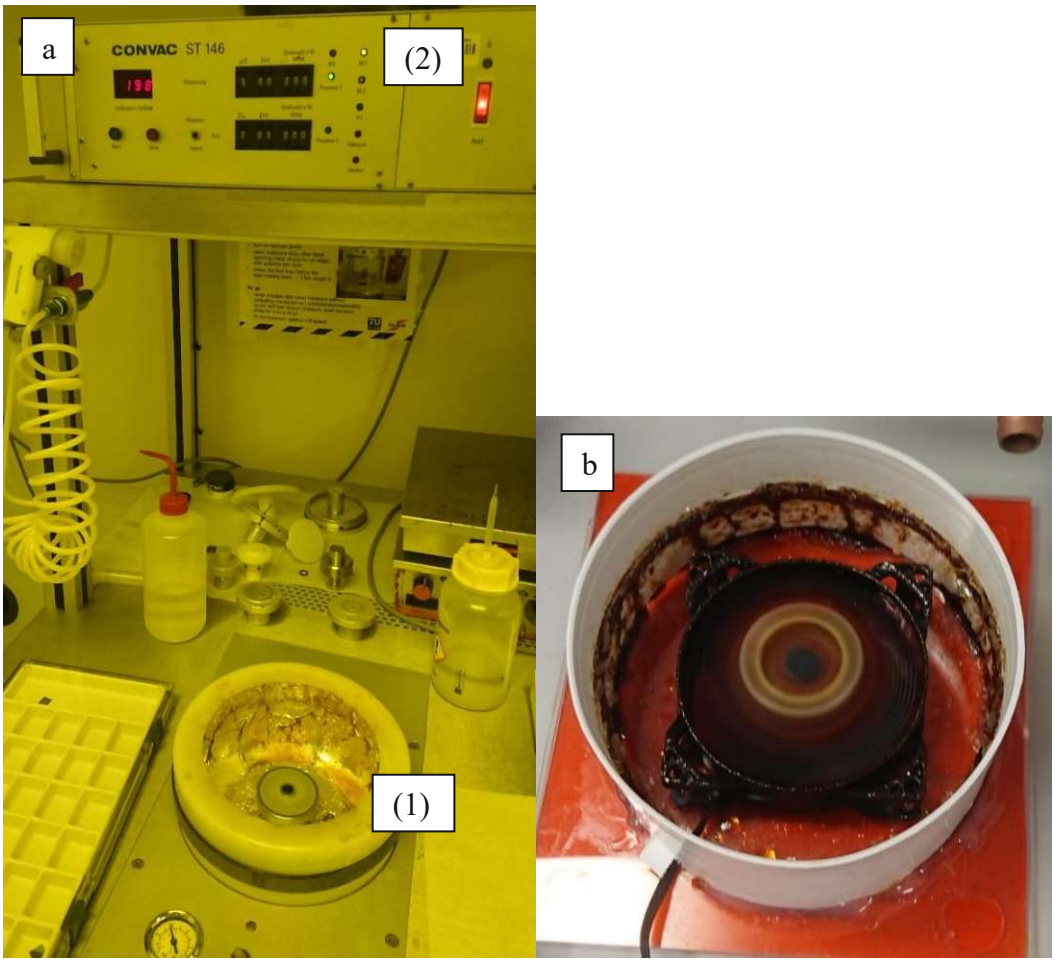

Figure 13: (a) Spin coater in Clean-room, (b) Self-built spin coater for pre-experiments.

Figure 13 (a) shows the professional spin coater in the clean room, where (1) is the sample holder and (2) is the control system. After the sample had been fixed on the sample holder with vacuum, the sample was rotated and cleaned from possible particles with acetone and iso-propanol. Thereafter, the rotation was stopped, and a droplet of coating solution was deposited at the center of the substrate, followed by steep increase of rotation. After the final spinning speed was reached, it was held for a set time until the coating process was finished.

The final film thickness h can be calculated through [27]

$$h = k_1 \omega^{\alpha} \qquad (2)$$

where h is the film thickness, ω the angular velocity and k_1 and α empiric constants. Both constants are dependent on various parameters such as rheology parameters, but α has been observed to be in the close vicinity of -0.5 [27].

Figure 13 (b) shows the self-built spin coater, which was used for pre-experiments and UV spin coating. The operation is similar to the professional one in the clean room, but after the spin process was started, a UV-C lamp was placed over the spin coater. This was only sensible for coating solutions with AIBN, which acts as radical starter under UV-C light. With the UV-C light, the adhesivity between coating solution and substate should be increased. Also, multi coating [30] after polymerization of the coating solution under UV-C light was done to close pinholes, which occurred during spin coating, which may be caused by impurities (e.g. particles), dewetting or outgassing (see 4.1.4 and 4.1.5).

3.5. Annealing

Curing, or the cross linking of the polymer results in an infusible material [31]. For SMP10 the main way for curing is thermal curing but can also be done with UV-C light if additives such as AIBN are added. Thermal curing can be performed in vacuum or inert gas atmosphere [31]. If the atmosphere contains reactive elements, impurities or involuntary results can occur, e.g. SiO instead of SiC can be formed if the oven atmosphere contains oxygen.

Pyrolysis is the thermally activated chemical decomposition of organic material without the presence of oxygen [31]. In this process, the preceramic polymer is converted into amorphous or crystalline SiC.

To perform the annealing process and consistency of curing and pyrolysis, special furnaces with a defined oven atmosphere and exact temperature profiles are needed. Therefore, two different furnaces have been used, shown in Figures 14 and 17.

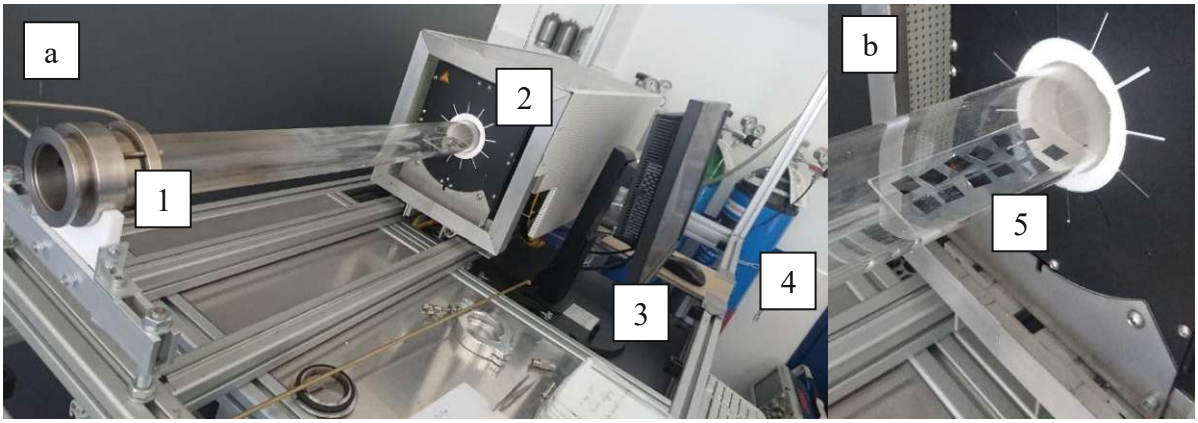

Figure 14: Oven with controlled atmosphere and adjustable temperature profile.

Figure 14 (a) shows the tube furnance with the quarz tube (1) where the samples are loaded, the heat source (2) and the computer system (3). In the background, gas flasks (4) for different oven atmospheres are visible. For annealing, the samples were loaded using a glas plate (5), shown in Figure 14 (b) and the temperature, oven atmosphere and rising-, and holding times were programmed via Matlab. The tube furnance could be operated up to 1000 °C with either under vacuum or in nitrogen atmosphere in the tube. Figure 15 and 16 shows the meassured temperature pressure graphs of the operation condition of the oven.

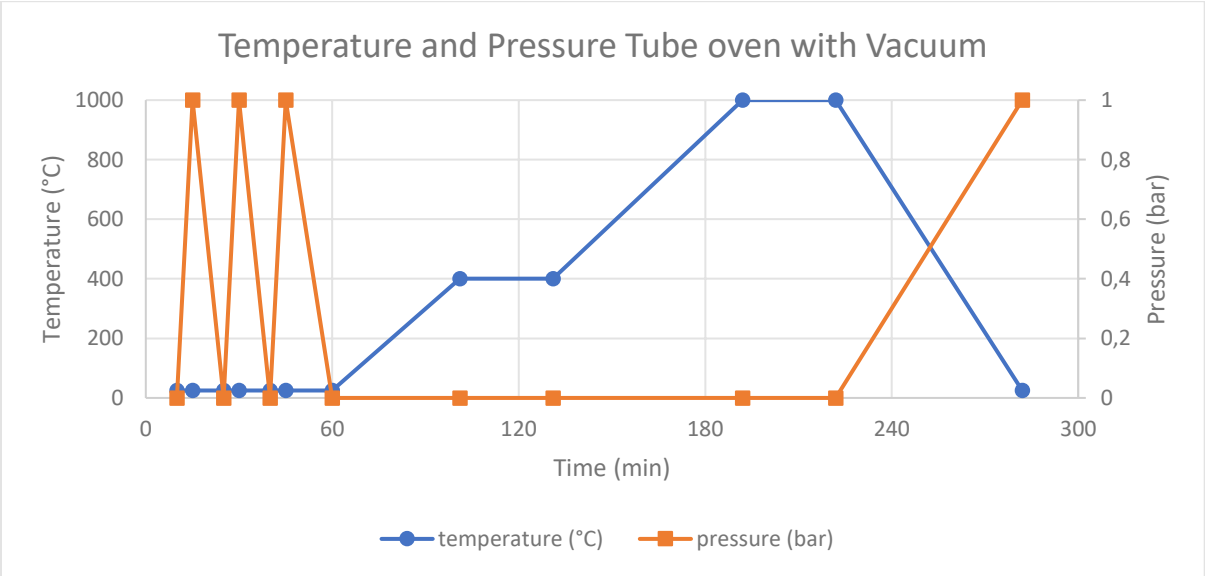

Figure 15: Target temperature and pressure profile of the tube oven, operated under vacuum.

In Figure 15, annealing was done under vacuum conditions (12 mbar). The preassure peaks in the beginning and end of the process are due to nitrogen flushing.

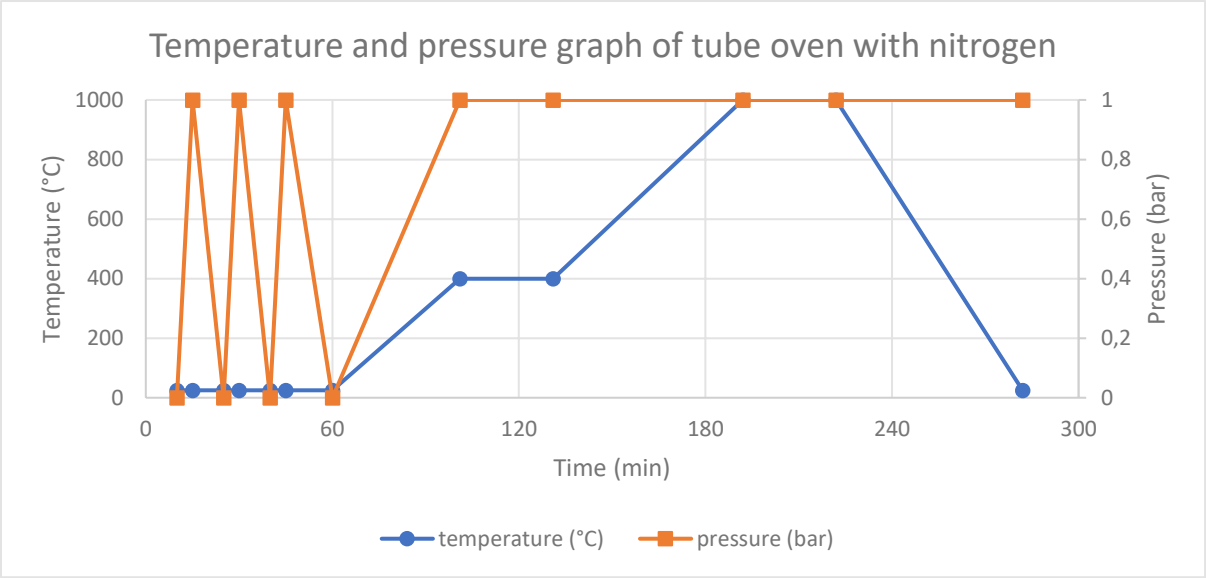

Figure 16: Target temperature and pressure profile of the tube oven, operated with N_2.

In Figure 16, the oven is operated under nitrogen atmosphere. To flush out remaining air, vaccum (12 mbar) was applied 4 times in the beginning, and nitrogen was used for flushing.

Since analyses showed, that the samples from the tube furnance where oxidized during pyrolisis (see section 4.1 for details), with the supposed reason of a problem with the tightness of the oven atmosphere, the low pressure chemicel vapor depostion equipment was used as alternative to the tube furnace for pyrolysis.

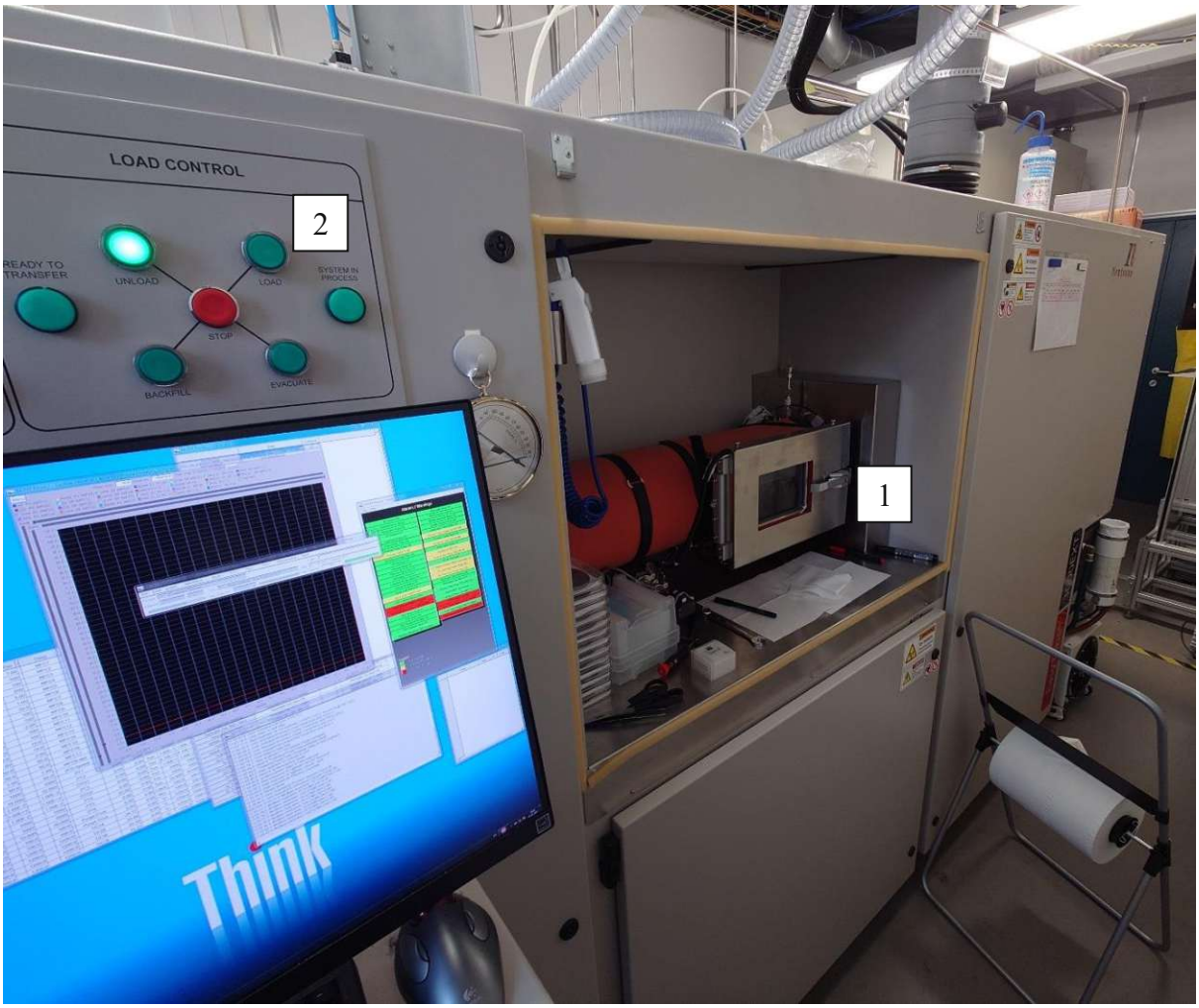

Figure 17: LPVCD used for annealing experiments.

In Figure 17 the used LPCVD is shown. The samples were loaded through a load lock system (1) and the programming was done with the control system (2). Figure 18 shows the temperature profile used with the LPCVD. In contrast to the tube furnace, the samples in the LPCVD were annealed at a higher temperature of 1200 °C and under an Argon atmosphere.

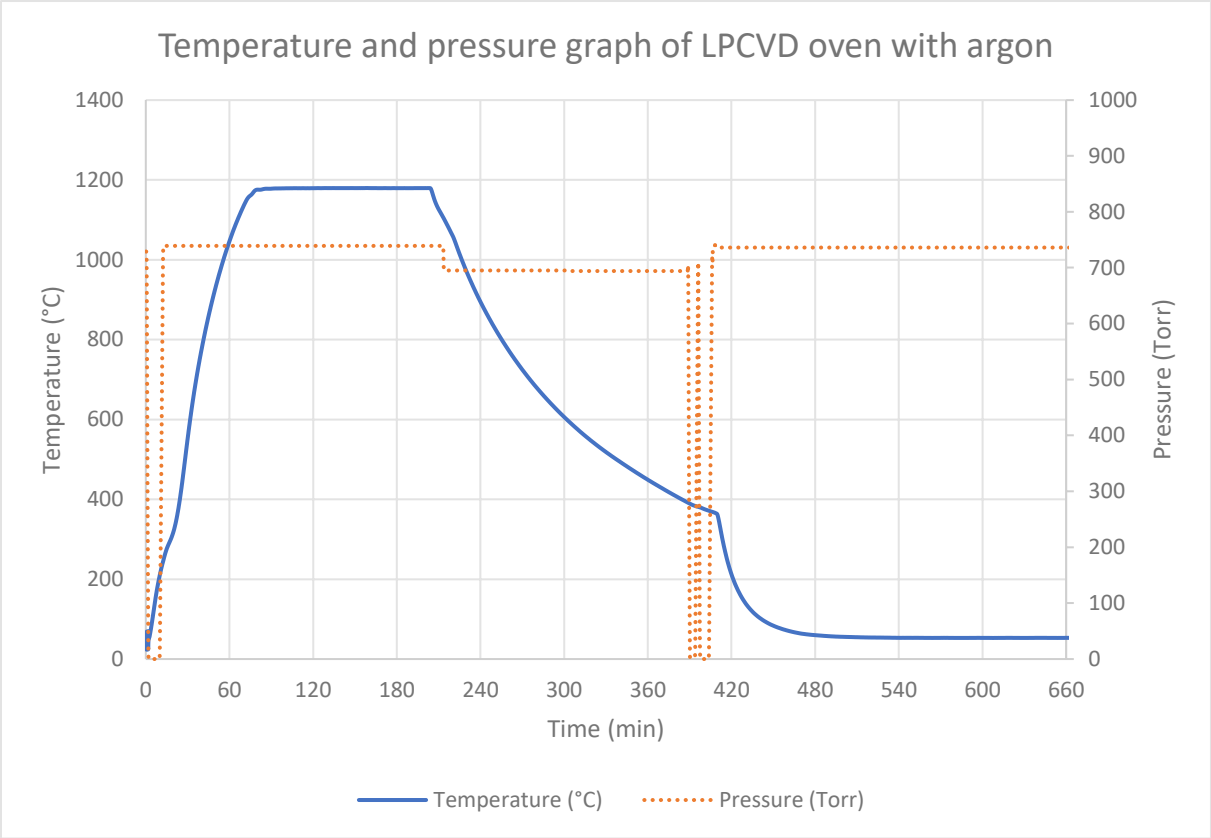

Figure 18: Meassured temperature and pressure profile of the LPCVD oven, operated with Argon.

In Figure 18, the temperature and pressure graph of LPCVD, operated under argon atmosphere, is shown. The pressure drops in the beginning were caused by the vacuum pump to rid the air in the oven. The pressure drops at minute 400 were caused by unloading the samples.

3.6. UV Exposure

For samples with AIBN admixed to the coating solution, the possibility of greening under UV-C light was given, since AIBN acts as radical starter [21] for the polymerization of SMP10. This was tested with two 18 W UV-C tubes installed under a wooden hood with orange acrylic glass on the side to prevent eye damage due to the UV-C radiation. Figure 18 shows the used UV-C hood.

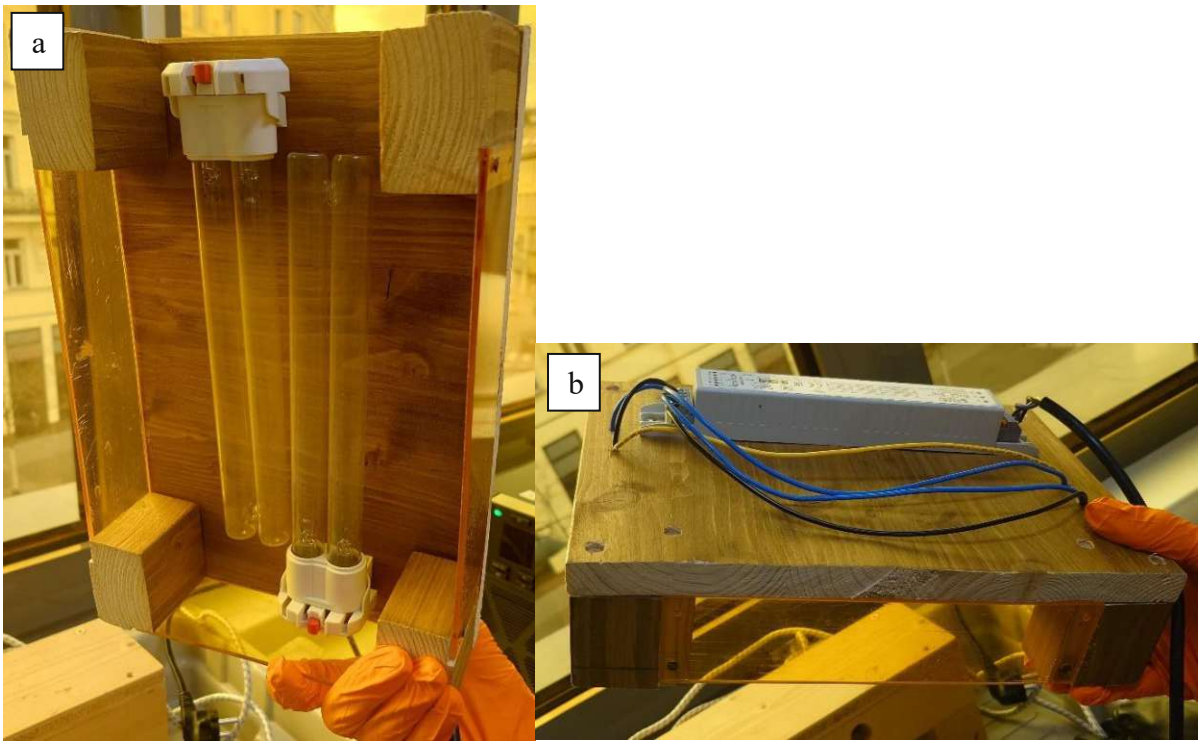

Figure 19: UV-C hood for greening samples coated with SMP10 and AIBN.

Figure 19 (a) shows the bottom side of the hood with the installed lamps, while Figure 19 (b) shows the top of it with the transformer for powering the lamps. For curing the samples with UV-C light, the spin coated silicon samples have been exposed to the light for 60 minutes. Thereafter, the pyrolysis was done in the oven.

3.7. Sample characterisation

To characterize the produced samples, different analytical methos were used such as optical microscopes, FTIR, XRD or SEM. With the used methods the qualitative and quantitative evaluation of the surface, the thickness of the layers, the level of surface modification and the chemical composition, as well, as the crystallographic composition of the thin film were analyzed.

3.7.1. FTIR Analysis

Fourier Transformed InfraRed (FTIR) analysis was used to track the state of the polymer film, since SMP10 as well as highly doped Si, and SiC are infrared (IR) active [32], which means, that these materials absorb the infrared light through molecule vibration, which can be measured by an infrared spectrometer [33]. For the measurements a Bruker Tensor 27 FTIR spectrometer

with the A510/Q Reflexion/Transmission cell was used. The measurement principle is shown in Figure 20 [34].

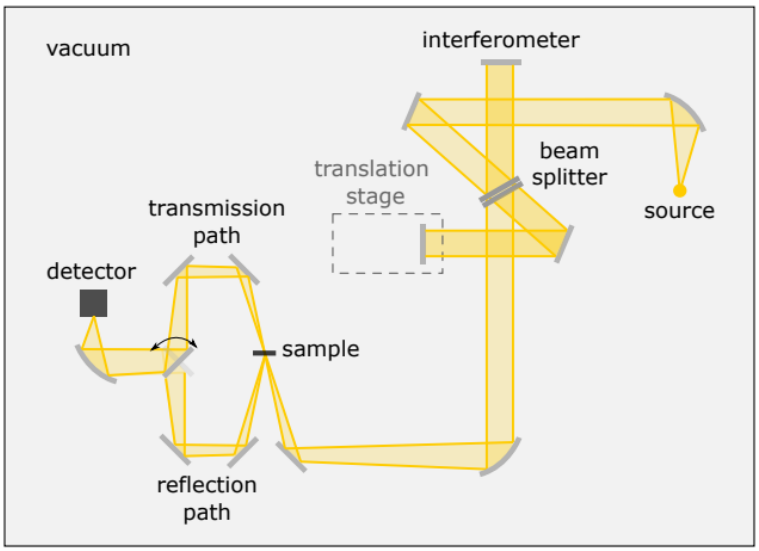

Figure 20: Principle of IRRA spectroscopy [34].

To measure thin films, the measured spectra of the used Si wafer had to subtracted from the measured spectra of the sample. The absorption of any material can be quantified by the absorption coefficient α [34]

$$\alpha = -\frac{1}{l} \cdot \ln \frac{I(l)}{I_0} \qquad (3)$$

where $I(l)$ is the intensity of light at a depth l, and I_0 is the initial intensity of light at the surface of the material ($l = 0$). I_0 can be expressed with [34]

$$I_0 = I_{Device} - R \qquad (4)$$

where I_{Device} is the intensity provided by the spectrometer and R the measured reflectance. For a sample of thickness d, the directly measured quantity is a dimensionless absorbance A [34]

$$A = -\ln \frac{I}{I_0} \qquad (5)$$

where I is the intensity of light measured after passing through the sample. With the value of d is the thickness of the Si substrate, the absorption coefficient can be calculated from the measured absorbance as

$$\alpha = \frac{A}{d} \qquad (6)$$

For the Si substrate without a thin film, the measured transmitted light I_1 can then be expressed through

$$I_1 = I_0 \exp(-\alpha d) \qquad (7)$$

where the factor αd known through

$$\alpha(\lambda) d = -\ln \frac{I_1(\lambda)}{I_0(\lambda)} \qquad (8)$$

where λ is the is the wavelength of the measurement light.

With the thin film on the Si substrate with the unknown thickness x, the transmitted light I_2 through the thin film and the Si substrate can be expressed as

$$I_2 = I_1 \exp(-\alpha' x) \qquad (9)$$

and $\alpha' x$ can be written as

$$\alpha' x = -\ln \frac{I_2}{I_1} = f(\lambda) \qquad (10)$$

Where $f(\lambda)$ is the FTIR spectra of the thin film. The used FTIR spectrometer is shown in Figure 21.

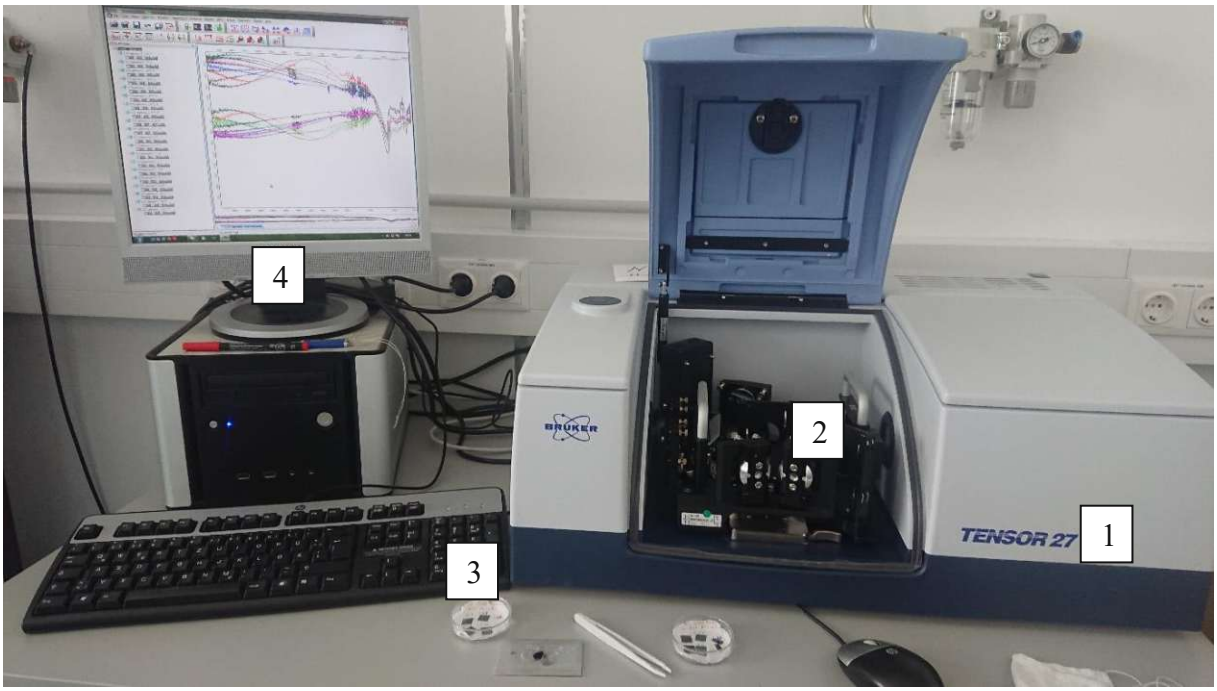

Figure 21: FTIR Spectrometer Bruker Tensor 27.

In Figure 21 the FTIR spectrometer Bruker Tensor 27 (2) is shown with the Reflection/Transmission cell (2), the sample holder (3) and samples, and the computer with the analysis software (4).

3.7.2. Microscopy

Microscopy: For the analysis of the surface and the cross-section of the samples, optical microscopes, and a scanning electron microscope (SEM) were used.

For the optical microscopy a Zeiss Axio Scope A1 reflected light microscope with a Zeiss AxioCam ICc1 camera was used. The principle of reflected light microscope is shown in Figure 22.

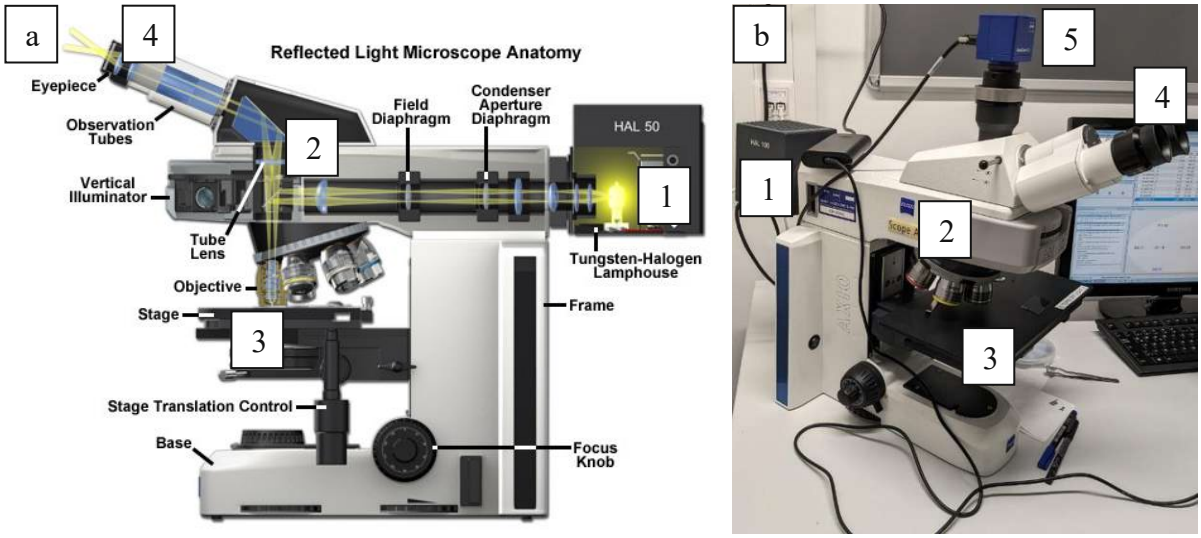

Figure 22: Principle of reflected light microscope [35].

In Figure 22 (a), the principle of the optical microscope is shown. The light from the light source (1) is coupled into the optical magnification pathway via a beamsplitter (2), where it is reflected from the sample on the stage (3) through the objective and projects the magnified image of the sample through the ocular (4) or on the camera, respectively. In Figure 22 (b) the used microscope is shown, which has additional a trinocular tube head with the Zeiss AxioCam ICc1 camera mounted (5).

In a SEM, an electron beam is formed by the electron source and accelerated toward the specimen using a positive electrical potential, Figure 23 (a). The electron beam is confined and focused into a thin, focused, monochromatic beam, using magnetic lenses [36]. The electrons of the beam interact with the sample, generating Auger, backscattered and secondary electrons

which contain information about its composition, atomic numbers, and surface topography respectively [36]. The secondary electrons from the sample, which contain the topographical information, are detected in the collector system, and transformed into an image. The structure of a SEM and the used SEM are shown in Figure 23.

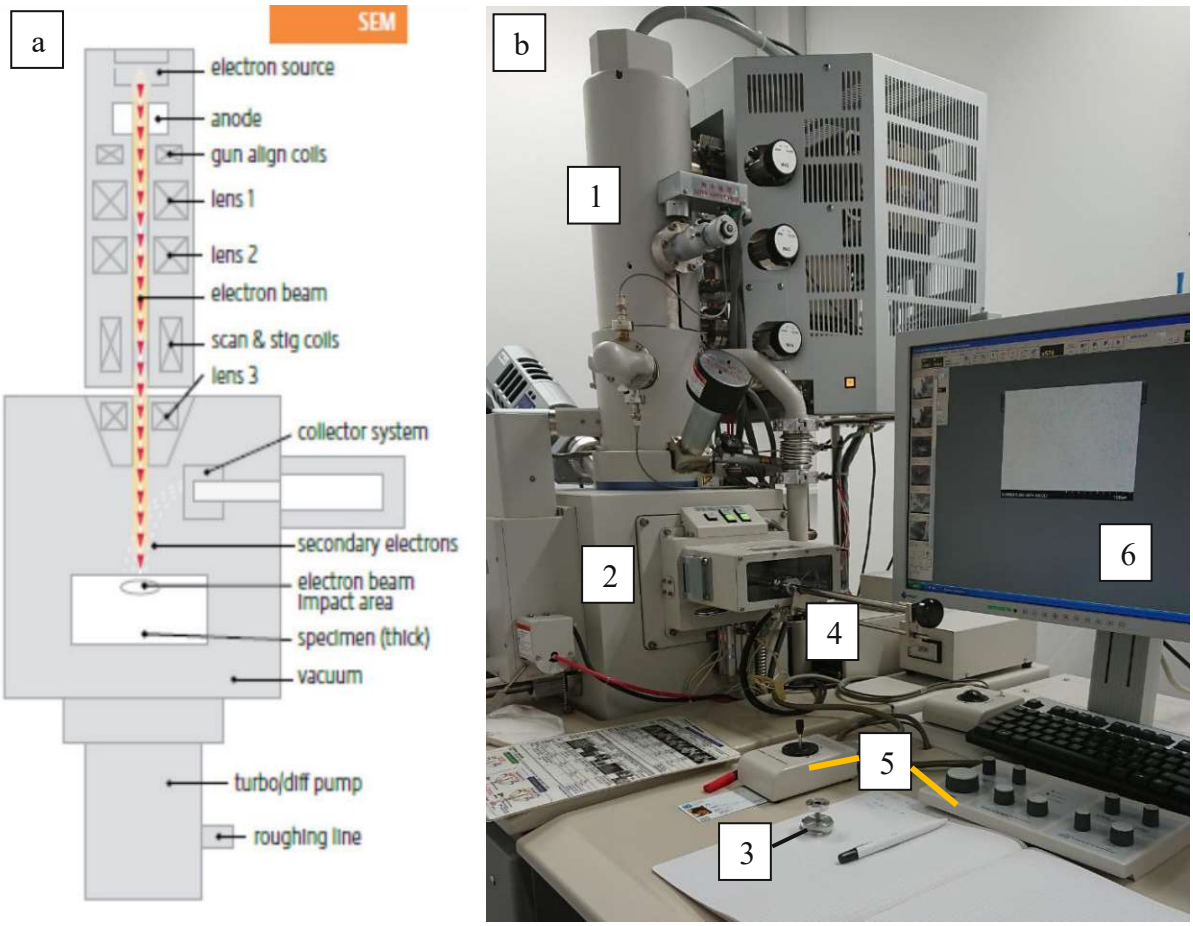

Figure 23: Structure of a SEM [36] *(a), used SEM (b).*

In the electron column (1) in Figure 23 (b) the electron beam is generated under vacuum, focused to a small diameter, and scanned across the surface of a specimen by electromagnetic deflection coils [36]. In the specimen chamber (2) the sample (3) can be loaded through a lock system (4). With the manual stage control (5) the sample can be manipulated in the specimen chamber for x-y-z movement, zoomed or tilted. The generated image is then displayed on the monitor (6). Figure 24 shows the sample holder with an attached sample.

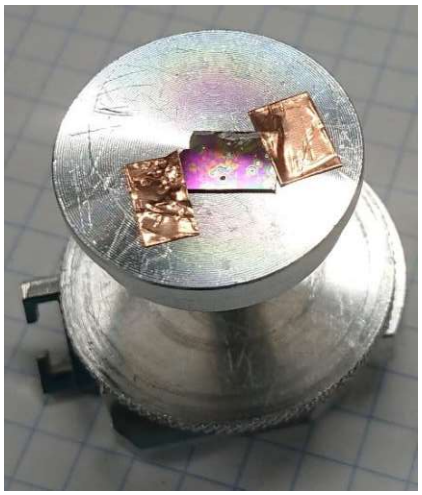

Figure 24: Sample holder with sample.

The sticky copper foil in Figure 24 is used to electrically connect the sample with the sample holder to minimize or avoid electrostatic charges.

3.7.3. Contact angle measurement

To gain information about the surface energy of a sample, the contact angles of known test liquids on the surface can be measured with a contact angle measurement device, which allows the calculation of the surface energy of the sample. The contact angle testing is schematically shown in Figure 25.

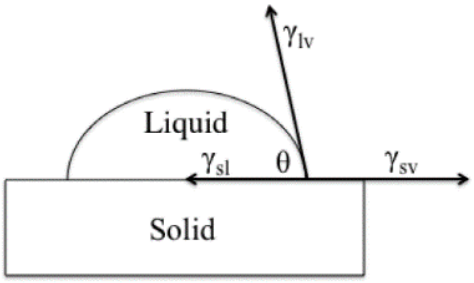

Figure 25: Cross-sectional schematic of a droplet placed on a surface [37].

Figure 25 shows the wetting of the solid, characterized by the contact angle, which is defined as the angle between the tangent to the liquid–vapor interface and the solid surface at the three-phase contact line [38]. With the Young equation, the contact angle between liquid and an ideal solid surface can be described [38],

$$\cos\Theta = \frac{\gamma_{sv}-\gamma_{sl}}{\gamma_{lv}} \qquad (11)$$

where θ is the Young contact angle, γ_{sv} and γ_{sl} the solid–vapor and solid–liquid interfacial tensions, respectively, and γ_{lv} the surface tension of the liquid [38]. Water and diiodomethane were used as testing liquids with different, known polar and dispersive components, which are listed in Table 1 [37]. The surface energy of the sample γ_{sv} can be calculated with [39]

$$\gamma_{sv}^{d} = \left[\frac{(\gamma_D\sqrt{\gamma_W^p}(1+\cos\theta_D)-\gamma_W\sqrt{\gamma_D^p}(1+\cos\theta_W))}{2(\sqrt{\gamma_D^d\gamma_W^p}-\sqrt{\gamma_W^d\gamma_D^p})}\right]^2 \qquad (12)$$

$$\gamma_{sv}^{p} = \left[\frac{(\gamma_W\sqrt{\gamma_D^d}(1+\cos\theta_W)-\gamma_D\sqrt{\gamma_W^d}(1+\cos\theta_D))}{2(\sqrt{\gamma_D^d\gamma_W^p}-\sqrt{\gamma_W^d\gamma_D^p})}\right]^2 \qquad (13)$$

$$\gamma_{sv} = \gamma_{sv}^{d} + \gamma_{sv}^{p} \qquad (14)$$

The indices W and D stand for water and diiodomethane, respectively.

Table 1: total energy γ_{lv}, polar energy γ_{lv}^{p} and dispersive energy γ_{lv}^{d} of the test liquids [39].

Test liquid	γ_{lv}	γ_{lv}^{p}	γ_{lv}^{d}
Water (W)	72,8	51,0	21,8
Diiodomethane (D)	50,8	0,0	50,8

The surface energy in this approach is expressed as a sum of a dispersive surface energy and a polar surface energy, as shown equation 14. The dispersive surface energy represents the molecular interaction due to London forces, and the polar surface energy consist of all other interactions due to non-London forces [40].

The contact angles θ were measured with the Krüss DSA30 drop shape analyzer, shown in Figure 26.

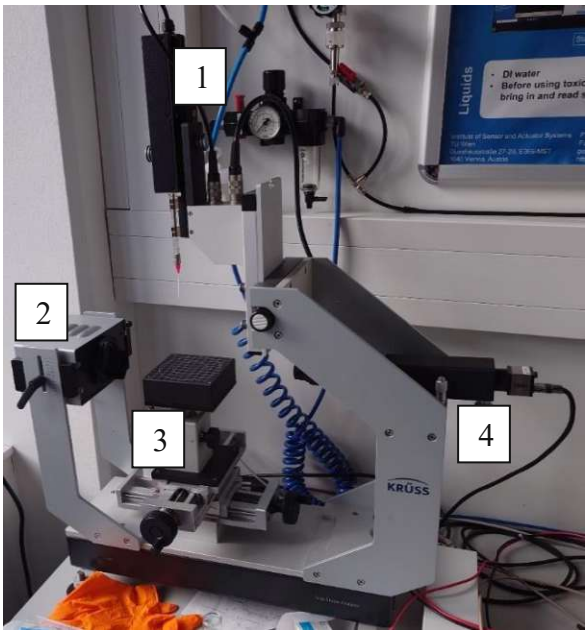

Figure 26: Krüss DSA30 drop shape analyzer for contact angle measurements.

The drop shape analyzer in Figure 26 consists of the drop shaper (1), a motor driven pipette, a light source (2), sample holder (3) and a camera (4). The pictures taken with the camera can be automatically analyzed with a computer.

3.7.4. XRD

With an X-ray diffractometer, the structure of crystals can be determined. Therefore, an X-ray is fired from different angles at the sample and the diffracted beam is measured. The principle is shown in Figure 27.

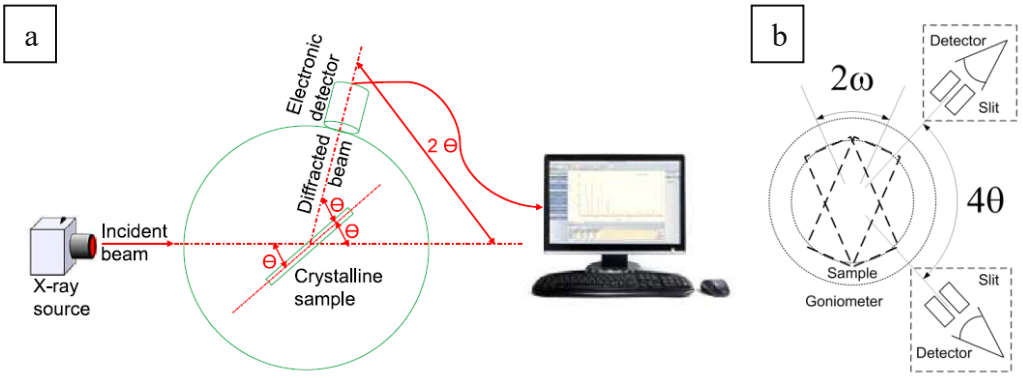

Figure 27: Schematic on the measurement principle of XRD technique [41] *(a) used principle* [42] *(b).*

Typically, a copper (Cu) anode in a sealed tube emits a Cu Kα1, Cu Kα2 and Cu Kβ radiation. A monochromator allows only the Kα1 to pass and produces a narrow band of wavelengths

through Soller slits of collimated x-rays (λ), and directs it to the sample. The sample diffracts the radiation at angles that obey Bragg's Law [41]

$$n\lambda = 2d_{hlk} \sin\theta \qquad (15)$$

Where n is an integer (1, 2, 3, …), d_{hlk} marks the interplanar spacing generating the diffraction, and θ is the x-ray incident angle [41]. The radiation diffracts at discrete directions in space and a detector records these signals while the x-ray source and detector move in an arc over the sample. The position and intensity of the signals relate to the identity and position of the atoms in the unit cell, which can be searched through patterns in a database. The basic principle is shown in Figure 27 (a), while Figure 27 (b) shows the principle of the used XRD device, where the source and the sensor move together around the sample, that rotates with ω. Figure 28 shows the used PANalytical X'Pert Pro diffractometer in Bragg-Brentano geometry with Cu $K_{\alpha 1,2}$ radiation, a BBHD mirror filter, and a X`Celerator line-detector.

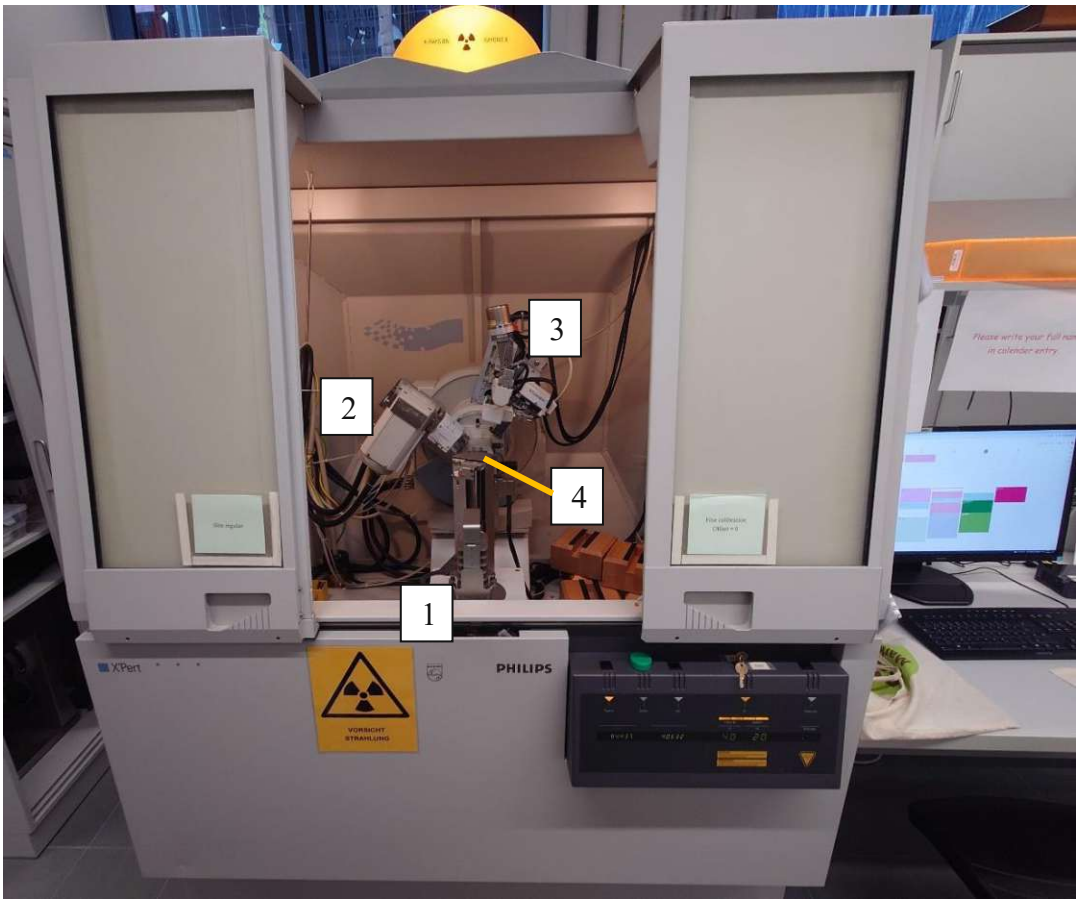

Figure 28: XRD from Panalytical X'Pert.

In Figure 28, the sample magazine (1), the x-ray source (2) and the detector (3) are shown. The examined sample (4) rotates around its own axis while be scanned. The samples on the sample holder are shown in Figure 29.

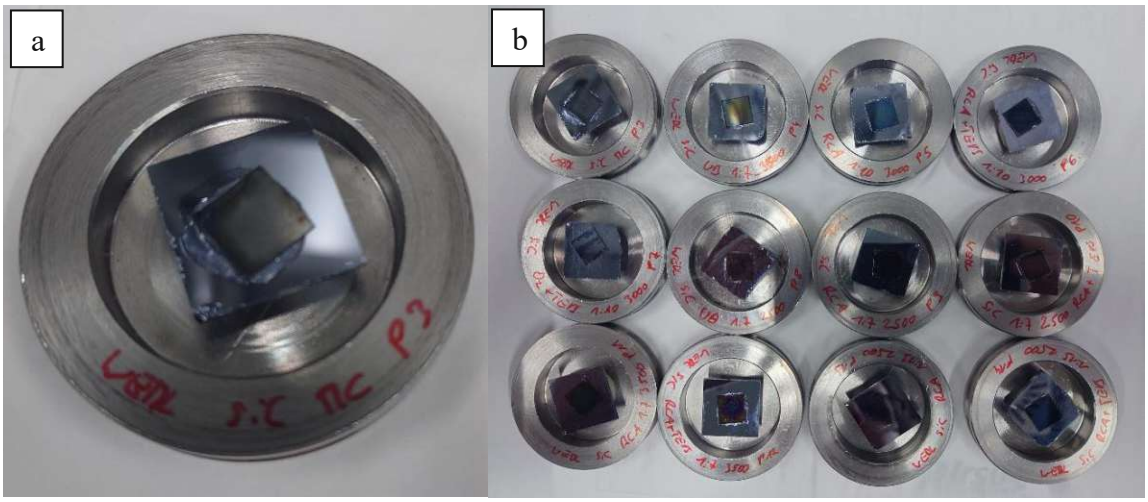

Figure 29: Sample holder with sample for XRD measurement, single sample (a), samples for batch processing (b).

Figure 29 (a) shows a single sample and (b) the examined sample of one batch in the sample holder (magazine). The sample was adhered with Vaseline on a Si (111) carrier crystal and adjusted in height, so that the sample holder and the sample were on the same level. For the height adjustment, flexible, adhesive putty was used.

3.7.5. Reflectometric thin film measurement

To measure the thickness of a thin film non-invasively, the reflectometric thin film measurement was used. In this measurement method, the reflection spectrum of the thin film is analysed. Therefore, light, consisting of visible, UV and near IR light, is irradiated on the sample and the reflections are measured. This was done with a measurement device from Filmetrics as shown in Figure 30.

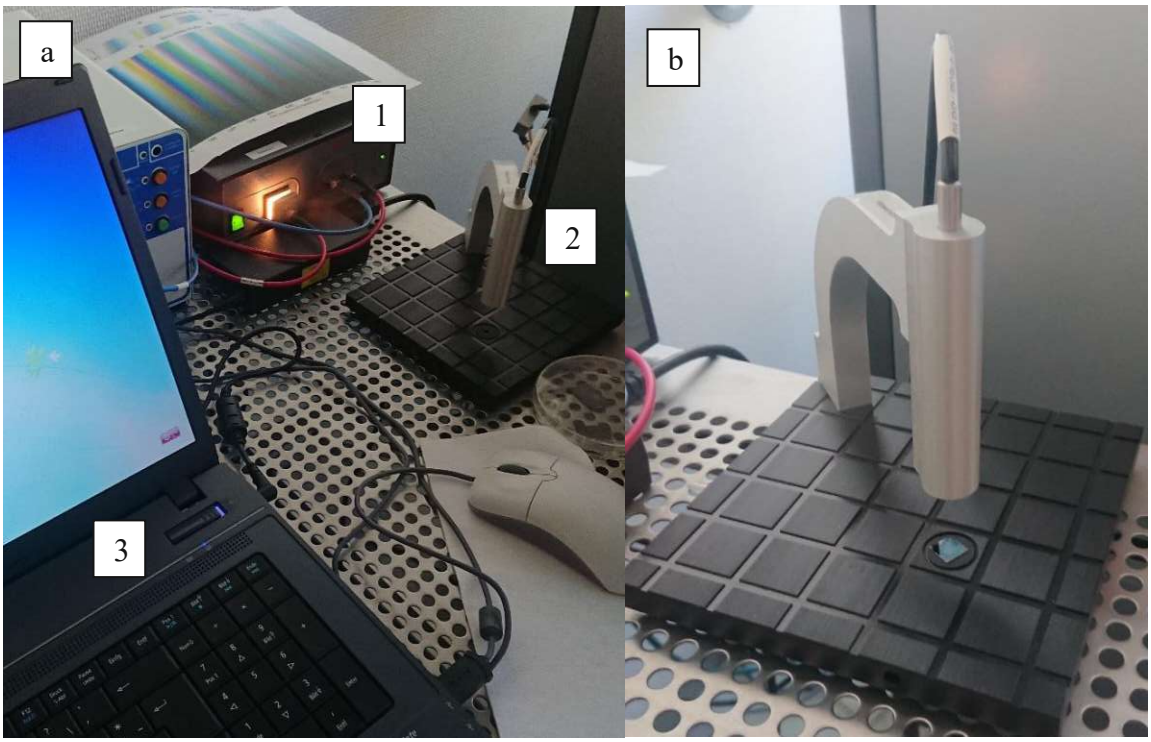

Figure 30: Apparatus from Filmetrics for measuring the film thickness.

In Figure 30 (a) the whole setup can be seen with the light source (1) the sensor for irradiation and detection of the reflection spectrum (2) and the computer for analysis (3). In Figure 30 (b) the sensor with a sample beneath is shown.

For accurate measurements, the device had to be calibrated with a bare silicon wafer without a thin film on top before each use. The measurement principle and typical reflection spectrum are shown in Figure 31 [43].

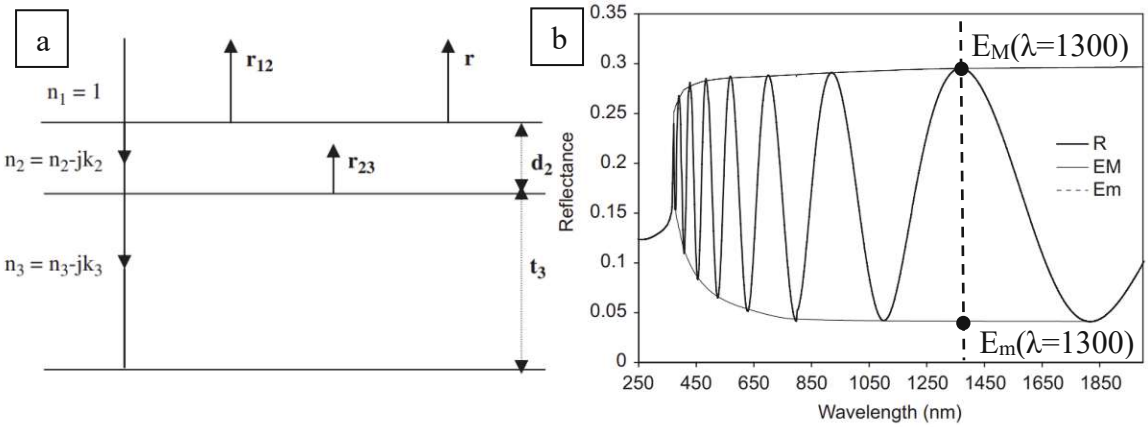

Figure 31: Model of film substrate system (a) and typical measured reflection spectrum of a thin film measurement (b) adapted from [43].

To gain the thickness of the film, the approximate values must be retrieved from the experimental reflectance measurement. In a first step the envelopes $E_M(\lambda_{extr})$ and $E_m(\lambda_{extr})$ as

shown in Figure 31 (b) are drawn. Then the maxima $E_M(\lambda_{extr})$ and the minima $E_m(\lambda_{extr})$ are extracted from the envelopes with their corresponding wavelength λ_{extr} and written in a list. Next every reflectance coefficient at the first interface r_{12}, see Figure 30 (a), between surface and air must be calculated for every λ_{extr} by using the extracted $E_M(\lambda_{extr})$ and $E_m(\lambda_{extr})$ values [43].

$$r_{12} = \frac{\left(1+E_m^{\frac{1}{2}}(\lambda_{extr})E_M^{\frac{1}{2}}(\lambda_{extr})\right) \pm [(1-E_M(\lambda_{extr}))(1-E_m(\lambda_{extr}))]^{\frac{1}{2}}}{[E_M^{\frac{1}{2}}(\lambda_{extr})+E_m^{\frac{1}{2}}(\lambda_{extr})]} \quad (16)$$

With r_{12}, n_2 can be calculated from Fresnel formula [43]

$$r_{12} = \frac{1-(n_2-ik_2)}{1+(n_2-ik_2)} \quad (17)$$

Where n_2 is the real part of the refractive index and k_2 is the imaginary part and $n_2 \gg k_2$.

In the next step the approximate initial values for the film reactive index n_{20} are calculated [43]

$$n_{20} \approx \frac{(1+r_{12})}{(1-r_{12})} \quad (18)$$

The approximate values for the film thickness d can be calculated for the wavelength of maxima and minima of reflection through [43]

$$d = \frac{\lambda_1\lambda_2}{4(\lambda_1 n_2-\lambda_2 n_1)} \quad (19)$$

In a further step, the obtained values for n_{20} are used with the values of d to calculate P for each extreme wavelength with

$$2nd = P\lambda_{extr} \quad (20)$$

The final film thickness d is calculated from this equation (19) using the obtained values of P and n_{20} for each extreme wavelength. The average final film thickness $\bar{d}$ is calculated for all wavelengths.

3.8. Experimental Procedure

The aim of the experiments was finding a method to manufacture a coherent, dense layer of SiC on a Si-Wafer. Therefore, two different methods have been tested, the immersion drawing process and the spin coating process. Since only the spin coating process was conducted successfully, the correlation between the dilution and solvent of the SMP10, the spinning speed,

the cleaning and modification of the surface and the layer thickness after curing (greening) and sintering of the samples and the possibility of doping of the resulting SiC film was investigated.

In the general process, the Si-wafer (n-Si, p-Si and undoped Si) was cleaned and spin coated with a SMP10 solution. After the sample was first dried, it was then greened at 400 °C or UV-C light and finally sintered at 1000 °C or 1200 °C in furnaces with different atmospheres. Therefore, the following experiments were carried out as shown in Table 2.

Table 2: Carried out experiments.

Experiments	*Remark*
SMP10 on Si wafer without cleaning or modification	with different dilutions of SMP10 and rpm
SMP10 on Si wafer with O_2 plasma cleaning	with different dilutions of SMP10 and rpm
SMP10 on Si wafer with Piranha acid clean	with different dilutions of SMP10 and rpm
SMP10 on Si wafer with RCA clean	with different dilutions of SMP10 and rpm
SMP10 on Si wafer with RCA clean and TEVS surface modification	contact angle measurement to determine the time needed in TEVS solution
Changing solvent for dilution of SMP10	repeating all previous experiments
Adding doping agent (Durazane) to SMP10	
Adding radical starter with doping properties (AIBN) to SMP10	- Polymerization through UVC light - Polymerization through temperature
Using different oven atmospheres	
UV spincoating	- Spin coating under UV light - Start polymerization of droplet on Si wafer and then start spin coating - Double spin coating after polymerizing of the first layer
Double spin coating after pyrolysis	

For all steps FTIR, SEM and layer thickness (Filmetrics) measurements have been performed. The varied parameters of the experiments are summarized in the Appendix 7.1.

To carry out the experiments systematically, the concept of Design of Experiment (DoE) was used [44]. In this particular application of a DoE design, instead of many different experiments, only 5 experiments are carried out, where two variables of the experiment are varied, forming

4 experiments with “extreme” values and one in the center of these 4 experiments. After analysis of the obtained samples from the 1st trial experiments, the sample with the best result forms the new corner experiment in direction of the trend for the best results (Figure 32) for the next (2nd) trial. At least three samples have been prepared, processed, and analyzed of every experiment in each trial. With this method, more information can be obtained with less experiments, and one will less likely miss the true optimum. A contour and Pareto plot will help for analysis and finding the optimum, where the contour plot represents the trend, and the Pareto plot represents the most influent parameters. A visualization of the experiment planning and the trials are shown in Figure 32.

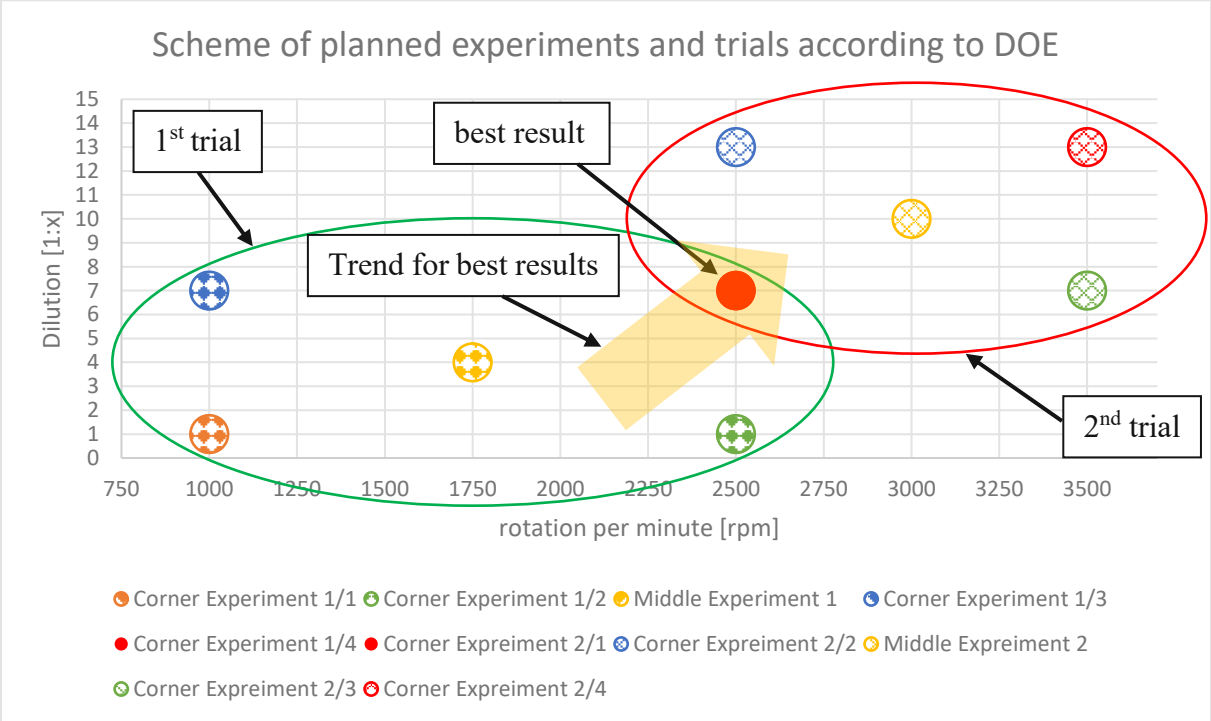

Figure 32: Scheme of planned experiments and trials according to DoE.

The varied variables were the dilution of the spin coating SMP10 solution and the rotation of the spin coater on differently cleaned and modified Si substrates. For evaluation, the adhesion of the thin film and the quality of the surface, through rating of the surface seen through the optical microscope, e.g. coherence, or the number of defects were used for the first DoE and the film thickness for the last DoE.

With the contour plot settings that will maximize or minimize the response variable are determined and the settings for the next iteration of the experiment can be identified. With the Pareto plot, the parameters with the biggest influence are filtered out and listed by their

importance [45]. The program to analyze the results of the experiments done with DoE is shown in the Appendix 7.3.

To find the starting parameters, a small series of experiments with dilutions from 1:1 to 1:100 in steps of 1:10 were conducted with spin coating rotations recommended in literature [29] between 1000 rpm and 5000 rpm in steps of 500 rpm.

4. Results and Discussion

In this chapter, the results of the thin film production as well as the measurement results will be presented and discussed.

4.1. Results

In this chapter, the results of the analysis of the carried-out experiments will be presented. Starting with the examination of the chemical progress through FTIR analysis, the effectiveness of the surface treatment will be shown through contact angle measurement, followed by the non-invasive measurement of the film thickness, which will also be validated with the SEM. Also, the surface will be evaluated through the optical microscope and the crystallinity will be verified through the XRD results.

4.1.1. FTIR

With the FTIR, the formation of SiC can be determined. Therefore, the liquid film on the Si substrate samples had been measured, where the spectrum of the pure Si substrate was subtracted according to the equations 3 – 10. The spectrum of p-Si and n-Si, according to step 2 in Figure 6, is shown in Figure 33, while the spectrum of liquid SMP10 for different dilutions, according to step 3 in Figure 6, is shown in Figure 34. The spectra were obtained using equation 3 – 10.

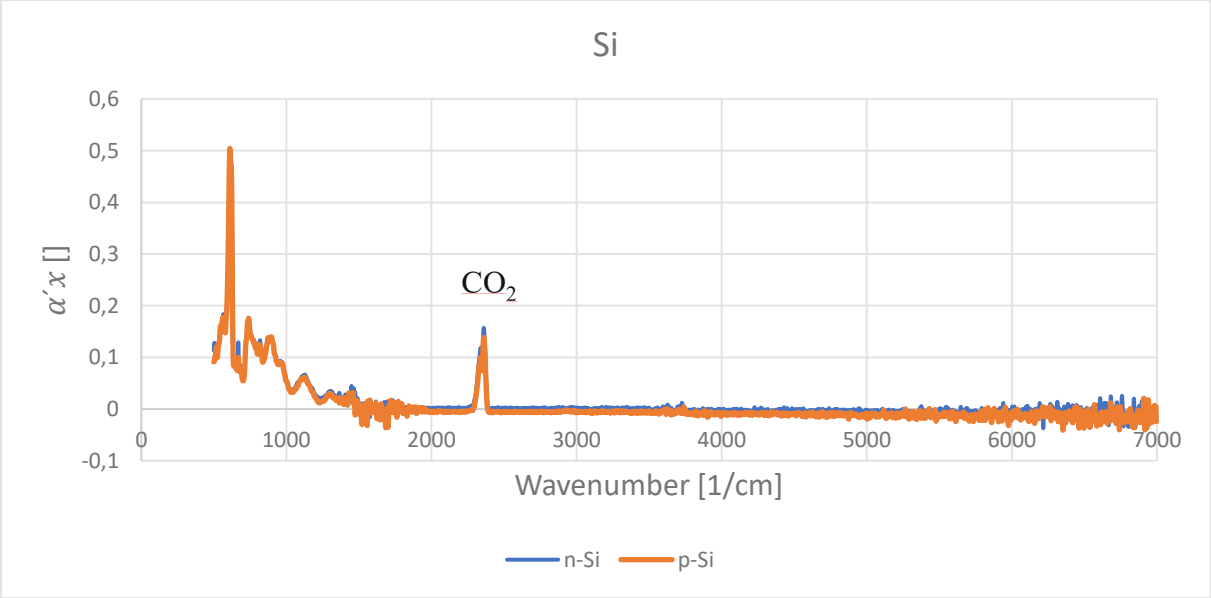

Figure 33: FTIR spectrum of n-Si and p-Si.

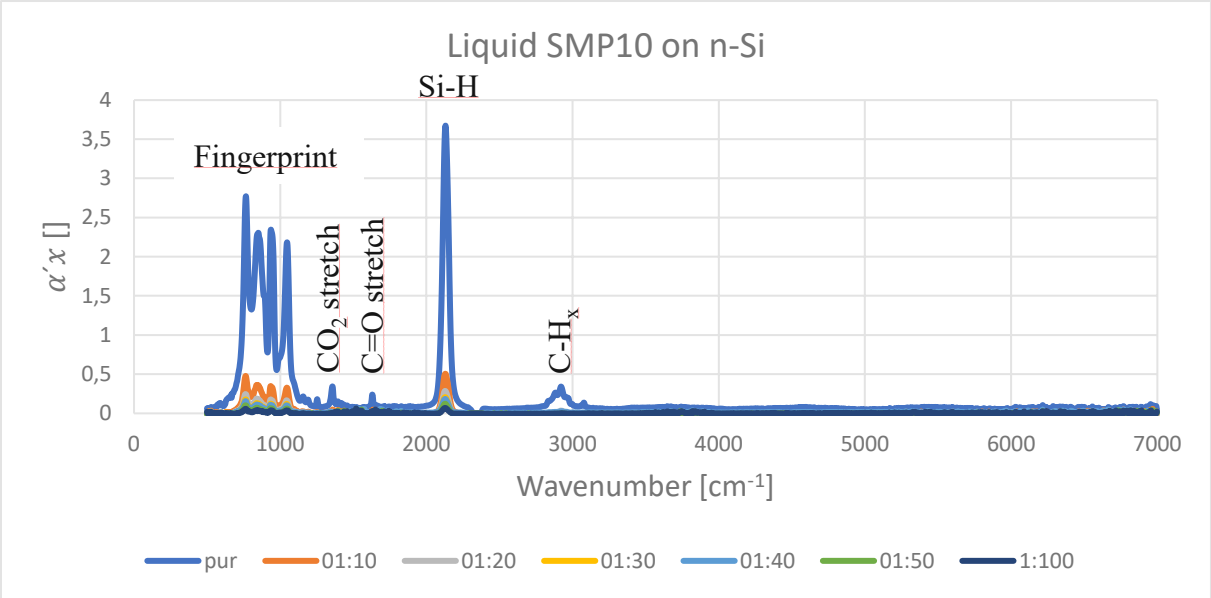

Figure 34: FTIR spectrum of liquid SMP10.

In Figure 34, the intensity of the spectra decreases with the dilution of SMP10 (1:1 to 1:100), which was to be expected, since the solvent should have been evaporated throughout the spin coating process, leading to a decreased film thickness.

After greening, step 4 in Figure 6, and after pyrolysis in the oven, step 5 in Figure 6, a new FTIR measurement of the thin film was taken. The results of the greened thin film and of the pyrolyzed thin film for different coating concentrations of SMP10 are shown in Figure 35 and Figure 36, respectively.

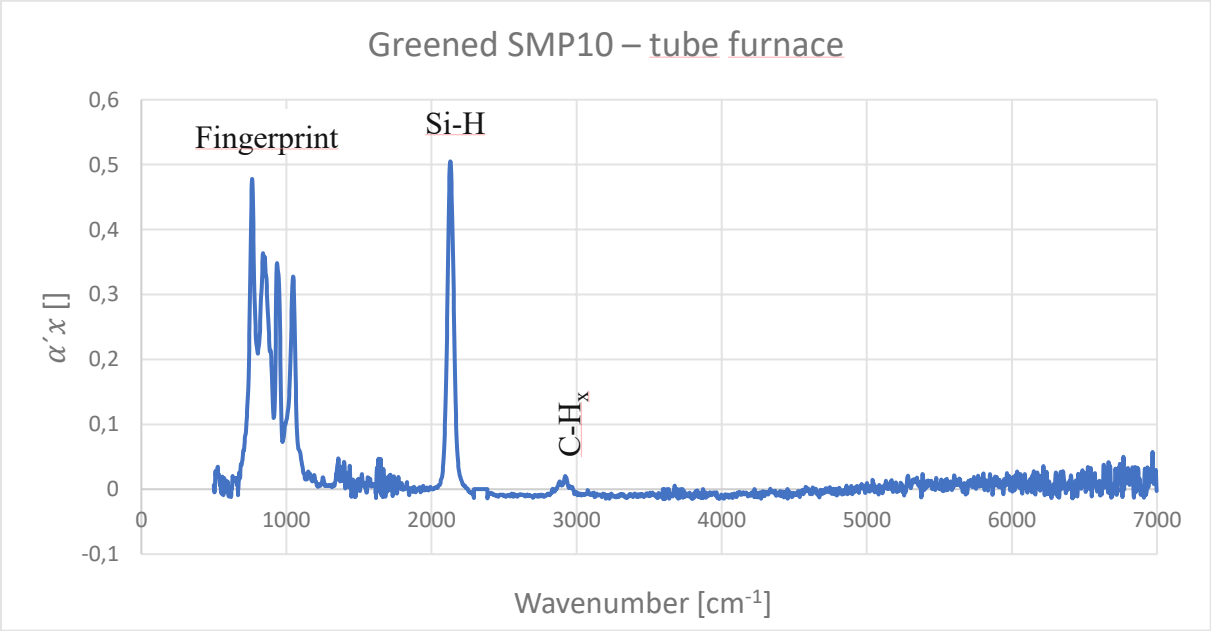

Figure 35: FTIR spectrum of finished thin film from the tube furnace.

In Figure 35 the fingerprint, Si-H and C-H_x peaks found in the liquid SMP10 film still exist, while the CO_x stretch peaks are not as clear as before. This was to be expected because only the vinyl bonds are consumed during greening.

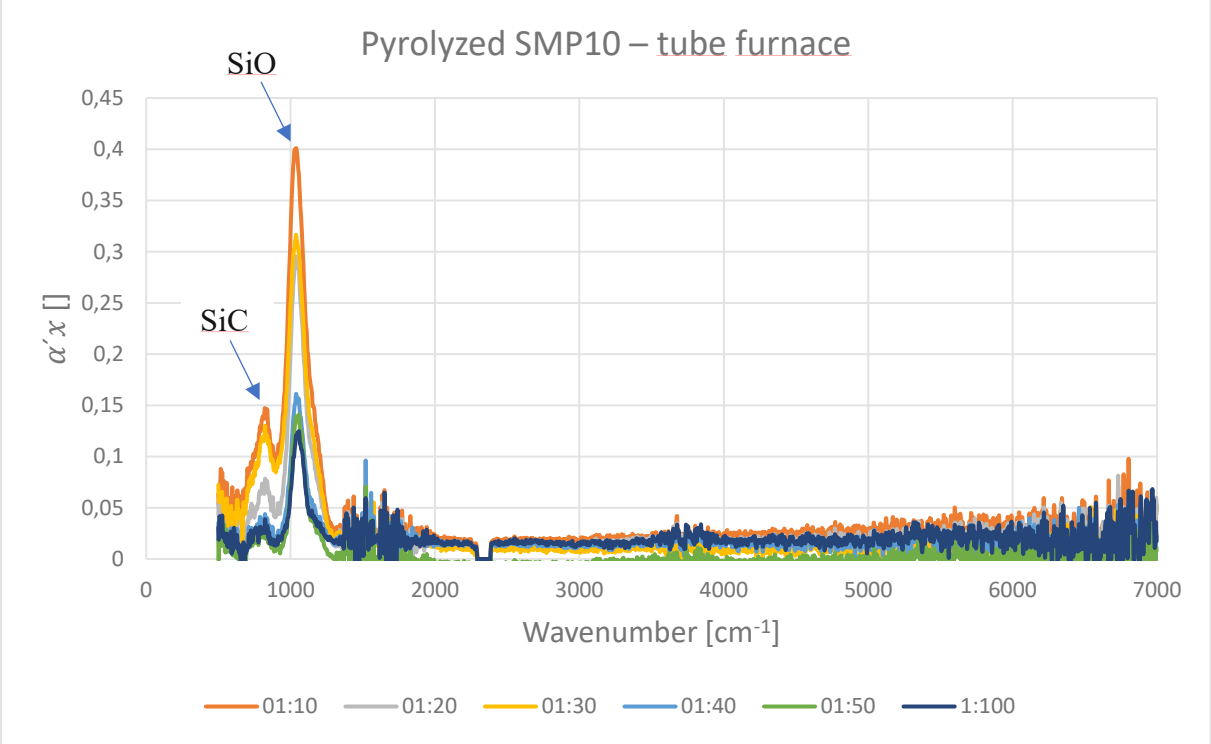

Figure 36: FTIR spectrum of finished thin film from the tube furnace.

Figure 36 shows, that the concentration has an influence on the intensity of the signal but not on the chemical fingerprint. While the found SiC peak [46] in Figure 36 was expected to be stronger, the detected SiO peak [47] was not expected. The SiO peak was found to occur most likely due to oxygen being present during pyrolysis. After several trials, the furnace was changed with the supposition, that the tube furnace had a leakage and oxygen seeps in while pyrolysis.

The analysis of the samples processed in the LPCVD oven are shown in Figure 37.

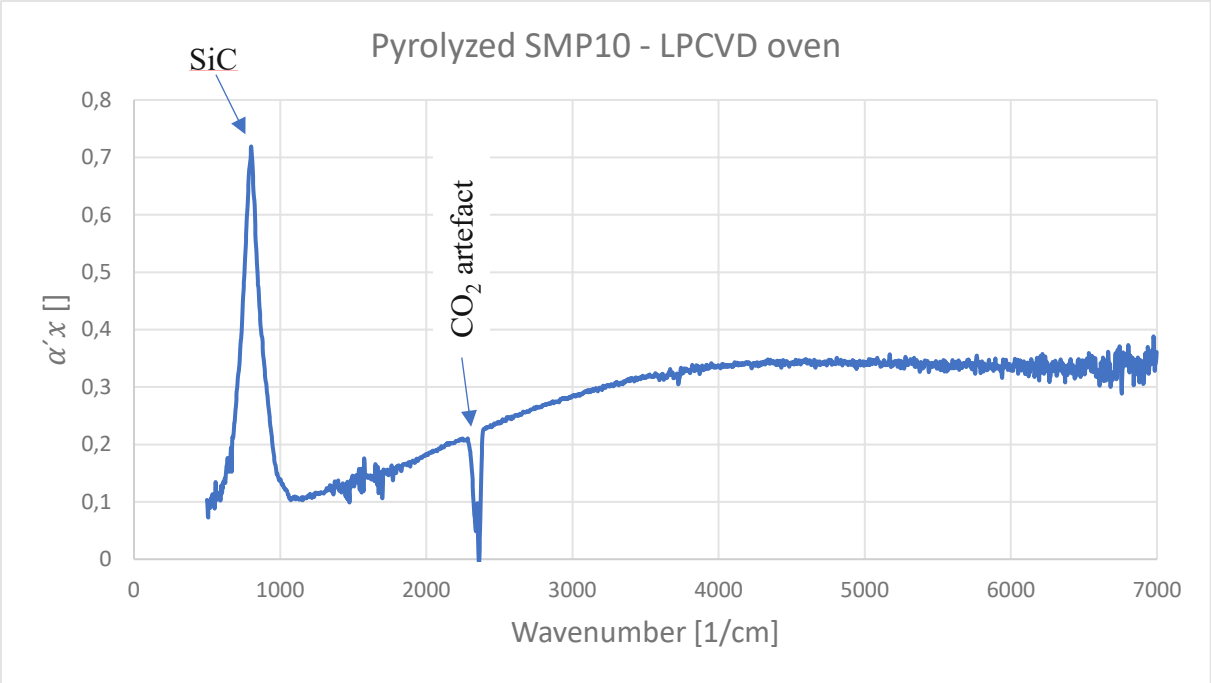

Figure 37: FTIR spectrum of finished thin film in LPCVD furnace without AIBN.

In Figure 37, only one spectrum is shown representative for all tested concentrations. The thin film consists mostly of SiC [46] as it would have been expected before. The negative peak at wavenumber 2360 cm^{-1} is the CO_2 artefact of the subtracted Si spectrum. Figure 37 shows the result of the coating solution mixed with AIBN. AIBN is expected to act as N dopant for SiC, forming SiN while pyrolysis. The FTIR spectrum in Figure 37 is representative for all tested concentrations of the coating solution.

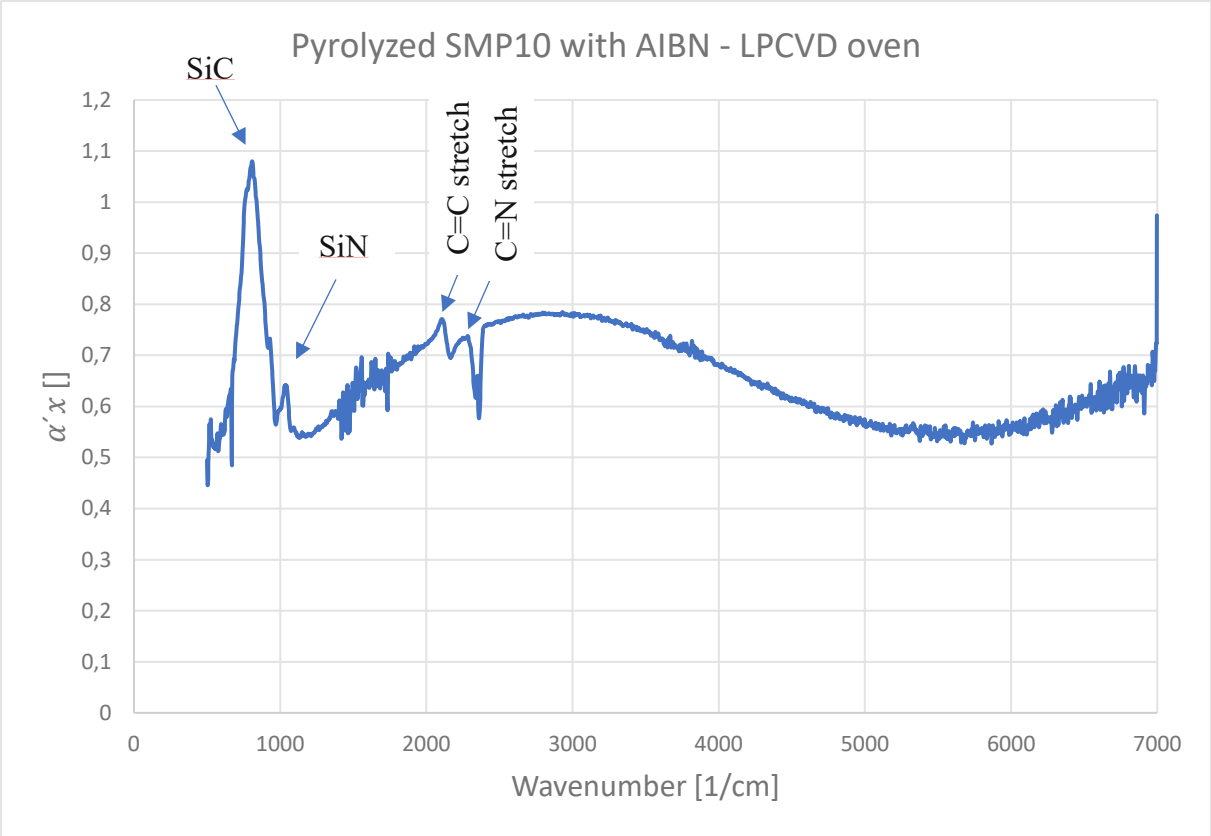

Figure 38: FTIR spectrum of finished thin film in LPCVD furnace with AIBN.

The expected SiC peak and the SiN [47] signal were found in the sample. Also, different concentrations of AIBN in the coating solution, either through lower or higher dilution, or less or more AIBN, result in weaker or stronger SiN peaks in the SiC thin film. Again, the CO_2 artefact occurred, but is assumed to be overlayed with the C=N stretch (2250 cm^{-1}).

The different FTIR spectra where the same for n-Si, p-Si and undoped Si. Also, no influence of different cleaning and surface modification processes was observed (see next section for details).

4.1.2. Surface Modification

For a better wetting of the silicon surface with SMP10, the surface energy of the silicon substrate should be as high as possible. TEVS causes initially a less good wettability, but in the end allows a better adhesion to the substrates because of the true chemical bonds between the thin film and the substrate (see 3.3 for details). Therefore, different approaches in cleaning of the surface and the modification with TEVS were done. Figures 39 and 40 are showing the

contact angle measurements of diiodomethane and water droplets on the activated surfaces of the Si substrate, respectively.

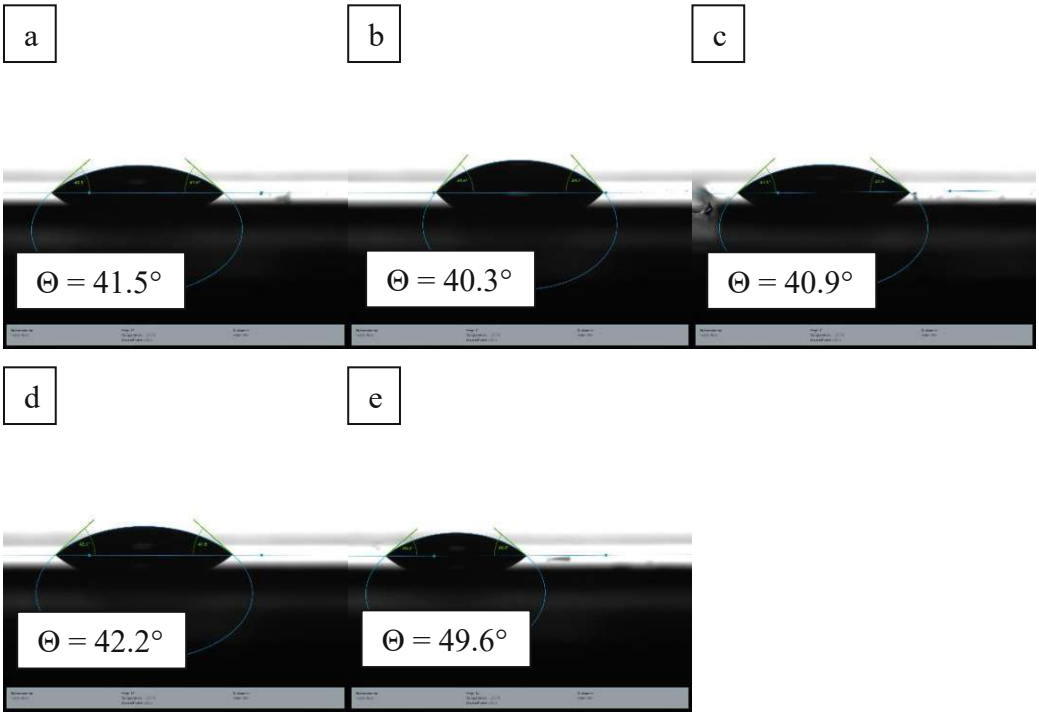

Figure 39: Contact angle measurements of diiodomethane droplets on Si surfaces, not modified (a), RCA and TEVS 30 min (b), RCA and TEVS 60 min (c), RCA and TEVS 120 min (d) and RCA and TEVS 5 h (e).

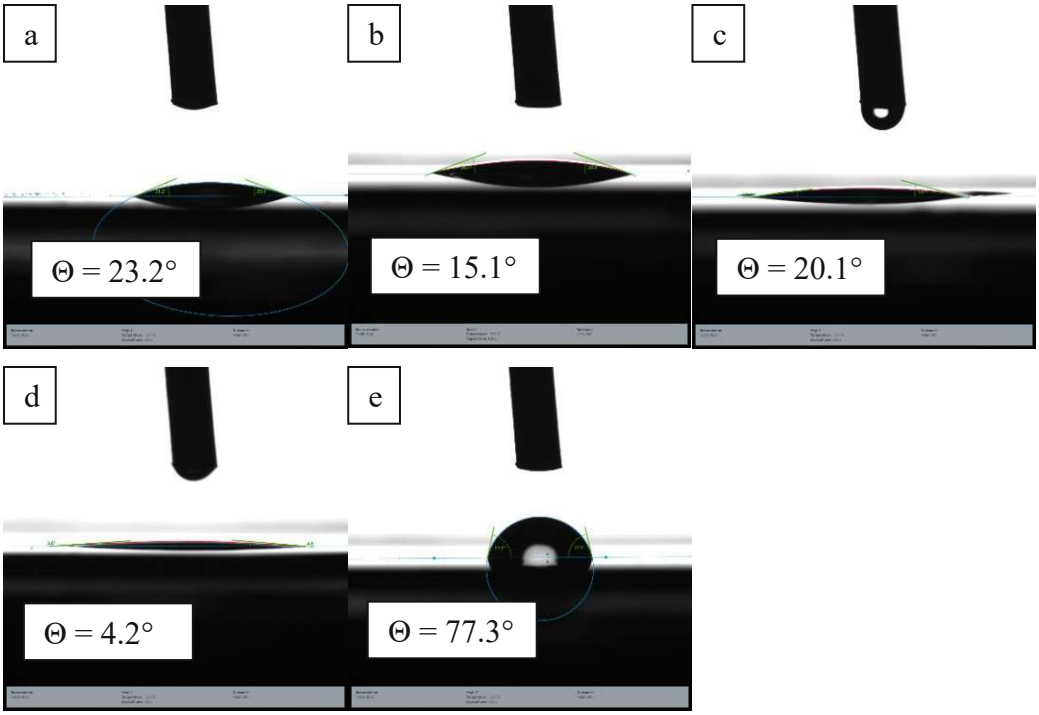

Figure 40: Contact angle measurements of H_2O droplets on Si surfaces: not modified (a), RCA and TEVS 30 min (b), RCA and TEVS 60 min (c), RCA and TEVS 120 min (d) and RCA and TEVS 5 h (e).

Figures 39 and 40 show the contact angle measurement of differently modified surfaces of diiodomethane and water droplets from one experiment, where the surfaces were not modified (a), RCA cleaned and in TEVS for 30 min immersed (b), RCA cleaned and in TEVS for 60 min immersed (c), RCA cleaned and in TEVS for 120 min immersed (d) and, RCA cleaned and in TEVS for 5 hours immersed (e).

The with equation 11 -14 calculated surface energy is shown in Figure 41.

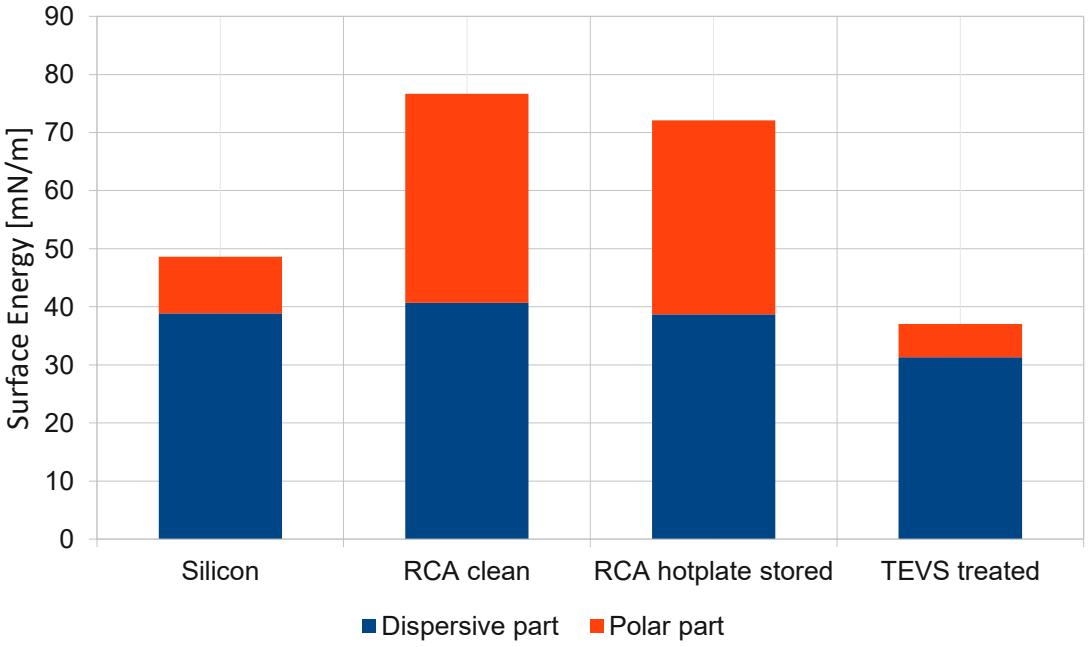

Figure 41: Surface energy of different surface modification; TEVS treated for 5 h.

Figure 41 shows the comparison of surface energy of untreated silicon samples, RCA cleaned silicon samples, RCA cleaned, and hotplate stored silicon samples and with TEVS treated (5 hours) silicon samples, divided in polar and dispersive part. The RCA process increases the surface energy, especially the polar part, while the surface modification with TEVS lowers the overall surface energy. If the sample is stored on a hotplate at 80 °C after treatment, the surface energy decreases [26]. This effect can slightly be seen in Figure 42. One mainly sees the EtOH does not work, and that time is needed to saturate the surface with TEVS.

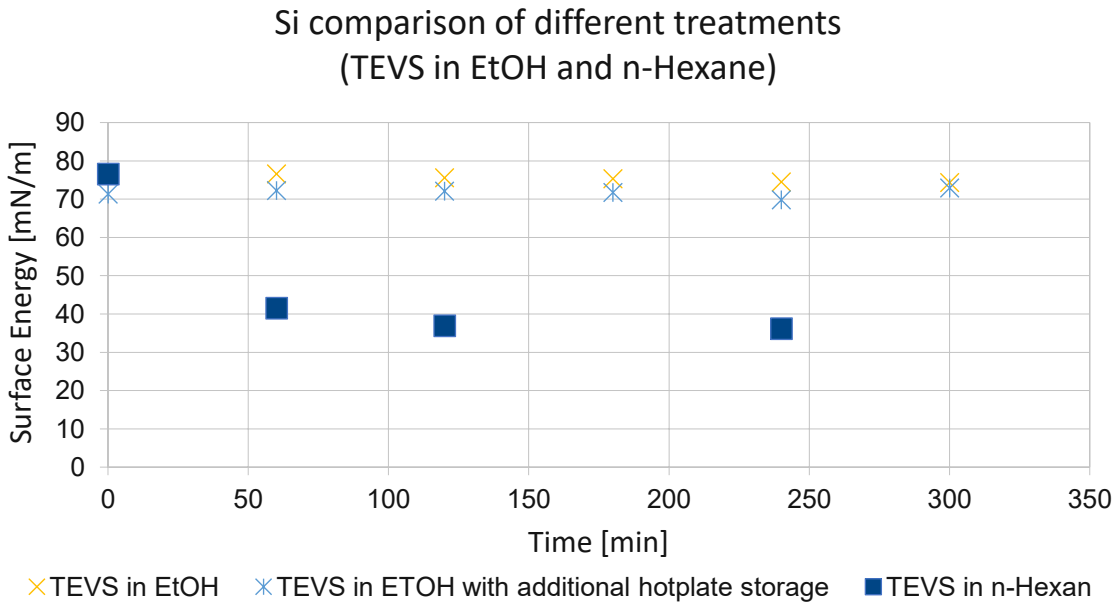

Figure 42: Comparison of the influence on surface energy depending on the treatment time with TEVS.

In Figure 42 the effect of the additional hotplate storage is marginal, while the influence of the solvent for TEVS as a big impact on the surface energy. The bad performance of TEVS in EtOH can be explained with the competitive behavior of EtOH, which wants to occupy -OH groups at the surface of the Si wafer (see also Figure 10 b).

4.1.3. Layer thickness measurement

The layer thickness was measured with the reflectometric thin film measurement method. Therefore, equation 16 – 20 were implemented in a phyton program (Appendix 7.3) to calculate the film thickness. The typical measurement results with the envelope E_M and E_m and the minima and maxima are shown in Figure 43 for liquid (a), greened (b) and pyrolyzed (c) films.

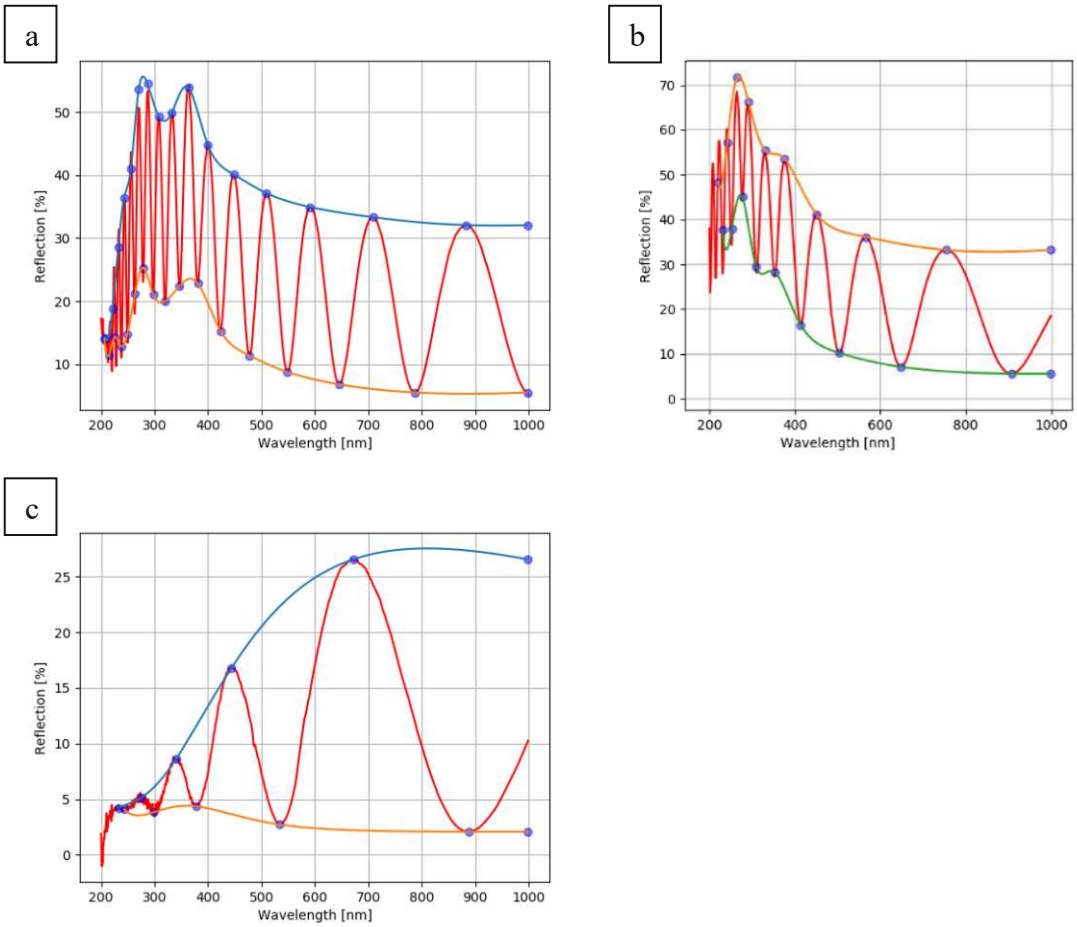

Figure 43: Measurement result of the reflectometric thin film measurement method with the Filmetrics device and calculated envelops E_M and E_m and minima and maxim for liquid (a), greened (b) and pyrolyzed (c) thin film.

With this method, the film thickness of each sample was calculated. The found refraction indices are listed in Table 3, which are in accordance to the literature values of the liquid and greened SMP10 films [48].

Table 3: Calculated refraction indices from reflectometric measurements (median values of the visible spectrum).

n_{liquid}	1.46
n_{green}	1.48
$n_{UV\_greened}$	1.49
$n_{pyrrolyzed}$	2.02

In Table 3 the different refraction indices for liquid, greened and pyrolyzed SMP10 films are shown. Between the greened sample without AIBN and the greened sample with AIBN the

refractive index shows no big difference, which indicates, that AIBN does not strongly influence the optical properties of SMP10. The in the tube furnace pyrolyzed thin film has a refraction index between SiO (typical 1,9) and SiC (typical 2,6) which was expected and is in accordance with the FTIR result in Figure 36.

The film thickness of liquid SMP10 on RCA cleaned and TEVS modified samples are shown in Figure 44, the results for the greened samples are shown in Figure 45 and Figure 46 shows the summary of the pyrolyzed film thicknesses for different spin coating parameters and surface modifications. All samples consist of 9 measurement each, divided into 3 prepared sample with each 3 measurements of the thin film.

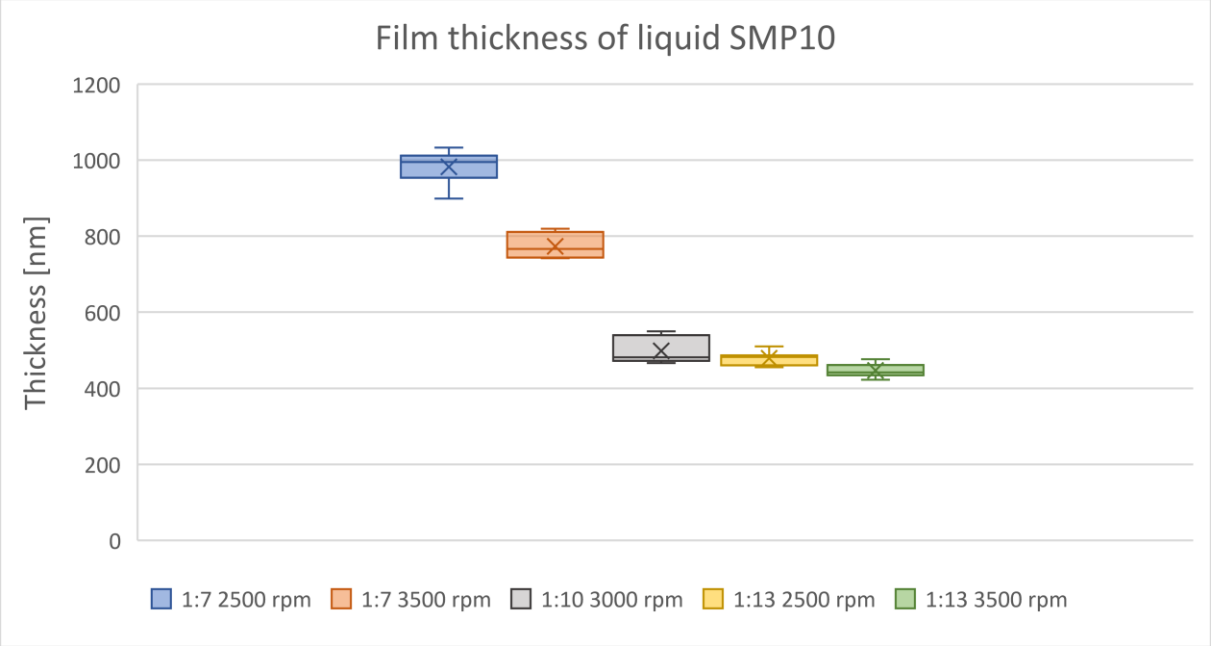

Figure 44: Film thickness of liquid SMP10 on RCA cleaned and TEVS modified surface.

In the diagram in Figure 44, 45 and 46, the line in the box indicates the median, the x the average value and the ⊤ and ⊥ are the minimum and maximum values, caused by measurements on the edge of the sample which are thicker due to the used spin coating process.

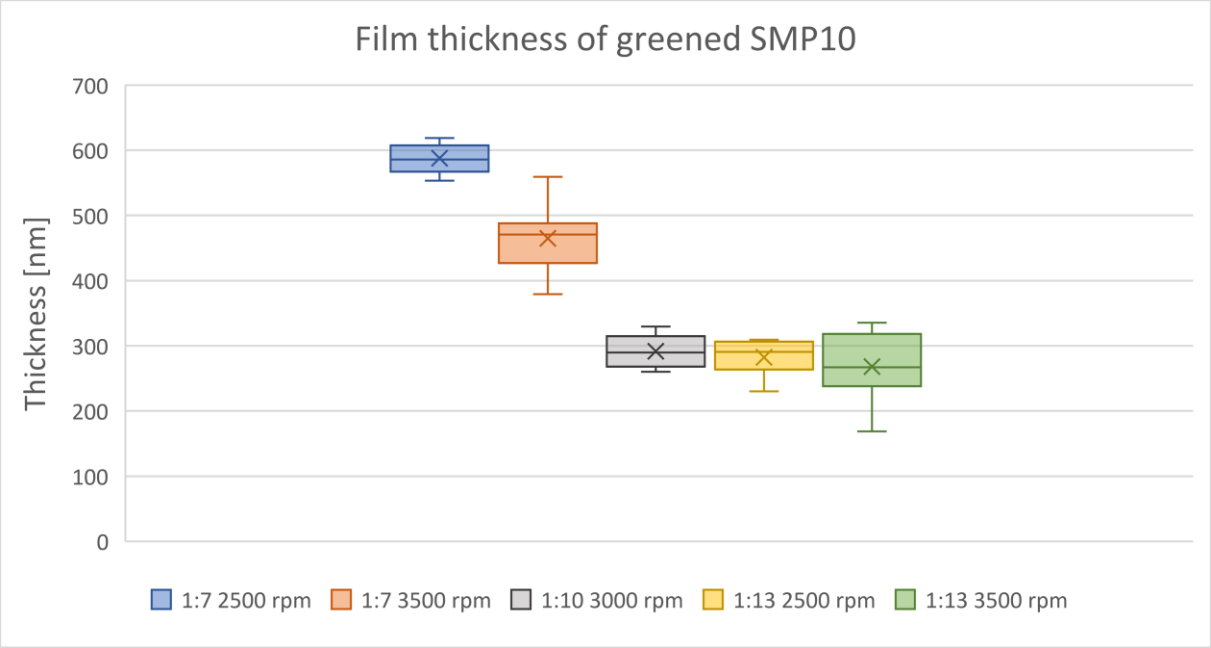

Figure 45: Film thickness of greened SMP10 on RCA cleaned and TEVS modified surface.

The shrinkage from the liquid to the greened film and from the greened to the pyrolyzed film was for both cases around 40 %.

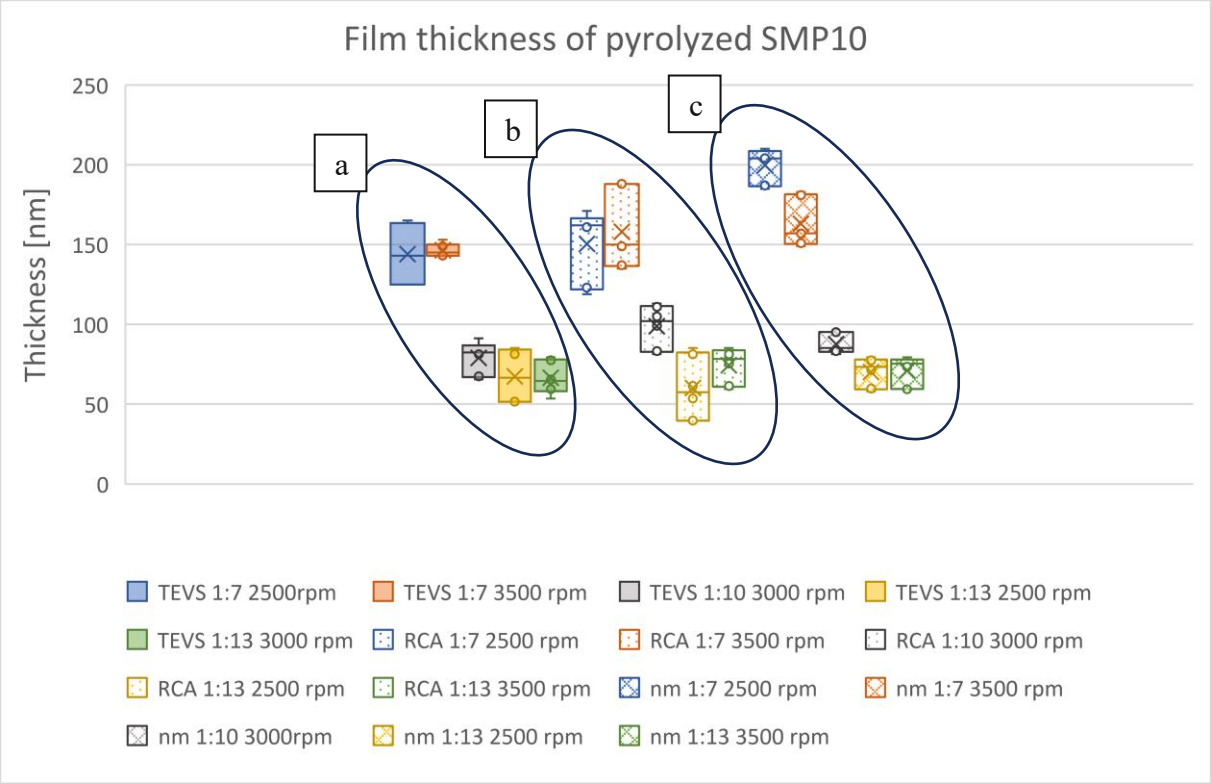

Figure 46: Film thickness of pyrolyzed SMP10 films with RCA cleaned and TEVS modified surface (a), RCA cleaned surface (b), and no modification of the surface (c).

While the film thickness in Figure 44 and Figure 45 were measured with the reflectometric measurement method, the film thickness in Figure 46 was measured with the SEM because the film was too thin for representative reflectometric measurements. Figure 45 also shows the influence of the surface modification on spin coating. All samples have been prepared with the same set of parameters, shown in Table 4. Figure 46 (a) shows the group of RCA cleaned and TEVS modified surface, Figure 46 (b) the group of only RCA cleaned Si substrate and Figure 46 (c) the group without modified surface. It can be seen that the thickest film is on the not cleaned or modified surfaces, while the thinnest film is found on the RCA cleaned and with TEVS modified surfaces, especially with the lower diluted SMP10 solutions. This may be because the samples cleaned with RCA and treated with TEVS have the lowest surface energy, as found in 4.1.2.

Table 4: Parameters for spin coating experiments with different surfaces.

Dilution [SMP10:Solvent]	1:7	1:7	1:10	1:13	1:13
Rotation [rpm]	2500	3500	3000	2500	3500

The DoE analysis with the contour and Pareto plot of the presented data are shown in Figure 47 and Figure 48, respectively. The data used for calculation are shown in Table 5.

Table 5: Used data for the contour and Pareto plot.

Real Variables		**Coded Variables**		**Median Thickness [nm]**		
Speed [rpm]	Dilution []	Speed	Dilution	Liquid	Green	Pyrolized
2500	1 to 7	-1	-1	994.5	585.5	143
3500	1 to 7	1	-1	785.3	470.7	145
3000	1 to 10	0	0	474.4	289.6	82.3
2500	1 to 13	-1	1	476.8	298.5	83.3
3500	1 to 13	1	1	440.7	267.2	64.5
Fit Function	Y = A · Speed + B · Dilution + C · Speed + D					
Analysis						
	Pyrolized	Green	Liquid			
A	-4.2	-36.5	-61.3			
B	-35.1	-122.6	-215.6			
C	-5.2	20.9	43.2			
D	103.6	382.3	634.3			

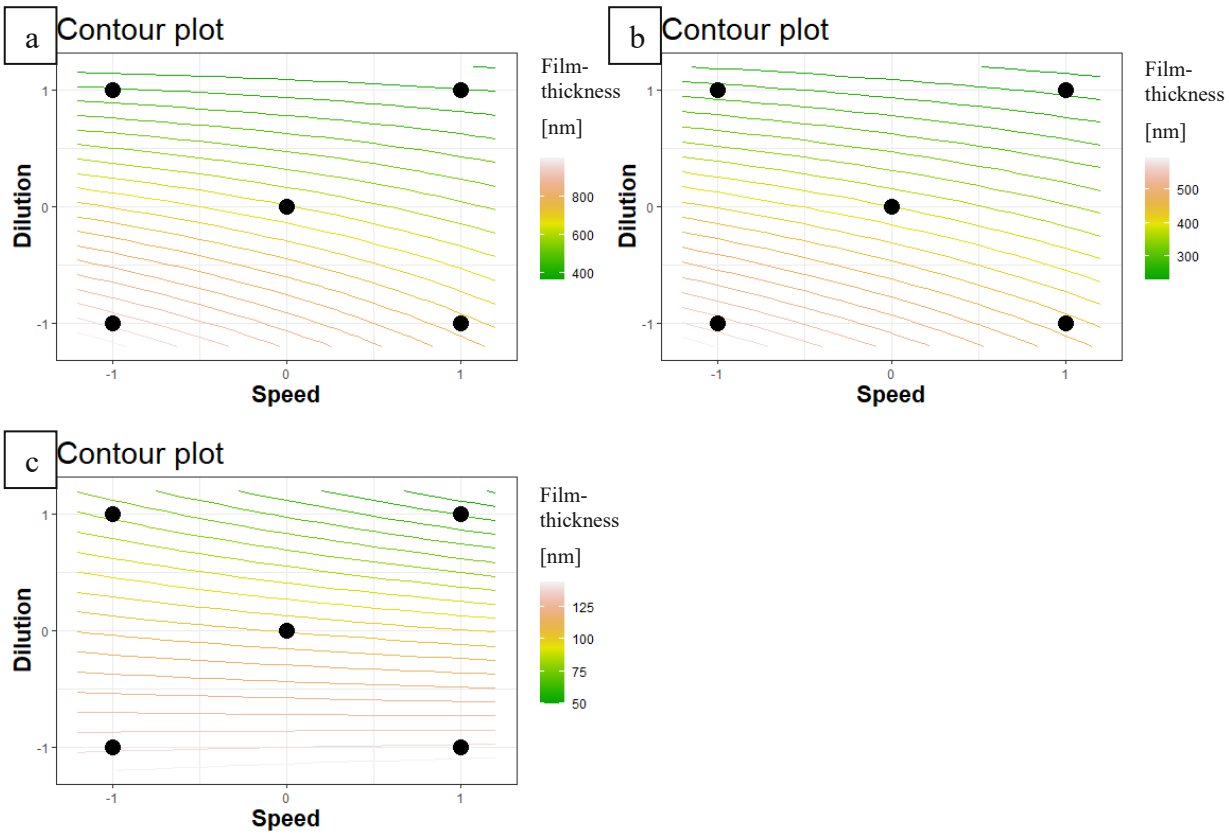

Figure 47: Contour plot for the liquid film (a), greened film (b) and pyrolyzed film (c), using the data from Table 5.

In Figure 47 both parameters, dilution of SMP10 and rotation speed of the spin coater influence the film thickness, indicated through the contour lines. Higher speed and dilution cause a lower film thickness according to the contour plots in Figure 47.

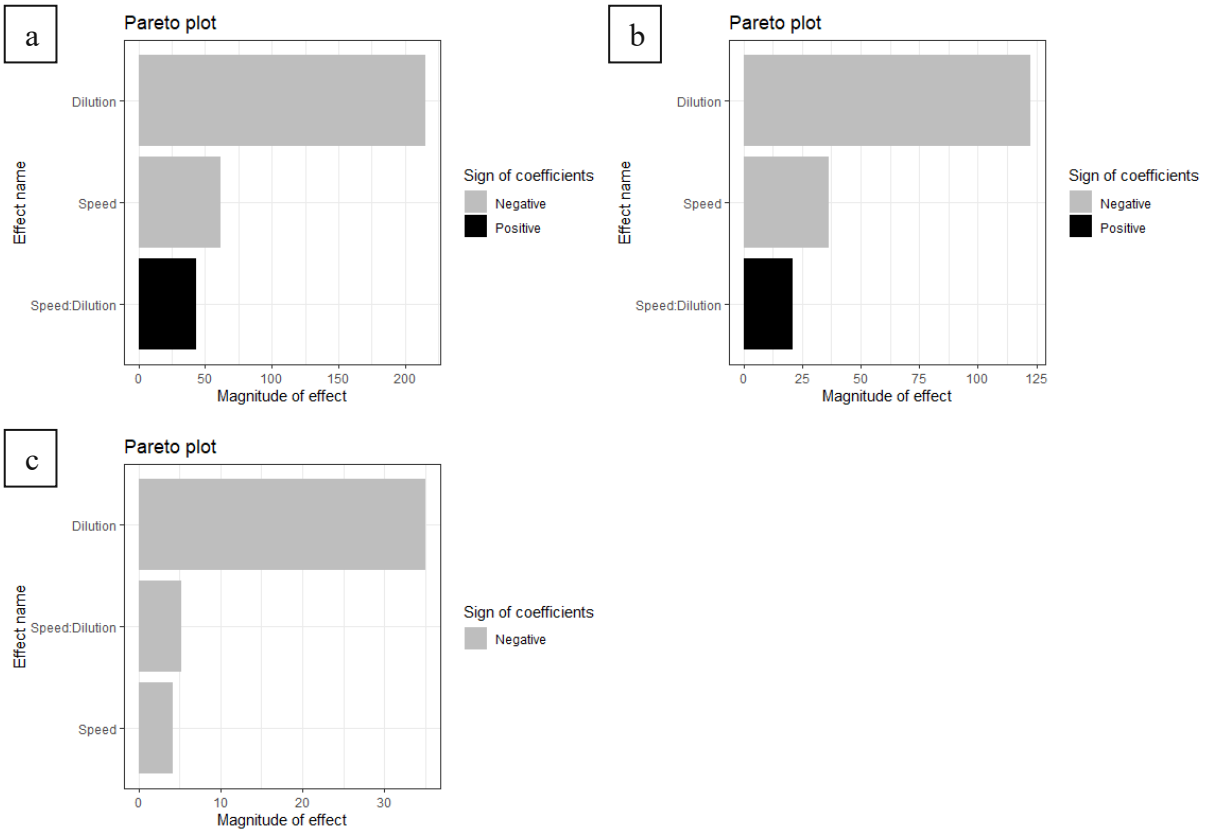

Figure 48: Pareto plot for the liquid film (a), greened film (b) and pyrolyzed film (c), using the data from Table 5.

Figure 48 shows the individual influence of the parameters of the film thickness. The pareto plots visualize the magnitude of the effect according to the fit functions in Table 5. In all three cases, the dilution affects the film thickness the most.

4.1.4. Scanning electron microscope analysis

To gain insight into the (crystalline) microstructure of the thin film and the film thickness, the samples with the thin films were cleaved and the cross section was analysed with the SEM.

Figure 49 shows the cross section of a dense, coherent SiC film which was fabricate with a 1:10 dilution of SMP10 with m-xylene, 3500 rpm spin coating velocity and RCA cleaned Si substrate.

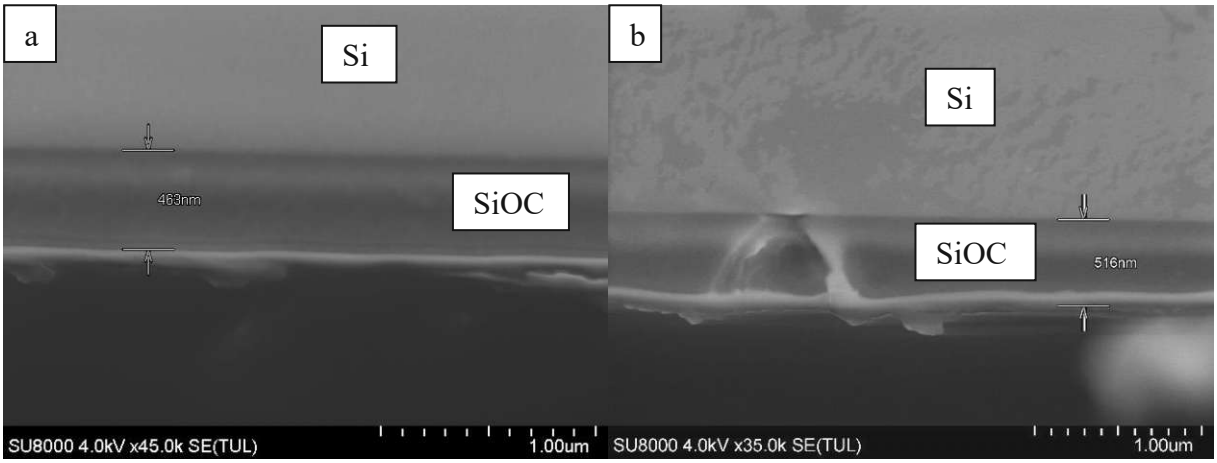

Figure 49: Amorphous, but dense thin film (a) defects in thin film (b) both samples with a 1:10 SMP10 solution, 3500 rpm spin coating speed, RCA cleaned, processed in tube furnace 1000 °C.

Crystaline SiO_2 is formed above 1200 °C [49], which indicates, that the thin film in Figure 49 is amorphous, since the samples in the tube furnace where pyrolyzed at 1000 °C. The high film thickness of 490 nm besides the recorded FTIR spectra is an additional indicator for oxidation because the reflectometric measurements of the film thickness showed, that the film thickness of mostly SiC films should be between 80 nm and 120 nm with the used parameters. In Figure 49 (b) a defect can be seen, which corresponds to a pinhole on the surface. The samples were processed in the tube furnace with 400 °C for curing and 1000 °C for pyrolysis.

Figure 50 (a) shows a polycrystalline SiC film, with AIBN admixed to the SMP10 coating solution, which was desired. Figure 50 (b) shows under-etching of the Si, most likely caused by H_2 [50]. Both samples were processed in the LPCVD at 1200 °C.

The thin films in Figures 49 and 50 appear fundamentally different in the SEM, which is expected because the FTIR showed that two different materials, SiC and SiOC, were synthesized.

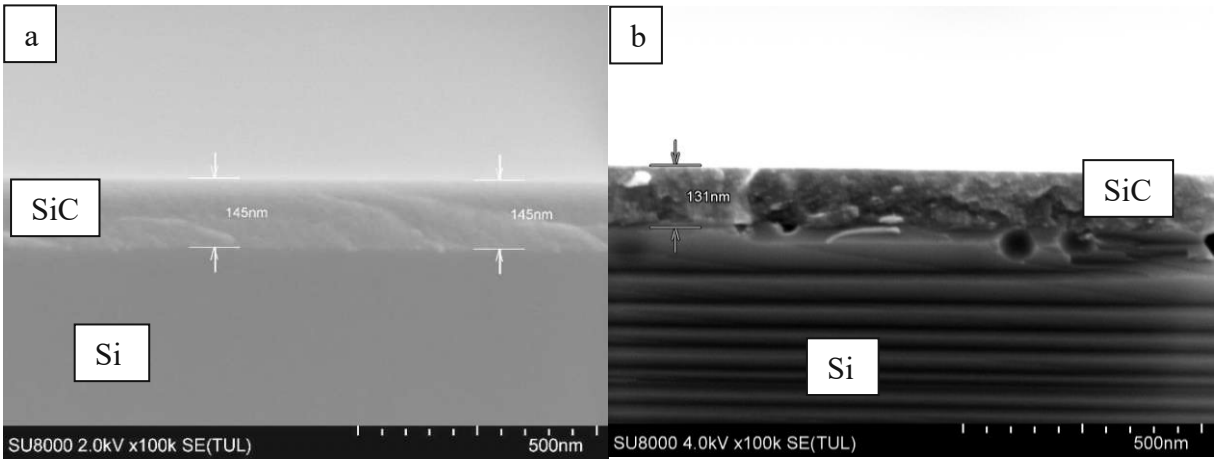

Figure 50: Cross-sectional view of polycrystalline SiC layer with AIBN admixed to the SMP10 solution after 1200 °C in Argon (a) and under etching of Si after 1200 °C in Argon, SiC layer without AIBN in the SMP10 solution (b).

4.1.5. Optical microscope

The quality of the surface could be evaluated with an optical microscope. Figure 51 shows the influence of the spin coating speed on the surface. While in Figure 51 (a) many defects in form of pinholes are visible, the defects drastically decreased with less rotations per minute, shown in Figure 51 (b). The used dilution of SMP10 was 1:10 with n-hexane as solvent. The sample was processed in the tube furnace.

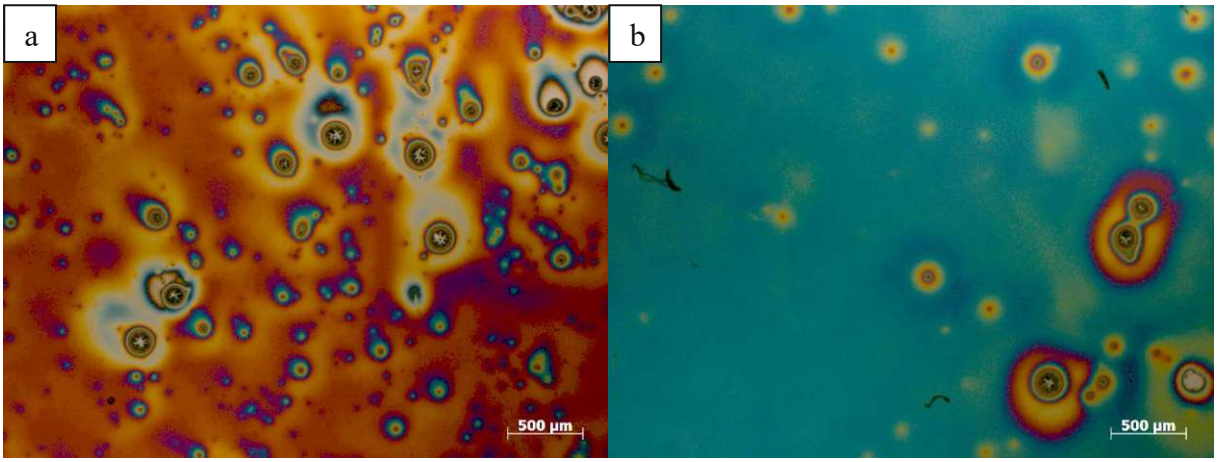

Figure 51: Surface analysis of pyrolyzed samples with 1:10 SMP10 dilution solution and 3000 rpm spin coating speed with many defects (a) and sample with 1:10 diluted SMP10 and 2000 rpm spin coating speed (b).

Figure 52 (a) shows the cracking of the surface after pyrolysis, most likely due to excess shrinking of a sample with a 1:7 SMP10 dilution with n-hexane and 1500 rpm spin coating

speed. Figure 52 (b) shows a greened sample which was prepared with the same parameters, where the pinholes are already present as well.

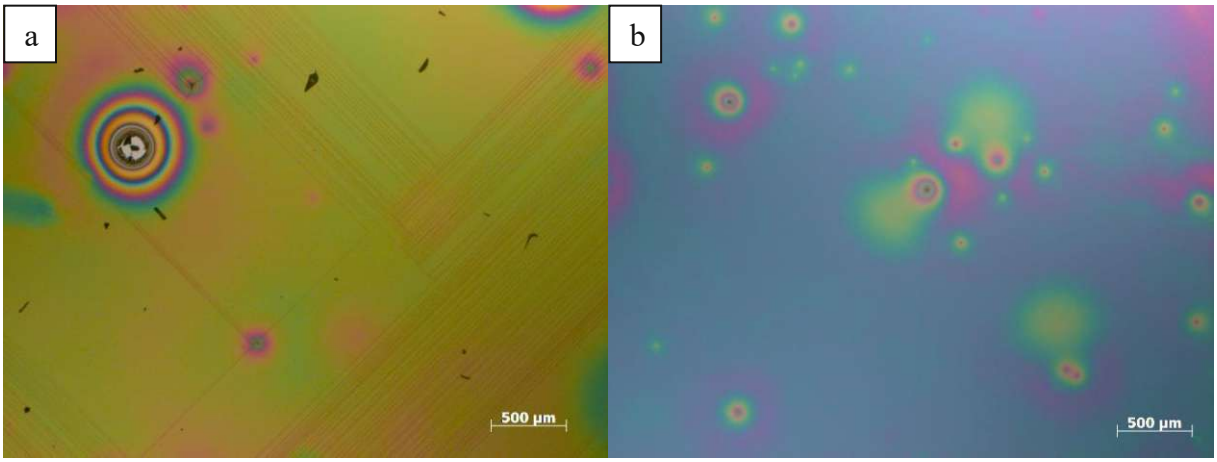

Figure 52: Presence of surface cracks after pyrolysis, 1:7 SMP10 dilution with n-hexane and 1500 rpm spin coating speed (a) greened film with already present pinholes (b).

In Figure 53, the results of mixing the coating solution with Durazane are shown. The 1:10 SMP10 dilution with n-hexane was spin coated with 3000 rpm and processed in the tube furnace. While in liquid state, a coherent, dense film formed, excessive dewetting occurred while pyrolysis as can be seen in Figure 53 (a) and (b). The Si sample was cleaned, using ultrasound, Piranha acid and a hydrofluoric (HF) acid dip.

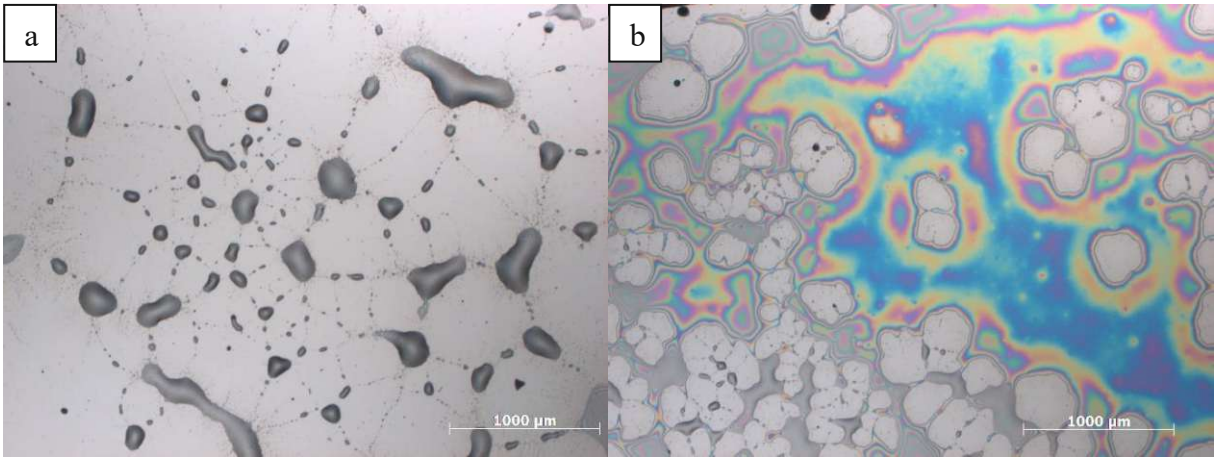

Figure 53: Excessive dewetting with Duranzane mixed to SMP10 after pyrolysis, no film formation at all (a) and slightly film formation (b).

Figure 54 shows the results with m-xylene instead of n-hexane as solvent for SMP10. Both samples were RCA cleaned and had a dilution of 1:10 of SMP10 with m-xylene. The SMP10 and m-xylene were filtered with a 2µm filter. While the sample in Figure 54 (a) was coated

with a spinning speed of 1500 rpm, the sample in Figure 54 (b) was coated with a speed of 3000 rpm.

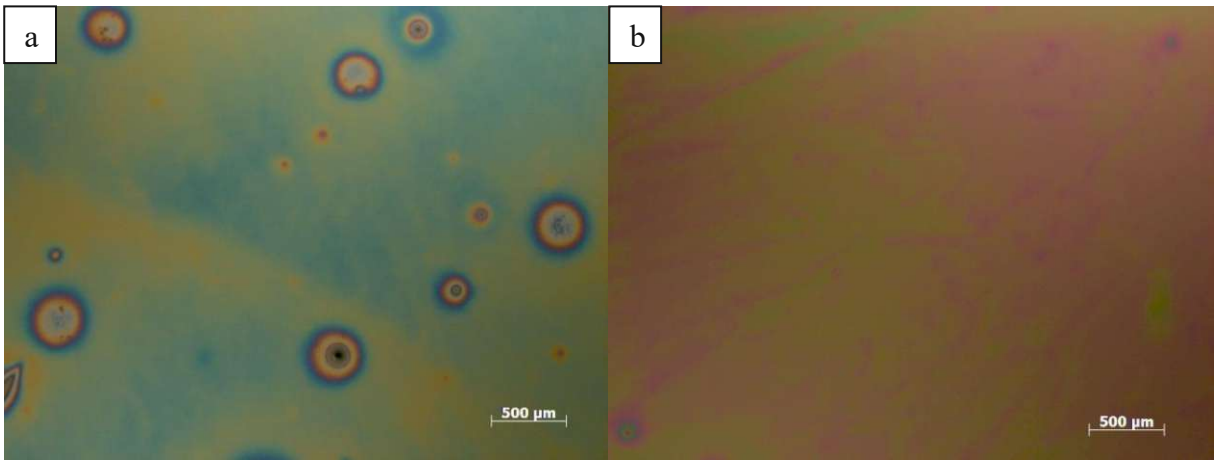

Figure 54: Effect of spin speed on surface defects: 1500 rpm spin coating speed (a) and 3000 rpm spin coating speed (b). Both samples were RCA cleaned, with a 1:10 dilution of SMP10 with m-xylene and all reagents were filtered with a 2 µm filter syringe.

In Figure 55 the results of UV spin coating are shown, which was done to fill up or close the pinholes with a second layer of SMP10 [30].

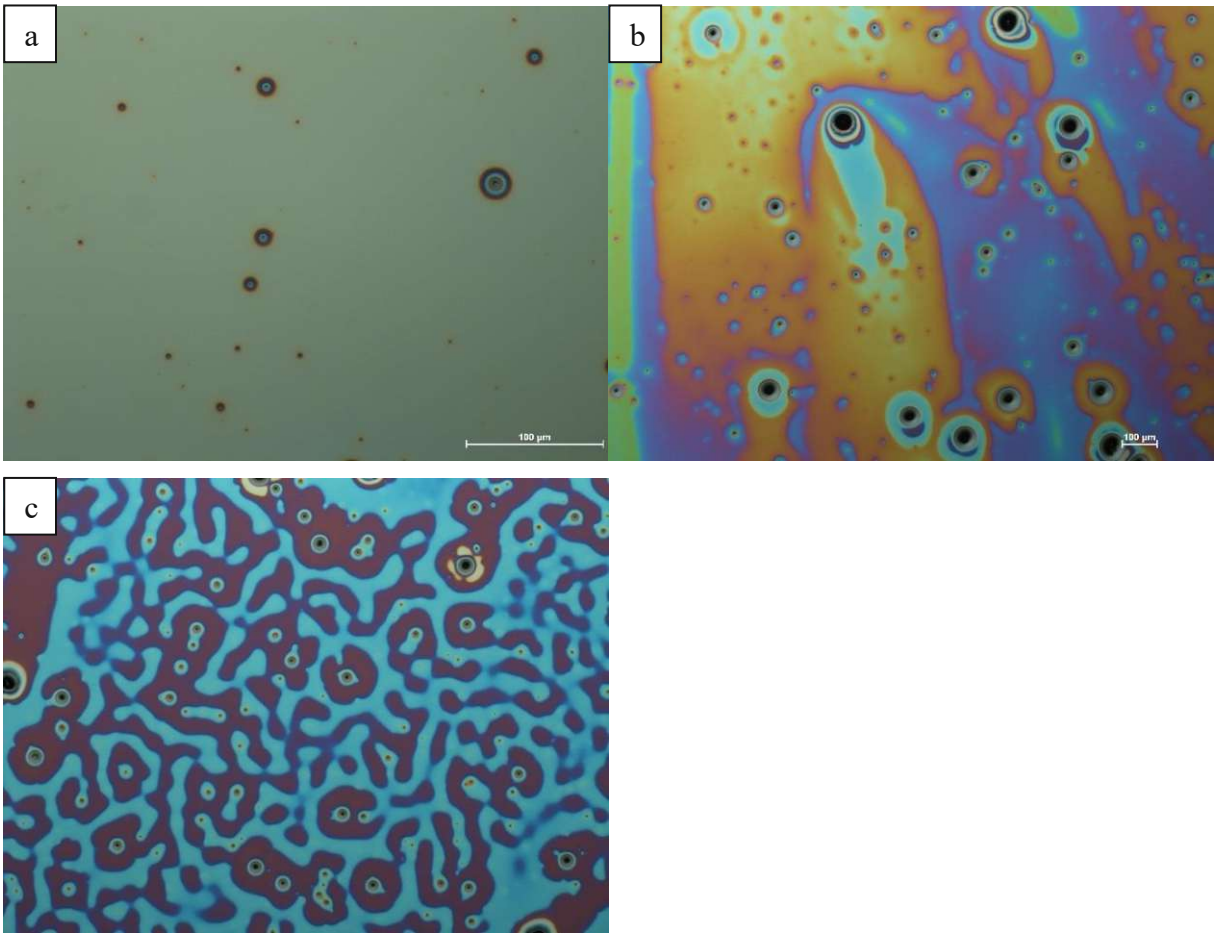

Figure 55: Multicoating: first coating after pyrolysis (a) second coating after pyrolysis (b) and UV spin coating 2 layers (c); each layer coated with a 1:13 solution with AIBN, 3500 rpm, RCA cleaned and with TEVS modified surface.

In Figure 55 (a) the first film is shown after pyrolysis using a dilution of 1:13 of SMP10 with m-xylene. In Figure 55 (b) the second layer of the same sample is shown with again, a dilution of 1:13 of SMP10 with m-xylene. In Figure 55 (c) a sample with the first layer cured under UV-C light and the second layer applied directly after curing can be seen after pyrolysis in the LPCVD furnace. The analysis with the optical microscope showed, that m-xylene works better as solvent as n-hexane. This could be caused by the lower vapor pressure of m-xylene.

The assessment of the thin films under the microscope was the decision-making base for the trend of the DoE trials. To synthesize an adhesive, dense and coherent thin film, several DoE´s have been conducted. The first DoE was to find the parameters for an adhesive thin film without flake offs, dewetting or cracking. If a thin film showed cracking, dewetting or flake of, the experiment was considered a failure, but if all experiments of the trial failed, the trend was determined by the least cracking, dewetting or flake of. After the parameters for an adhesive, coherent thin film had been found, the focus was shifted to the pinholes, starting a new DoE.

The thin film with least defects determined the trend of a trial. With the parameters found for the least pinholes, a new DoE was started for the film thickness, as discussed in section 4.1.3.

The cracking could be adjusted with the DoE but for the pinholes, which may be caused through particles, it may not be the only tool for a solution. Here a chemical/physical solution is needed to get completely rid of the problem. An overview over the conducted experiments and the results of the conducted trials in the DoE´s can be found in Appendix 7.2.

4.1.6. Electrical Film Resistance

The electrical resistance was measured with the four-point method [51], [52]. While there was an infinitely large resistance for the samples with SMP10 without additives, the resistance dropped significantly for samples with AIBN admixed to the SMP10 coating solution.

While the measured bulk material had a resistance of 700 kΩ, the sample with a thin film from a 1:7 diluted SMP10 spin solution had a resistance of 6 kΩ and the sample with a thin film from a 1:13 diluted SMP10 spin solution had a resistance of 14 kΩ. The difference in the resistance between the two samples is most likely due to more defects in the thin film of the sample with 1:13 diluted SMP10. The specific resistance ρ of the thin film can be calculated with [53]

$$\rho = R \cdot \frac{A}{l} \qquad (21)$$

where ρ is the specific resistance, R is the measured resistance, A is the cross-sectional area, through which the current flows, consisting of the film thickness multiplied with the sample width, and l is the sample length distance between the contacts. With the measured resistance and the respectively film thickness, the results in Table 6 were obtained. D. Schroder [54] defines materials with a specific resistance from 10^{-3} to 10^{9} Ωcm as semiconducting.

Table 6: Specific resistance of the measured thin films.

Dilution / Film thickness (nm)	Specific resistance (Ωcm)	Comment
1:7 / 145	0,087	Semi-conductive
1:13 / 70	0,098	Semi-conductive

4.1.7. XRD

Since Si has a very strong reflection between 65 °θ and 74 °θ which would dominate all other signals by far, the XRD measurement was split in two measurements per sample to cut this peak off.

For analysis of the diffractogram, HighScore Plus [55] for compound determination was used. The results of the XRD analysis are shown in Figure 56 and 57. While Figure 56 and 57 (a) show the diffractogram from 5 °θ to 65 °θ, Figure 56 and 57 (b) show the diffractogram from 74 °θ to 120 °θ.

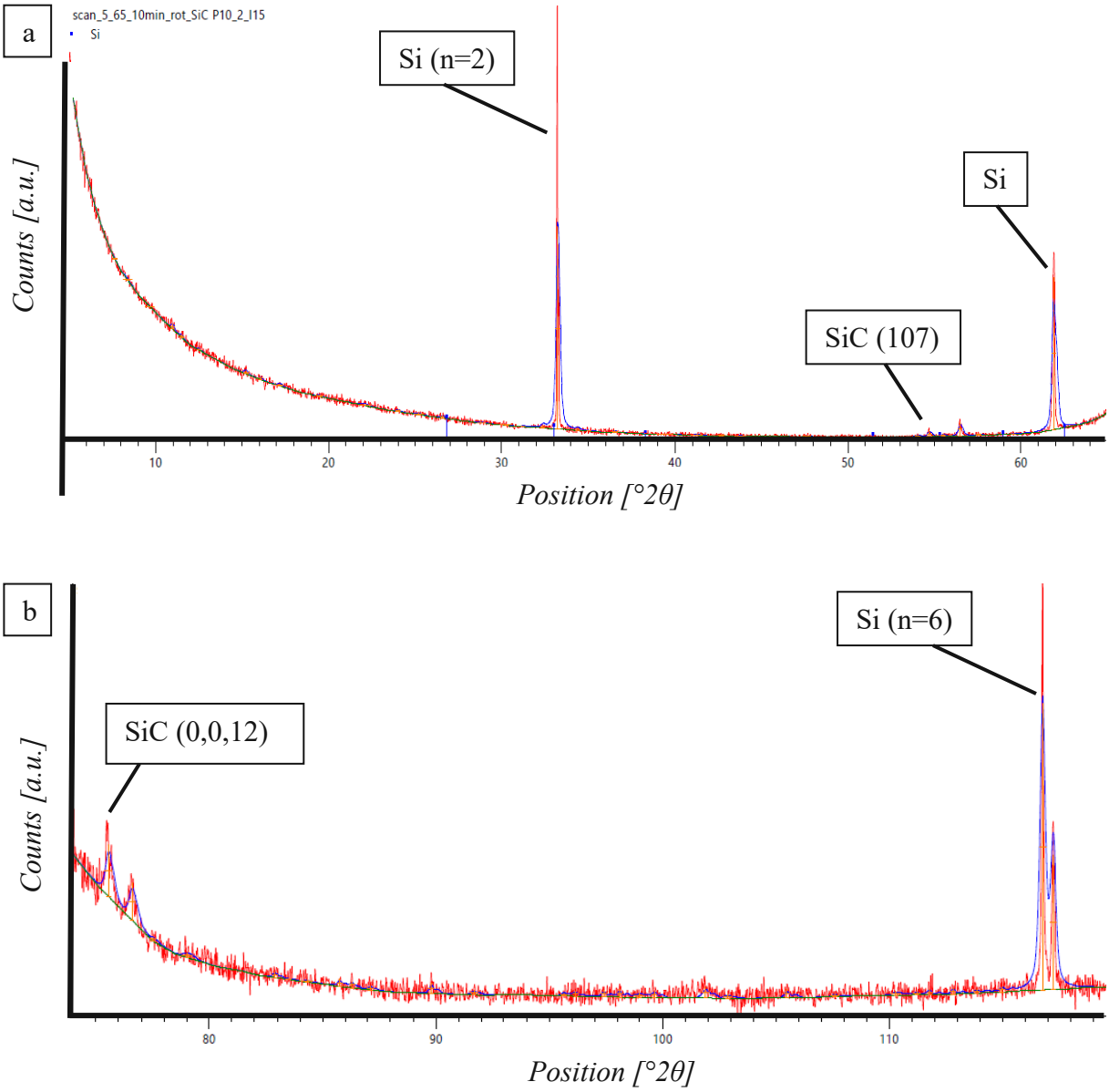

Figure 56: XRD of SiC thin film on Si sample, dilution: 1:7, 2500 rpm, RCA cleaned; 5 °2θ – 65 °2θ (a), 74 °2θ – 120 °2θ (b).

Figure 56 shows the diffractogram for the SiC thin film without AIBN, processed in the LPCVD furnace. In Figure 56 (a) crystalline SiC (107) and in Figure 56 (b) crystalline SiC (0,0,12) was found. The Si peaks and pattern occur due to not only pinholes but also due to reflection below the SiC thin film, since the used X-rays have a penetration depth of up to 30 µm through SiC, depending on the incidence angle [56].

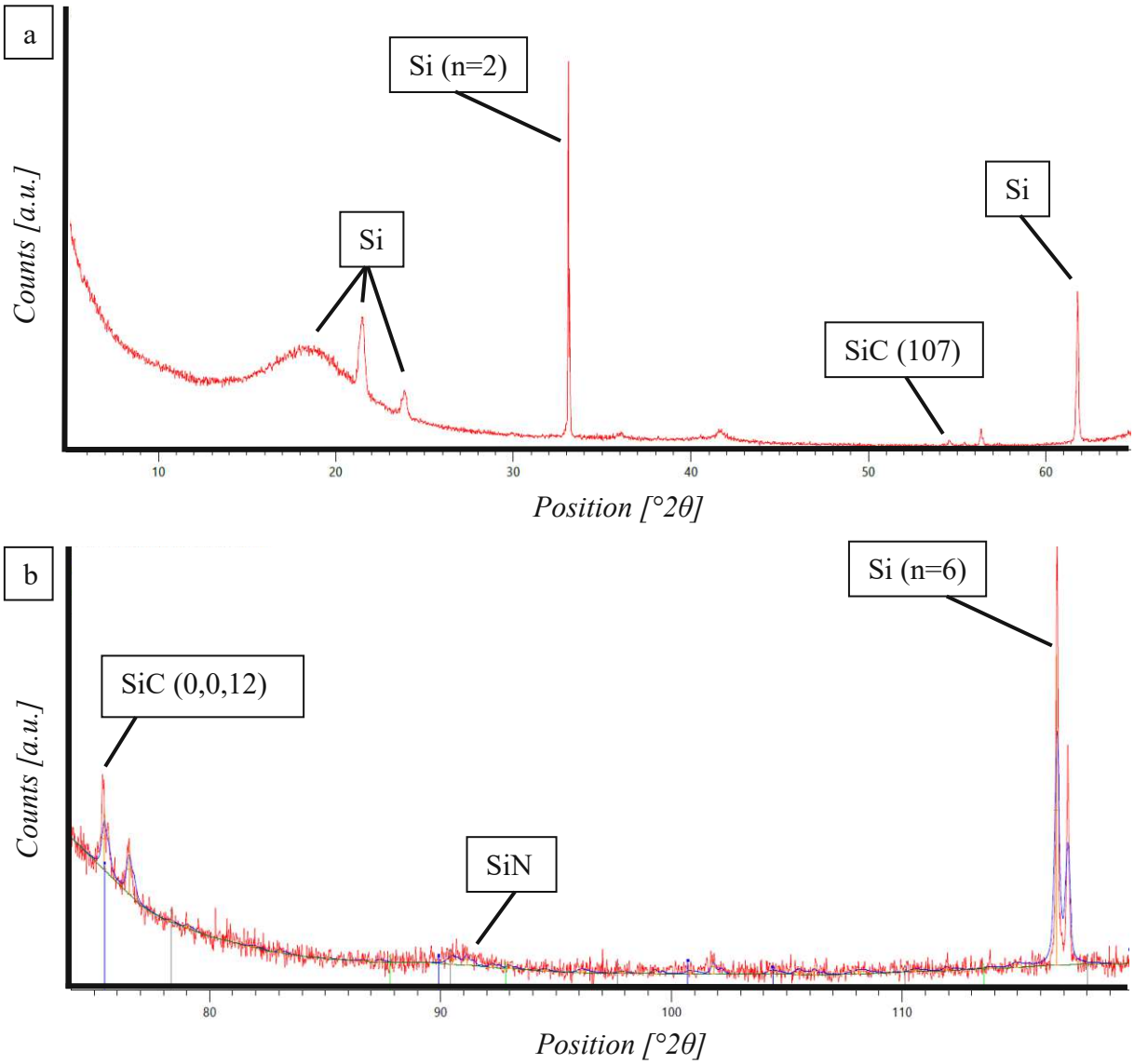

Figure 57: XRD of SiC thin film with AIBN admixed to the SMP10 solution, on Si sample, multicoated 1:13, 5500 rpm, RCA cleaned and TEVS modified; 5 °2θ – 65 °2θ (a), 74 °2θ – 120 °2θ (b).

In Figure 57 (a) and (b), the peak and pattern search of the HighScore Plus program found crystalline SiC and SiN (Si_3N_4) as a weak pattern of the sample with AIBN admixed to the SMP10 solution. In Figure 57 (b), only one peak of SiN is shown, while in reality there are

many small peaks detected forming the SiN signature. The peak at 18 °θ of the measurement in Figure 57 (a) consist of multiple peaks which represents a Si pattern.

4.2. Discussion

The results presented in this study showed that it is possible to produce a dense, coherent SiC thin film with the polycarbosilan SMP10.

To achieve a SiC thin film, the oven atmosphere is of most importance. While coherent films were possible with the tube furnace, the FTIR analysis showed, that they were thoroughly oxidized and only a small amount of SiC formed. Switching to an inert atmosphere oven, not only SiC formed as sole component, but it was also crystalline as the XRD results proofed.

The film thickness is not only determined by spin coating speed and the concentration of the coating liquid as described by K. Norman and M Tyona [27], [29], but also by the activation of the substrate surface. As showed in Figure 45, the film thickness increases with higher surface energy. Thin films between 50 nm and 500 nm could be reproducibly manufactured.

The solvent of the SMP10 solution plays a major role in terms of surface quality. While there were many defects using n-hexane (Figure 50), there were much less defects after changing the solvent to m-xylene (Figure 53), most likely due its lower evaporation pressure.

The occurring defects, which look like pinholes, exist already in the curing phase, independent from UV curing or thermal curing. While the first assumption was, that outgassing during thermal treatment is the reason for the pinholes, with UV curing this assumption was proven to be only partly correct.

The pinhole like defects on the surface are an unwanted effect that maybe can be avoided in a good cleanroom atmosphere and other proper equipment (e.g. filters or controlled atmosphere) or with surfactants, which can lower the surface energy and prevent dewetting at particles (provided particles are the reason for the pinholes).

The attempt to cover the pinholes with multicoating as described by M. Achoi et al. [30] failed due to partly dewetting of the second layer, especially around the pinholes as can be seen in Figure 54. Surfactants in the second spin coating liquid may solve the dewetting.

The fabrication of a SiC thin film by admixing of Durazane to the SMP10 solution failed due to excessive dewetting, shown in Figure 52 but was successful with AIBN. The formation of SiN using AIBN could be proven with the FTIR (Figure 37) and XRD (Figure 56). Different concentrations of AIBN (1%, 2% and 3% AIBN in SMP10) resulted in different peak intensities of SiN in the FTIR spectrum, which also means, that the amount of AIBN might be too high for electrical purposes, since the peaks were quite strong, but the principle of nitrogen

incorporation could be proven. The SiC thin films with AIBN admixed to the SMP10 solution were semi-conductive, which was proven with the 4-point method, while no electrical conductivity could be measured with pure SiC without AIBN.

The concept of DOE was useful, since with the evaluation of five experiments, a trend which parameters are suitable was visible. With that systematic method, the best spin coating parameters for SiC thin films on Si are found to be a dilution of SMP10:solvent of 1:7, 1:10 and 1:13 with 3500 rpm, 3000rpm and 2500 rpm, respectively, where the solvent was m-xylene. The best parameters are defined where an adhesive, dense, coherent, and reproduceable thin film could be synthesised with as few as possible defects. The best cleaning of the substrate found was US cleaning, followed by the RCA (SC1/SC2) process and an immersion of the Si wafer in TEVS for 100 minutes, where the maximum adherence of the thin film was observed. TEVS modification of the Si surface was proven possible.

5. Conclusions and Outlook

A dense, coherent crystalline SiC thin film could be produced with a controllable thickness between 50 nm and 500 nm using SMP10 with the spin coating method. The spin coating parameters of 1:7, 1:10 and 1:13 SMP10 dilutions with 3500 rpm, 3000rpm and 2500 rpm, respectively have been found for best results. The solvent working best for the dilution was m-xylene. Additionally, the thin film could be fabricated either with or without AIBN as nitrogen donor. The formation of SiN was observed with FTIR analysis, and the grade of formation can be varied, depending on the amount of AIBN mixed to the coating solution. If the amount of AIBN will be lowered in future works, N doped SiC could be formed. The oven atmosphere is of most importance to achieve a SiC thin film, since oxygen in the furnace leads to the oxidation of the thin film, resulting in a SiO instead of a SiC layer. The successfully tested oven temperature was 1200 °C. For surface cleaning, an US bath in combination with the RCA SC1 and SC2 process was found to be the best choice. For the best adhesion of the SMP10 on the Si bulk material, the Si should be immersed in TEVS for 100 min. To avoid the presence of pinhole like defects, which still occurs, different solvents for SMP10 and AIBN or heating rates can be tested in future. A better cleanroom may solve the problem with the pinhole if they are particle induced. Also, the possibility to spin coat the samples under inert atmosphere such as nitrogen or argon, should be investigated. The effect of the hydrogen underetching of the substrate should also be investigated in future.

6. Literature

[1] H. J. Van Daal, W. F. Knippeneerg, and J. D. Wasscher, “ON THE ELECTRONIC CONDUCTION OF a-Sic CRYSTALS BETWEEN 300 AND 1500:K,” 1963.

[2] Liaw P. and Davis R.F., “Epitaxial Growth and Characterization of β - SiC Liaw_1985_J._Electrochem._Soc._132_642,” *J. Electrochem. Soc.*, vol. 132, no. 3, pp. 642–648, 1985.

[3] P. Moll, G. Pfusterschmied, S. Schwarz, M. Stöger-Pollach, and U. Schmid, “Impact of alternating precursor supply and gas flow on the LPCVD growth behavior of polycrystalline 3C-SiC thin films on Si,” *Sens Actuators A Phys*, vol. 372, Jul. 2024, doi: 10.1016/j.sna.2024.115376.

[4] X. Yang, X. Yang, K. Kawai, K. Arima, and K. Yamamura, “Novel SiC wafer manufacturing process employing three-step slurryless electrochemical mechanical polishing,” *J Manuf Process*, vol. 70, pp. 350–360, Oct. 2021, doi: 10.1016/j.jmapro.2021.08.059.

[5] P. J. Wellmann, “Review of SiC crystal growth technology,” *Semiconductor Science and Technology*, vol. 33, no. 10. Institute of Physics Publishing, Sep. 05, 2018. doi: 10.1088/1361-6641/aad831.

[6] M. Leitgeb, C. Zellner, M. Schneider, and U. Schmid, “A Combination of Metal Assisted Photochemical and Photoelectrochemical Etching for Tailored Porosification of 4H SiC Substrates,” *ECS Journal of Solid State Science and Technology*, vol. 5, no. 10, pp. P556–P564, 2016, doi: 10.1149/2.0041610jss.

[7] M. Leitgeb *et al.*, “Stacked Layers of Different Porosity in 4H SiC Substrates Applying a Photoelectrochemical Approach,” *J Electrochem Soc*, vol. 164, no. 12, pp. E337–E347, 2017, doi: 10.1149/2.1081712jes.

[8] C. Wu, C. Jacob, X. Ning, and S. Nishino, “Epitaxial growth of 3C-SiC on Si(111) from hexamethyldisilane,” 1996.

[9] L. Gou, C. Qi, J. Ran, and C. Zheng, “SiC ®lm deposition by DC magnetron sputtering,” *Thin Solid Films*, pp. 42–44, 1999.

[10] S. M. Rajab, I. C. Oliveira, M. Massi, H. S. Maciel, S. G. dos Santos Filho, and R. D. Mansano, “Effect of the thermal annealing on the electrical and physical properties of SiC thin films produced by RF magnetron sputtering,” *Thin Solid Films*, vol. 515, no. 1, pp. 170–175, Sep. 2006, doi: 10.1016/j.tsf.2005.12.052.

[11] P. M. Gammon *et al.*, “Development, characterisation and simulation of wafer bonded Si-on-SiC substrates,” *Mater Sci Semicond Process*, vol. 78, pp. 69–74, May 2018, doi: 10.1016/j.mssp.2017.10.020.

[12] J. Zhou, B. Lv, H. Liang, and Z. Wen, “Simulation and optimization of polysilicon thin film deposition in a 3000 mm tubular LPCVD reactor,” *Solar Energy*, vol. 253, pp. 462–471, Mar. 2023, doi: 10.1016/j.solener.2023.02.044.

[13] M. R. Jennings *et al.*, “Si/SiC heterojunctions fabricated by direct wafer bonding,” *Electrochemical and Solid-State Letters*, vol. 11, no. 11, 2008, doi: 10.1149/1.2976158.

[14] F. Mu, K. Iguchi, H. Nakazawa, Y. Takahashi, M. Fujino, and T. Suga, “Room-temperature wafer bonding of SiC-Si by modified surface activated bonding with sputtered Si nanolayer,” *Jpn J Appl Phys*, vol. 55, no. 4, Apr. 2016, doi: 10.7567/JJAP.55.04EC09.

[15] V. M. Airaksinen, J. Kaitila, H. Niemi’, J. Lahtinen’, and J. Saarilahtiz, “Physica Scripta Growth of Silicon Carbide on (100) Silicon Substrates by Molecular Beam Epitaxy,” 1994.

[16] J. H. Keller and R. G. Simmons, “Sputtering Process Model of Deposition Rate,” 1979.

[17] J. R. Arthur, “Molecular beam epitaxy,” *Surface Sience*, pp. 189–217, 2001, [Online]. Available: www.elsevier.com/locate/susc

[18] Starfire Systems, “SMP-10,” 2022. Accessed: Apr. 22, 2024. [Online]. Available: https://www.starfiresystems.com/wp-content/uploads/2022/03/SMP-10.pdf

[19] S. Kaur, R. Riedel, and E. Ionescu, "Pressureless fabrication of dense monolithic SiC ceramics from a polycarbosilane," *J Eur Ceram Soc*, vol. 34, no. 15, pp. 3571–3578, 2014, doi: 10.1016/j.jeurceramsoc.2014.05.002.

[20] Wikipedia, "Azobisisobutyronitrile." Accessed: Apr. 22, 2024. [Online]. Available: https://en.wikipedia.org/wiki/Azobisisobutyronitrile

[21] J. Schirmann and P. Bourdauducq, "Hydrazine," in *Ullmann's Encyclopedia of Industrial Chemistry*, Wiley, 2001. doi: 10.1002/14356007.a13_177.

[22] W. Syverson, M. Fleming, and P. Schubring, "The effects of reversing wafer-surface wetting properties of sulfuric acid: hydrogen peroxide wafer-cleaning solutions," in *Proceedings of the Fourth International Symposium on Cleaning Technology in Semiconductor Device Manufacturing*, 1996, p. 60.

[23] C. Du, Y. Zhao, and Y. Li, "Effect of Surface Cleaning Process on the Wafer Bonding of Silicon and Pyrex Glass," *J Inorg Organomet Polym Mater*, vol. 33, no. 3, pp. 673–679, Mar. 2023, doi: 10.1007/s10904-022-02510-x.

[24] S. Norhafiezah, R. M. Ayub, M. K. Md Arshad, A. H. Azman, M. A. Farehanim, and U. Hashim, "The Influence of Wafer Cleaning Process on the Silicon Surface Roughness," *Adv Mat Res*, vol. 1109, pp. 262–265, Jun. 2015, doi: 10.4028/www.scientific.net/amr.1109.262.

[25] Wikipedia, "Triethoxyvinylsilan." Accessed: Apr. 21, 2024. [Online]. Available: https://de.wikipedia.org/wiki/Triethoxyvinylsilan

[26] Y. Sun *et al.*, "Surface modification of silicon wafer by grafting zwitterionic polymers to improve its antifouling property," *Appl Surf Sci*, vol. 419, pp. 642–649, Oct. 2017, doi: 10.1016/j.apsusc.2017.05.016.

[27] K. Norrman, A. Ghanbari-Siahkali, and N. B. Larsen, "Studies of spin-coated polymer films," *Annual Reports on the Progress of Chemistry - Section C*, vol. 101. pp. 174–201, 2005. doi: 10.1039/b408857n.

[28] S. Obregón and V. Rodríguez-González, "Photocatalytic TiO2 thin films and coatings prepared by sol–gel processing: a brief review," *Journal of*

Sol-Gel Science and Technology, vol. 102, no. 1. Springer, pp. 125–141, Apr. 01, 2022. doi: 10.1007/s10971-021-05628-5.

[29] M. D. Tyona, "A theoritical study on spin coating technique," *Advances in materials Research*, vol. 2, no. 4, pp. 195–208, Dec. 2013, doi: 10.12989/amr.2013.2.4.195.

[30] M. F. Achoi, M. A. A. Noman, S. Kato, N. Kishi, and T. Soga, "Pinhole-free Methylammonium Bismuth Iodide Perovskite Solar Cells Via All-Solution-Processed Multi-step Spin Coating," *J Electron Mater*, vol. 51, no. 2, pp. 577–585, Feb. 2022, doi: 10.1007/s11664-021-09330-8.

[31] S. A. Potticary, "Chemical and Behavioral Study of Commercial Polycarbosilanes for the Processing of SiC Fibers," 2017.

[32] Y. de Hazan and D. Penner, "SiC and SiOC ceramic articles produced by stereolithography of acrylate modified polycarbosilane systems," *J Eur Ceram Soc*, vol. 37, no. 16, pp. 5205–5212, Dec. 2017, doi: 10.1016/j.jeurceramsoc.2017.03.021.

[33] C. Berthomieu and R. Hienerwadel, "Fourier transform infrared (FTIR) spectroscopy," *Photosynthesis Research*, vol. 101, no. 2–3. pp. 157–170, Sep. 2009. doi: 10.1007/s11120-009-9439-x.

[34] K. J. Savill, "Charge-carrier dynamics in hybrid metal halide perovskites for next-generation solar cells," University of Oxford, 2020.

[35] R. Rottenfusser, E. E. Wilson, and M. W. Davidson, "Education in Microscopy and Digital Imaging," https://zeiss-campus.magnet.fsu.edu/articles/basics/reflected.html. Accessed: Jun. 18, 2024. [Online]. Available: https://zeiss-campus.magnet.fsu.edu/articles/basics/reflected.html

[36] M. Kannan, "Scanning electron microscopy: Principle, components and applications," *A textbook on fundamentals and applications of nanotechnology*, pp. 81–92, 2018.

[37] A. Kozbial *et al.*, "Study on the surface energy of graphene by contact angle measurements," *Langmuir*, vol. 30, no. 28, pp. 8598–8606, Jul. 2014, doi: 10.1021/la5018328.

[38] T. Huhtamäki, X. Tian, J. T. Korhonen, and R. H. A. Ras, "Surface-wetting characterization using contact-angle measurements," *Nat Protoc*, vol. 13, no. 7, pp. 1521–1538, Jul. 2018, doi: 10.1038/s41596-018-0003-z.

[39] Leitgeb Markus, "Preparation and characterization of polymeric stamps for R2R nanoimprint lithography," 2014. Accessed: Apr. 23, 2024. [Online]. Available: https://permalink.catalogplus.tuwien.at/AC11447206

[40] Y. X. Zhuang and O. Hansen, "Correlation of effective dispersive and polar surface energies in heterogeneous self-assembled monolayer coatings," *Langmuir*, vol. 25, no. 10, pp. 5437–5441, May 2009, doi: 10.1021/la804318p.

[41] H. Khan, A. S. Yerramilli, A. D'Oliveira, T. L. Alford, D. C. Boffito, and G. S. Patience, "Experimental methods in chemical engineering: X-ray diffraction spectroscopy—XRD," *Canadian Journal of Chemical Engineering*, vol. 98, no. 6. Wiley-Liss Inc., pp. 1255–1266, Jun. 01, 2020. doi: 10.1002/cjce.23747.

[42] D. Windover, D. L. Gil, A. Henins, and J. P. Cline, "NIST high resolution x-ray diffraction standard reference material: SRM 2000," in *AIP Conference Proceedings*, 2009, pp. 50–54. doi: 10.1063/1.3251259.

[43] A. M. El-Naggar, S. Y. El-Zaiat, and S. M. Hassan, "Optical parameters of epitaxial GaN thin film on Si substrate from the reflection spectrum," *Opt Laser Technol*, vol. 41, no. 3, pp. 334–338, Apr. 2009, doi: 10.1016/j.optlastec.2008.05.022.

[44] B. R. A Fisher, *Design of Experiments*. 1937.

[45] K. Dunn, "Process Improvement Using Data Release 10d109," 2023. Accessed: May 15, 2024. [Online]. Available: https://learnche.org/pid/

[46] F. Shariatmadar Tehrani, B. T. Goh, M. R. Muhamad, and S. A. Rahman, "Pressure dependent structural and optical properties of silicon carbide thin films deposited by hot wire chemical vapor deposition from pure silane and methane gases," *Journal of Materials Science: Materials in Electronics*, vol. 24, no. 4, pp. 1361–1368, Apr. 2013, doi: 10.1007/s10854-012-0934-z.

[47] A. D. Mallorquí *et al.*, "Field-effect passivation on silicon nanowire solar cells," *Nano Res*, vol. 8, no. 2, pp. 673–681, Feb. 2015, doi: 10.1007/s12274-014-0551-7.

[48] Honeywell, "US 6,225,238 B1," 2001

[49] M. I. Ojovan, R. Tournier, and R. F. Tournier, "On Structural Rearrangements Near the Glass Transition Temperature in Amorphous Silica On Structural Rearrangements Near The Glass Transition Temperature in Amorphous Silica," *Amorphous Silica. Materials*, vol. 14, no. 18, p. 5235, 2021, doi: 10.3390/ma14185235ï.

[50] M. Bassu, G. Scheen, and L. A. Francis, "Thick macroporous silicon membranes: Influence of the masking layer on the underetching characteristics," *Sens Actuators A Phys*, vol. 185, pp. 66–72, Oct. 2012, doi: 10.1016/j.sna.2012.06.019.

[51] D. S. Perloff, "Four-Point Sheet Resistance Measurements of Semiconductor Doping Uniformity," *J Electrochem Soc*, pp. 582–590, 1977.

[52] D. S. Perloff, "FOUR-POINT SHEET RESISTANCE CORRECTION FACTORS FOR THIN RECTANGULAR SAMPLES," 1977.

[53] M. J. Deen and F. Pascal, "Electrical characterization of semiconductor materials and devices - Review," *Journal of Materials Science: Materials in Electronics*, vol. 17, no. 8. pp. 549–575, Aug. 2006. doi: 10.1007/s10854-006-0001-8.

[54] D. K. Schroder, *Semiconductor material and device characterization*. IEEE Press, 2006.

[55] Malvern Panalytical, "HighScore Plus." Accessed: May 15, 2024. [Online]. Available: https://www.malvernpanalytical.com/en/products/category/software/x-ray-diffraction-software/highscore-with-plus-option

[56] W. Wisniewski, C. Genevois, E. Veron, and M. Allix, "Experimental evidence concerning the significant information depth of X-ray diffraction

(XRD) in the Bragg-Brentano configuration," *Powder Diffr*, vol. 38, no. 2, pp. 139–144, Jun. 2023, doi: 10.1017/S0885715623000052.

7. Appendix

7.1. Varied parameters of the experiments

Table 7.1: Varied parameters of the experiments

Solvent for SMP10	Dilution	Rotation per minute	Cleaning	Surface Modification	Additive
n-Hexan	1:1 – 1:100	1000 - 4000			
n-Hexan	1:1 – 1:50	1000 – 4000		TEVS	
n-Hexan	1:1 – 1:50	1000 – 4000	O_2 cleaning		
n-Hexan	1:1 – 1:50	1000 – 4000	O_2 cleaning	TEVS	
n-Hexan	1:1 – 1:50	1000 – 4000	Piranha acid		
n-Hexan	1:1 – 1:50	1000 – 4000	Piranha acid	TEVS	
n-Hexan	1:1 – 1:50	1000 – 4000	US, Piranha acid	TEVS	
n-Hexan	1:1 – 1:50	1000 – 4000	RCA		
n-Hexan	1:1 – 1:50	1000 – 4000	RCA	TEVS	
n-Hexan	1:1 – 1:50	1000 – 4000	US, RCA	TEVS	
n-Hexan	1:1 – 1:50	1000 – 4000	HF-Tip		
n-Hexan	1:1 – 1:50	1000 – 4000	Piranha acid, HF-Tip		
n-Hexan	1:7 – 1:15	1000 – 4000	US, RCA		Duracan
n-Hexan	1:7 – 1:15	1000 – 4000	US, RCA	TEVS	Duracan
n-Hexan	1:7 – 1:15	1000 – 4000	US, RCA		AIBN
n-Hexan	1:7 – 1:15	1000 – 4000	US, RCA	TEVS	AIBN
m-Xylene	1:4 – 1:20	1000 – 4000	US, RCA		
m-Xylene	1:4 – 1:20	1000 – 4000	US, RCA		Duracan
m-Xylene	1:4 – 1:20	1000 – 4000	US, RCA	TEVS	Duracan
m-Xylene	1:4 – 1:20	1000 – 4000	US, RCA		AIBN
m-Xylene	1:4 – 1:20	1000 – 4000	US, RCA	TEVS	AIBN

7.2. Overview of the results from the carried out experiments

Solvent for SMP10	Dilution	Rotation per minute	Cleaning/Surface Modification	Result	Comment
n-Hexan	1:1 – 1:100	1000 - 4000		Above 1:50 film too thin or no film detectable, Below 1:4 film too thick: flake of and cracking	Many defects on all samples; Trend to Dilutions from 1:7 to 1:15 with 2500 rpm – 3500 rpm
n-Hexan	1:1 – 1:100	1000 – 4000	TEVS	Above 1:50 film too thin or no film detectable, Below 1:4 film too thick: flake of and cracking	Less defects on all samples than without TEVS; Trend to Dilutions from 1:7 to 1:15 with 2500 rpm – 3500 rpm
n-Hexan	1:7 – 1:30	1000 – 3500	O_2 cleaning	Bad adhesion, dewetting for all samples	
n-Hexan	1:7 – 1:30	1000 – 3500	O_2 cleaning / TEVS	Bad adhesion, dewetting for all samples	
n-Hexan	1:7 – 1:30	1500 – 3500	Piranha acid	Coherent film, many defects, Trend to 1:10 with 3000 rpm	
n-Hexan	1:7 – 1:30	1500 – 3500	Piranha acid / TEVS	Coherent film, many defects, Trend to 1:10 with 3000 rpm	Less defects that without TEVS
n-Hexan	1:7 – 1:30	1500 – 3500	US, Piranha acid / TEVS	Coherent film, many defects, Trend to 1:10 with 3000 rpm	Fewer defects when using US
n-Hexan	1:7 – 1:30	1500 – 3500	RCA	Coherent film, many defects,	Better adhesion that with

				Trend to 1:10 with 3000 rpm	Piranha clean, also less defects
n-Hexan	1:7 – 1:30	1500 – 3500	RCA / TEVS	Coherent film, many defects, Trend to 1:10 with 3000 rpm	Less defects that without TEVS
n-Hexan	1:7 – 1:30	1500 – 3500	US, RCA / TEVS	Coherent film, many defects, Trend to 1:10 with 3000 rpm	Fewer defects when using US
n-Hexan	1:7 – 1:30	1500 – 3500	HF-Tip	Bad adhesion, dewetting on all samples	
n-Hexan	1:7 – 1:30	1500 – 3500	Piranha acid, HF-Tip	Bad adhesion, dewetting on all samples	
n-Hexan	1:7 – 1:15	1500 – 3500	US, RCA / Durazane	Bad to no adhesion, dewetting on all samples	
n-Hexan	1:7 – 1:15	1500 – 3500	US, RCA / TEVS / Durazane	Bad to no adhesion, dewetting on all samples	
n-Hexan	1:7 – 1:15	1500 – 3500	US, RCA / AIBN	Coherent film, many defects, Trend to 1:10 with 3000 rpm	SiN formation observed
n-Hexan	1:7 – 1:15	1500 – 3500	US, RCA / TEVS / AIBN	Coherent film, many defects, Trend to 1:10 with 3000 rpm	Better Adhesion, less defects than without TEVS
m-Xylene	1:4 – 1:20	1500 – 3500	US, RCA	Coherent film, some defects, Trend to 1:10 with 3000 rpm	
m-Xylene	1:4 – 1:20	1500 – 3500	US, RCA / Durazane	Bad to no adhesion, dewetting on all samples	

m-Xylene	1:4 – 1:20	1500 – 3500	US, RCA / TEVS / Durazane	Bad to no adhesion, dewetting on all samples	
m-Xylene	1:4 – 1:20	1500 – 3500	US, RCA/ AIBN	Coherent film, some defects, Trend to 1:10 with 3000 rpm	
m-Xylene	1:4 – 1:20	1500 – 3500	US, RCA / TEVS / AIBN	Coherent film, some defects, Trend to 1:10 with 3000 rpm	Less defects than without TEVS

7.3. Phyton code for calculating the film thickness

```
# -*- coding: utf-8 -*-
"""
Created on Thu Sep 23 09:41:14 2021
@author: leitgeb
"""
from matplotlib import pyplot
import numpy as np
import math
from matplotlib import rcParams
import pylab as pl
import sys
import matplotlib
from patsy import cr
from sklearn.linear_model import LinearRegression
from scipy.interpolate import interp1d
from scipy import interpolate
```

```
from pandas import DataFrame


#rcParams.update({'figure.autolayout': True})
#font = {'family' : 'normal',
#        'weight' : 'bold',
#        'size'   : 12}
#matplotlib.rc('font', **font)
#matplotlib.rc('axes', linewidth = 2)


def read_file(filename):



    #filename = "1zu7gruen.csv"
    readfile = open(filename, "r") #r stands for the intention of reading. "w" would be write to file
    sepFile = readfile.read().split("\n") #sepFile is a list like this ["12, 3", "5, 4"....]
    sepFile = sepFile[1:]
    wavelength = [float(sepFile[x].split(";")[0]) for x in range(len(sepFile)-1)]
    wavenumber = [1/x for x in wavelength]
    reflectance = [float(sepFile[x].split(";")[1]) for x in range(len(sepFile)-1)]
    return (wavelength, reflectance, wavenumber)


def spline_regression(x_data, y_data, df=100):
    # Generate spline basis with different degrees of freedom
    x_basis = cr(x_data, df=df, constraints="center")
    # Fit model to the data
```

```
    model = LinearRegression().fit(x_basis, y_data)
    # Get estimates
    y_hat = model.predict(x_basis)
    return y_hat


def find_maxima(x_values, y_values):
    extreme_x_positions = []
    extreme_y_positions = []
    for runner in range((len(x_values) - 2)):
        slope1 = (y_values[runner + 1] - y_values[runner])/(x_values[runner +
1] - x_values[runner])
        slope2 = (y_values[runner + 2] - y_values[runner + 1])/(x_values[runner
+ 2] - x_values[runner + 1])
        if slope1 * slope2 < 0 and slope1 > slope2:
            extreme_x_positions.append(x_values[runner + 1])
            extreme_y_positions.append(y_values[runner + 1])
    return (extreme_x_positions, extreme_y_positions)


def find_minima(x_values, y_values):
    extreme_x_positions = []
    extreme_y_positions = []
    for runner in range((len(x_values) - 2)):
        slope1 = (y_values[runner + 1] - y_values[runner])/(x_values[runner +
1] - x_values[runner])
        slope2 = (y_values[runner + 2] - y_values[runner + 1])/(x_values[runner
+ 2] - x_values[runner + 1])
        if slope1 * slope2 < 0 and slope1 < slope2:
            extreme_x_positions.append(x_values[runner + 1])
            extreme_y_positions.append(y_values[runner + 1])
```

```
    return (extreme_x_positions, extreme_y_positions)


def make_envelope_fit(filename, upper_envelope_order, lower_envelope_order,
spline_regression_sensitivity):
    original_data = read_file(filename)
    fitted_curve = spline_regression(original_data[0], original_data[1],
spline_regression_sensitivity)
    maximum_positions = find_maxima(original_data[0], fitted_curve)
    minimum_positions = find_minima(original_data[0], fitted_curve)
    upper_spline_fit = interp1d(maximum_positions[0], maximum_positions[1],
kind = upper_envelope_order)
    lower_spline_fit = interp1d(minimum_positions[0], minimum_positions[1],
kind = lower_envelope_order)


    upper_envelope_range =
original_data[0][original_data[0].index(maximum_positions[0][0]):original_dat
a[0].index(maximum_positions[0][-1])]
    upper_envelope = upper_spline_fit(upper_envelope_range)


    lower_envelope_range =
original_data[0][original_data[0].index(minimum_positions[0][0]):original_dat
a[0].index(minimum_positions[0][-1])]
    lower_envelope = lower_spline_fit(lower_envelope_range)


    pl.plot(original_data[0], original_data[1], color = "red")
    pl.plot(maximum_positions[0], maximum_positions[1], "bo", alpha = 0.5)
    pl.plot(minimum_positions[0], minimum_positions[1], "bo", alpha = 0.5)
    pl.plot(lower_envelope_range, lower_envelope)
    pl.plot(upper_envelope_range, upper_envelope)
```

```
    extreme_x_positions      =      list(set.union(set(minimum_positions[0]),
set(maximum_positions[0])))
    extreme_x_positions.sort()
    extreme_x_positions = extreme_x_positions[1:-1]
    maximums = upper_spline_fit(extreme_x_positions)
    minimums = lower_spline_fit(extreme_x_positions)
    #print(extreme_x_positions)
    #pl.plot(extreme_x_positions, maximums, "bo", alpha = 0.5)
    #pl.plot(extreme_x_positions, minimums, "bo", alpha = 0.5)

    pl.grid(True)
    pl.xlabel("Wavelength [nm]")
    pl.ylabel("Reflection [%]")

    return (extreme_x_positions, maximums, minimums)

a = make_envelope_fit("1zu7gruen.csv", 2,2,100)
l1 = a[0]
l2 = a[1]
l3 = a[2]
df = DataFrame({'Wavelength': l1, 'E_M': l2 , 'E_m': l3})
df.to_excel('test.xlsx', sheet_name='sheet1', index=False)
```

7.4. R-Code for analyzing the results of the experiments done with DoE

```
require(rlang)
library(pid)
```

```
Speed <- c(-1 ,1, 0, -1, 1)

Dilution <- c(-1, -1, 0, 1, 1)


#y <- c(143, 145, 82.3, 83.3, 64.5) #pyrolized

#y <- c(585.47, 470.65,289.55, 298.51, 267.155) #green

y <- c(994.475, 785.28, 474.44, 476.79, 440.655) #liquid




doe.model <- lm(y ~ Speed + Dilution + Speed*Dilution)

paretoPlot(doe.model)

contourPlot(doe.model,    xlim    =    c(-1.2,1.2),    ylim    =c(-1.2,1.2),
colour.function=terrain.colors)


doe.model
```